# Advancements in jet turbulence and noise modeling: accurate one-way solutions and empirical evaluation of the nonlinear forcing of wavepackets

Thesis by

Aaron Towne

In Partial Fulfillment of the Requirements

for the Degree of

Doctor of Philosophy


California Institute of Technology

Pasadena, California

2016

(Defended December 3, 2015)

*FOR HIS GLORY*

# Acknowledgments

I could not have completed this thesis without the guidance, support, and encouragement of many people. First and foremost, to my wonderful wife and teammate, Lindsey: thank you for your unwavering love and support and for making the many sacrifices necessary for me to pursue this degree. I appreciate you immensely. I'm also grateful to my parents, who by teaching me to value education and pursue excellence, opened up limitless opportunities for me and made this accomplishment possible.

I owe a debt of gratitude to my advisor, Tim Colonius. Tim, thank you for the countless hours you invested in me. Above all, you showed me, by example, how to approach research – with curiosity, irreproachable rigor, and, perhaps most importantly, with unquenchable optimism. Moreover, as a supervisor, you seemed to always know when to apply pressure and when to extend grace.

I also want to acknowledge several of my collaborators: Peter Jordan, André Cavalieri, Guillaume Brès, and Tom Hagstrom. Peter and André, our intermittent brainstorming sessions and late-night discussions were both fruitful and entertaining. Guillaume, thank you for your heroic efforts to rapidly provide me with the data I needed to complete this thesis. Also, I want to thank Tom for pointing me in the right direction early in the development of the outflow-based one-way integration method.

I'm grateful for the comradery and frequent aid of my fellow Computational Flow Physics group members: Dani Rodriguéz, Ani Sinha, Jun Liu, Oliver Schmidt, Vedran Coralic, Sebastian Liska, Mathew Inkman, Jomela Meng, Jeesoon Choi, Chen Tsai, Ed Burns, Andres Goza, Jay Qi, Kazuki Maeda, Phillipe Tosi, and André Fernando de Castro da Silva. To my fellow jet-noise laborers Dani, Ani, and Oliver: it was a pleasure working with and learning from each of you. Jomela, we may

have broken our pact to graduate in five years, but at least we could commiserate together along the way.

I would have certainly given up during the madness that was the first year class-load without the rest of my incoming MCE class: Jeff Amelang, Tom Allen, Gerry Della Rocca, Asghar Aryanfar, Cindy Wang, Srivatsan Hulikal, Ramathasan Thevamaran, Swetha Veeraraghavan, Marcella Gomez, Melissa Tanner, Trevor Currie, Arnar Bjornsson, and Jie Jiang.

I'm thankful for the faithful care and support of my many friends from Pacific Crossroads Church. Yes, most of you broke the first rule of interacting with PhD students – to never ask how one's thesis is coming along – innumerable times, but always with the best of intentions: to take interest in my life and to encourage me.

Finally, I'd like to thank my thesis committee – Guillaume Blanquart, Beverley McKeon, and Fazle Hussain – for serving in this capacity and for providing valuable feedback on this thesis.

# Abstract

Jet noise reduction is an important goal within both commercial and military aviation. Although large-scale numerical simulations are now able to simultaneously compute turbulent jets and their radiated sound, lost-cost, physically-motivated models are needed to guide noise-reduction efforts. A particularly promising modeling approach centers around certain large-scale coherent structures, called wavepackets, that are observed in jets and their radiated sound. The typical approach to modeling wavepackets is to approximate them as linear modal solutions of the Euler or Navier-Stokes equations linearized about the long-time mean of the turbulent flow field. The near-field wavepackets obtained from these models show compelling agreement with those educed from experimental and simulation data for both subsonic and supersonic jets, but the acoustic radiation is severely under-predicted in the subsonic case. This thesis contributes to two aspects of these models. First, two new solution methods are developed that can be used to efficiently compute wavepackets and their acoustic radiation, reducing the computational cost of the model by more than an order of magnitude. The new techniques are spatial integration methods and constitute a well-posed, convergent alternative to the frequently used parabolized stability equations. Using concepts related to well-posed boundary conditions, the methods are formulated for general hyperbolic equations and thus have potential applications in many fields of physics and engineering. Second, the nonlinear and stochastic forcing of wavepackets is investigated with the goal of identifying and characterizing the missing dynamics responsible for the under-prediction of acoustic radiation by linear wavepacket models for subsonic jets. Specifically, we use ensembles of large-eddy-simulation flow and force data along with two data decomposition techniques to educe the actual nonlinear forcing experienced by wavepackets in a Mach 0.9 turbulent jet. Modes with high energy are extracted using proper

orthogonal decomposition, while high gain modes are identified using a novel technique called empirical resolvent-mode decomposition. In contrast to the flow and acoustic fields, the forcing field is characterized by a lack of energetic coherent structures. Furthermore, the structures that do exist are largely uncorrelated with the acoustic field. Instead, the forces that most efficiently excite an acoustic response appear to take the form of random turbulent fluctuations, implying that direct feedback from nonlinear interactions amongst wavepackets is not an essential noise source mechanism. This suggests that the essential ingredients of sound generation in high Reynolds number jets are contained within the linearized Navier-Stokes operator rather than in the nonlinear forcing terms, a conclusion that has important implications for jet noise modeling.

# Contents

# List of Figures

# List of Tables

# Chapter 1

# Introduction

## 1.1 Motivation

Worldwide dependence on air-travel is at an all-time high and continues to increase, with recent growth in total flights around five percent annually (International Air Transport Association , 2014). At the same time, boosted by greater public awareness of the adverse health effects of excess noise pollution, airports and airlines are being required to progressively reduce their noise footprints.

Regulation of commercial aircraft noise began shortly after the introduction of jet-powered airplanes. In the United States, the Aircraft Noise Abatement Act of 1968 required the Federal Aviation Administration (FAA) to develop and enforce safe standards for aircraft noise (Bearden, 2006). That same year, the International Civil Aviation Organization (ICAO) instigated the establishment of international specifications to control aircraft noise, which were eventually adopted in 1971 (The Convention on International Civil Aviation, 2006). These standards, which were also adopted by the FAA, became more restrictive in 1977 and again in 2006. Recently, the ICAO approved even more stringent regulations that will be enforced beginning in 2017.

These increasingly demanding requirements have been achieved primarily by a steady increase in the bypass ratio of commercial turbofan jet engines. A higher bypass ratio, defined as the ratio between the mass that flows through an engine's fan and the mass that flows through its core, results in a lower nozzle exit velocity. Since aerodynamic noise is a strong function of jet exit velocity, a higher bypass ratio yields a quieter jet. Modern high-bypass-ratio turbofan engines are around 20

dB quieter than their low-bypass-ratio predecessors. Unfortunately, the potential for further noise reduction by bypass ratio increase is limited. Increasing an engine's bypass ratio necessarily increases the engine's size to maintain thrust. Modern engines have reached the point that any further increase in size will soon require complete redesign of the aircraft. Therefore, further improvements will require new approaches to noise reduction.

While great strides have been made toward quieting commercial aircraft, the noise levels produced by military tactical aircraft have not decreased and have even increased. Noise produced by military aircraft is unregulated and is often disruptive in communities adjacent to military bases and dangerous to airstrip and flight deck personnel. For example, the noise levels on Navy aircraft carriers, which can reach over 150 dB, far exceed those which can be safely attenuated by state-of-the-art hearing protection. This contributes to the approximately $1 billion per year that the U.S. Department of Veteran Affairs spends on hearing loss cases (Naval Research Advisory Committee 2009). For tactical aircraft, the noise produced by the jet exhaust dominates all other sources of noise. However, because of high performance requirements, using high-bypass-ratio engines to reduce noise is not a viable option for these aircraft.

The search for innovative noise reduction technologies in both commercial and military aviation will require accurate, low-cost models that can be used to guide and test potential strategies and more generally attain a better understanding of flow-generated noise. This thesis is concerned with the development of such models.

## 1.2 Jet noise models

### 1.2.1 The Navier-Stokes equations

The most fundamental model for a jet and its radiated sound is the compressible Navier-Stokes equations. Throughout this thesis, we write these equations in cylindrical coordinates and in terms of specific volume $\nu$, pressure $p$, and cylindrical velocity components $u_x$, $u_r$, $u_\theta$:

$$\frac{D\nu}{Dt} - \nu\left(\nabla \bullet u\right) = 0, \tag{1.1a}$$

$$\frac{Du_x}{Dt} + \nu\frac{\partial p}{\partial x} = \frac{1}{Re}\nu\nabla^2 u_x, \tag{1.1b}$$

$$\frac{Du_r}{Dt} - \frac{u_\theta^2}{r} + \nu\frac{\partial p}{\partial r} = \frac{1}{Re}\nu\left(\nabla^2 u_r - \frac{u_r}{r^2} - \frac{2}{r^2}\frac{\partial u_\theta}{\partial \theta}\right), \tag{1.1c}$$

$$\frac{Du_\theta}{Dt} + \frac{u_r u_\theta}{r} + \frac{\nu}{r}\frac{\partial p}{\partial \theta} = \frac{1}{Re}\nu\left(\nabla^2 u_\theta - \frac{u_\theta}{r^2} + \frac{2}{r^2}\frac{\partial u_r}{\partial \theta}\right), \tag{1.1d}$$

$$\frac{Dp}{Dt} + \gamma p\left(\nabla \bullet u\right) = \frac{\gamma}{RePr}\left(\nu\nabla^2 p + p\nabla^2\nu\right), \tag{1.1e}$$

with

$$\frac{D}{Dt} = \frac{\partial}{\partial t} + u_x\frac{\partial}{\partial x} + u_r\frac{\partial}{\partial r} + \frac{u_\theta}{r}\frac{\partial}{\partial \theta}, \tag{1.2}$$

$$\nabla^2 = \frac{\partial^2}{\partial x^2} + \frac{\partial^2}{\partial r^2} + \frac{1}{r}\frac{\partial}{\partial r} + \frac{1}{r^2}\frac{\partial^2}{\partial \theta^2}, \tag{1.3}$$

and

$$\nabla \bullet u = \frac{\partial u_x}{\partial x} + \frac{\partial u_r}{\partial r} + \frac{u_r}{r} + \frac{1}{r}\frac{\partial u_\theta}{\partial \theta}. \tag{1.4}$$

All variables have been appropriately non-dimensionalized by an ambient sound speed $c_\infty$, density $\rho_\infty$, and the nozzle diameter $D$. The fluid is approximated as a perfect gas with specific heat ratio $\gamma$, constant Reynolds number $Re = \rho_\infty c_\infty D/\mu_\infty$, and Prandtl number $Pr = C_p\mu_\infty/k$. Here, $\mu_\infty$ is the ambient dynamic viscosity, $C_p$ is the specific heat at constant pressure, and $k$ is the thermal conductivity of the fluid. We have neglected viscous energy dissipation and assumed that the gradient of the dilatation is small. The ideal gas law under this non-dimensionalization is

$$p = \frac{\gamma - 1}{\gamma}T/\nu, \tag{1.5}$$

where $T$ is the thermodynamic temperature. When augmented with appropriate boundary and initial conditions, equation (1.1) governs both the hydrodynamics and acoustics of the jet.

### 1.2.2 Large-scale simulations

Recent advances in computational methods and the increasing availability of computing power have made possible numerical simulations of equation (1.1) capable of simultaneously predicting the near-field hydrodynamics of the jet and its radiated sound.

At low Reynolds numbers, direct numerical simulation (DNS) is feasible (Freund 2001). At higher Reynolds numbers, which are more practically relevant, the vast separation between the largest and smallest length scales (for example, the potential core length and the Kolmogorov length scale, respectively) makes direct numerical simulation impossible. The natural fall-back is to model the smallest scales while explicitly computing the large scales via large-eddy-simulation (LES) (Bodony & Lele 2008). Only in the last few years has LES reached the resolution and sophistication required to properly represent the thin, turbulent boundary layers that exist in the near-nozzle region of real jets (Brès et al. 2015).

Despite the increasing feasibility and accuracy of large-scale jet-noise simulations, they have at least two limitations as models. First, by any practical measure, these simulations are still computationally expensive. The search for innovative noise reduction techniques, especially those based on formal optimization frameworks, will likely necessitate an iterative approach requiring many simulations. At present, this would be a monumental undertaking using DNS or LES. Second, on their own, these simulations provide no insight into the physical mechanisms responsible for sound production, nor guidance for leveraging them to reduce noise – the jet turbulence and acoustics come as one intertwined bundle.

These two limitations of direct jet-noise simulation highlight the critical need for reduced-order models that can be rapidly computed and used to uncover the physics that are acoustically relevant. Such models do not supersede large-scale simulations; they critically rely on them for inspiration and validation (see, for example, Chapter 3 of this thesis).

### 1.2.3 Acoustic analogy

On the opposite end of the spectrum from large-scale numerical simulations, Lighthill's acoustic analogy (Lighthill 1952, 1954) reduces the entire jet noise problem to a single inhomogeneous wave equation for the density $\rho$:

$$\left(\frac{\partial^2}{\partial t^2} - c_\infty^2 \nabla^2\right) \rho = \frac{\partial^2 T_{ij}}{\partial x_i \partial x_j}. \tag{1.6}$$

This is an exact rearrangement of the Navier-Stokes equations, provided that the source term $T_{ij}$ is known exactly. The solution of equation (1.6) can be obtained in the far-field using a Green's function. A predictive model is obtained by approximating the source terms. If simulation data is available for a given jet, one can compute the source, but despite over sixty years of concentrated effort, any general approach for accurately prescribing the Lighthill source terms has been elusive.

Source terms that can be more easily modeled have been sought by generalizing Lighthill's theory by subsequently moving more and more terms from the source term to the left-hand-side propagator (Phillips 1960, Lilley 1974). The culmination of this trend was realized by Goldstein's generalized acoustic analogy (Goldstein 2003), in which the complete linearized Navier-Stokes operator appears on the left-hand-side, leaving only nonlinear interactions within the source term.

These nonlinear interactions play a central role in several existing theories of jet noise. For example, vortex-pairing (Laufer 1974, Williams & Kempton 1978, Kibens 1980), nonlinear vortex-ring breakdown (Hussain 1983), and nonlinear saturation of instability waves (Sandham et al. 2006, Sandham & Salgado 2008, Suponitsky et al. 2010) have all been proposed as key sources of jet noise. Within any acoustic analogy-based approach, these processes must be accurately represented by the source term. Current strategies for approximating these source terms require high-fidelity flow data as an input, limiting the utility of these theories as jet-noise models.

The modeling approach we develop in section 1.2.4.2 bears some resemblance to Goldstein's analogy. However, our philosophical outlook is quite different, and in fact essentially opposite, from Goldstein's (or that underpinning any acoustic analogy) – we regard the linear operator, rather than

the source, to be of primary importance. This will become clear in Chapter 3.

### 1.2.4 Wavepacket models

An alternative, physically-motivated reduced-order approach centers around modeling certain large-scale coherent structures, called wavepackets, that are observed in jets and their radiated sound.

#### 1.2.4.1 Wavepackets in jets

Large-scale structures were first observed in turbulent jets by Crow & Champagne (1971). They postulated that the eddies clearly seen at low Reynolds numbers also exist in high Reynolds number turbulence and amplified these latent structures by periodically forcing the jet using a loudspeaker. In unforced jets, these structures can be detected using multipoint velocity and pressure measurements, which show that they are coherent over length and time scales far exceeding the integral scales of turbulence (Fuchs 1972), and indeed take the form of advecting wavepackets with slowly-varying wavelength and phase-speed. For example, Figure 1.1 shows the cross-spectral density of pressure measurements taken along a cylindrical microphone array just outside the jet (with respect to the microphone at $x = 3$) for a Mach 0.9 jet at two different frequencies (Reba et al. 2010). The data exhibit a clear wavepacket structure, as demonstrated by the close fit achieved using a simple Gaussian wavepacket model.

In turbulent jets, these structures make up a modest portion of the total flow energy (Michalke & Fuchs 1975, Cavalieri et al. 2013). However, their spatiotemporal coherence makes them acoustically efficient compared to the more energetic incoherent turbulent fluctuations (Jordan & Colonius 2013). In particular, wavepackets are strongly correlated with far-field acoustic radiation, particularly at low angles to the jet axis, where sound is most intense (Lee & Ribner 1972, Hileman et al. 2005, Tam et al. 2008). The spatial growth and decay of wavepackets Crighton & Huerre (1990), and especially their breakdown near the end of the potential core (Morrison & McLaughlin 1979, Hussain 1986, Hileman et al. 2005), have been shown to be especially relevant as sound source mechanisms.

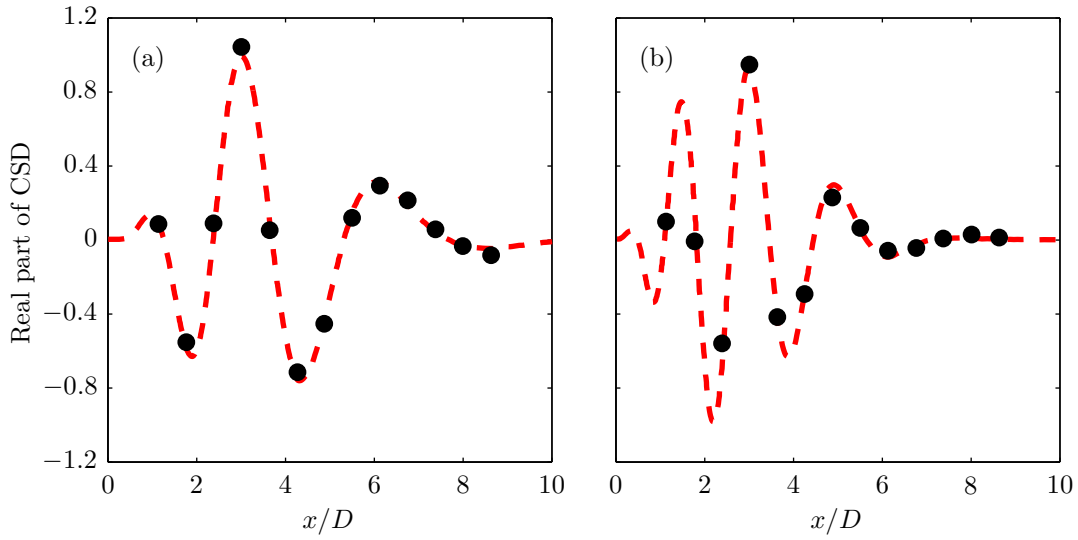


Figure 1.1: Cross-spectral density of pressure measurements ( ● ) taken along a cylindrical microphone array just outside the jet, with respect to the microphone at $x = 3$, for a Mach 0.9 jet at Strouhal number (a) 0.25 and (b) 0.40 (Reba et al. 2010). A simple Gaussian wavepacket model (– – –) can be tuned to closely match the data.

#### 1.2.4.2 Wavepackets as modal solutions

These observations suggest that a reduced-order jet noise model could be constructed by modeling wavepackets. The typical approach to modeling wavepackets is to approximate them as linear modal solutions of the Euler or Navier-Stokes equations linearized about the long-time mean of the turbulent flow field. This approach dates to the 1970s, when it was found that the wavelength and phase-speed of experimentally-measured wavepackets could be explained by linear stability theory (Michalke 1971, Mattingly & Chang 1974, Crighton & Gaster 1976, Tam & Burton 1984). Further justification for this approach was provided by Suzuki & Colonius (2006), who showed that wavepackets in the near-acoustic field can be quantitatively identified as instability waves.

The mathematical formulation of this approach begins with the full compressible Navier-Stokes equations, which can be written conceptually as

$$\frac{\partial q}{\partial t} = \mathcal{F}(q)\,, \tag{1.7}$$

where $q = [\nu, u_x, u_r, u_\theta, p]^T$ and the nonlinear operator $\mathcal{F}$ is implicitly defined by equation (1.1).

Substituting the standard Reynolds decomposition

$$q\left(x,r,\theta,t\right)=\bar{q}\left(x,r\right)+q'\left(x,r,\theta,t\right) \tag{1.8}$$

into equation (1.7) and isolating the terms that are linear in $q'$ yields an equation of the form

$$\frac{\partial q'}{\partial t}-\mathcal{A}\left(\bar{q}\right)q'=f\left(x,r,\theta,t\right), \tag{1.9}$$

where

$$\mathcal{A}\left(\bar{q}\right)=\frac{\partial\mathcal{F}}{\partial q}\left(\bar{q}\right) \tag{1.10}$$

and $f$ contains the remaining nonlinear terms.

Sine our interest is in round, statistically stationary jets, it suffices to decompose $q'$ and $f$ into azimuthal and temporal Fourier modes:

$$q'\left(x,r,\theta,t\right)=\sum_{\omega}\sum_{m}\hat{q}_{\omega,m}\left(x,r\right)e^{im\theta}e^{-i\omega t}, \tag{1.11a}$$

$$f\left(x,r,\theta,t\right)=\sum_{\omega}\sum_{m}\hat{f}_{\omega,m}\left(x,r\right)e^{im\theta}e^{-i\omega t}. \tag{1.11b}$$

Substituting these decompositions into equation (1.10) leads to an equation of the form

$$\mathcal{L}_{\omega,m}\hat{q}_{\omega,m}=\hat{f}_{\omega,m} \tag{1.12}$$

for each $(\omega,m)$ mode pair, where $\mathcal{L}_{\omega,m}=-i\omega I-\mathcal{A}_m$, and $\mathcal{A}_m$ is the operator $\mathcal{A}$ with $\frac{\partial}{\partial\theta}$ replaced by $im$. Note that no approximation has been made to this point; equation (1.12) exactly defines the jet if the forcing term $\hat{f}_{\omega,m}$, as well as the incoming fluctuations at the jet inlet, is exactly known.

A predictive model is obtained by replacing the exact forcing term and boundary conditions, as well as in general the baseflow $\bar{q}$, with user-specified approximations thereof. This is represented

schematically in Figure 1.2.

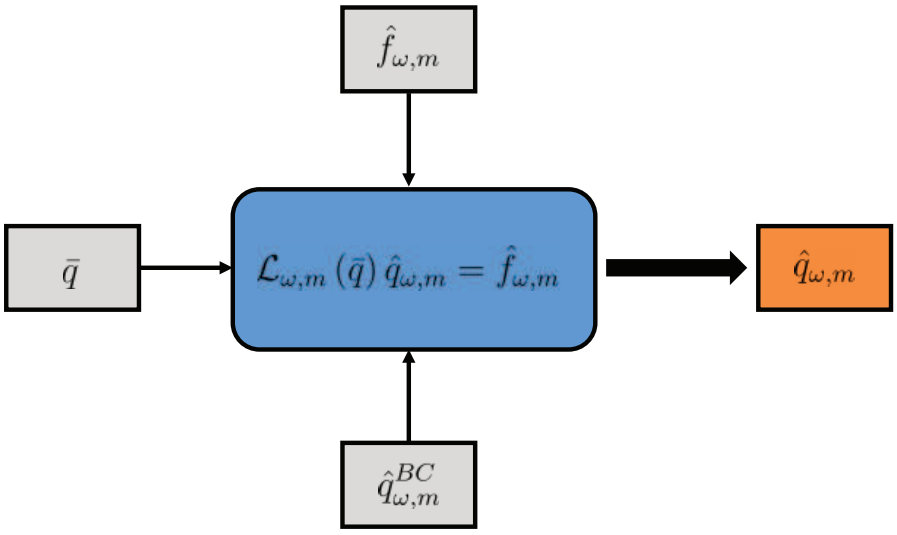


Figure 1.2: Schematic of the frequency domain wavepacket model given by equation (1.12). The model takes as inputs a baseflow $\bar{q}$, an inlet boundary condition $\hat{q}^{BC}_{\omega,m}$, and a volumetric forcing term $\hat{f}_{\omega,m}$, and returns $\hat{q}_{\omega,m}$.

#### 1.2.4.3 Solution methods

This thesis will focus on two aspects of the wavepacket modeling approach outlined above. First, irrespective of the various modeling choices, equation (1.12) must ultimately be solved for $\hat{q}_{\omega,m}$. This is an elliptic boundary-value problem. Numerical discretization in $x$ and $r$ leads to a large matrix equation of the form

$$\mathbf{L}_{\omega,m}\mathbf{q}_{\omega,m} = \mathbf{f}_{\omega,m}, \tag{1.13}$$

where the matrix $\mathbf{L}_{\omega,m}$ is the discrete representation of the operator $\mathcal{L}_{\omega,m}$, the vector $\mathbf{q}_{\omega,m}$ is the numerical approximation of $\hat{q}_{\omega,m}$, and the vector $\mathbf{f}_{\omega,m}$ contains the discrete representation of $\hat{f}_{\omega,m}$ as well as terms needed to enforce the boundary condition $\hat{q}^{BC}_{\omega,m}$. The size of $\mathbf{L}_{\omega,m}$ is proportional to the total number of spatial grid points (or an equivalent measure in non-collocation methods), which is typically $\mathcal{O}\left(10^5\right)$. Even though this matrix is sparse when sparse discretization methods

are used, solving equation (1.13), usually via LU decomposition, is computationally expensive in terms of CPU time, and even more so in terms of memory usage (see section 2.2.7.3 for an example).

An alternative approach is to revert to the time domain and time-step the equations, i.e., an azimuthally transformed version of equation (1.9), using an explicit time integrator, until the solution becomes statistically stationary. This avoids the need to solve a large matrix equation, but the number of time steps required to reach a stationary solution is extremely large because the linearized flow equations are notoriously stiff. See section 2.2.5 for more discussion on the computational scaling of these methods.

Because of the substantial computational cost of these direct solution methods, a number of alternative approaches have been employed to obtain low-cost, approximate solutions of equation (1.12) by leveraging the slow axial variation of the mean jet. Michalke (1971) and Mattingly & Chang (1974) applied classical linear stability theory to experimentally measured velocity profiles to compute local eigenvalues and found good agreement with experimental growth rate and wavenumber estimates. These methods also provided early insight into the key role of the Kelvin-Helmholtz instability and its sensitivity to various flow parameters. However, the local nature of such methods limits their ability to accurately capture nonparallel effects and the downstream growth and decay of the wavepackets, which are essential to sound production.

To address this limitation, a variety of weakly-nonparallel methods were developed based on the method of multiple scales (Crighton & Gaster 1976, Tam & Morris 1980) and matched asymptotic expansion (Tam & Burton 1984). These methods partially account for the slow divergence of the jet mean flow and deliver reasonable approximations of the wavepackets, especially in the near-field.

A simpler, more robust approach for incorporating slow mean flow divergence is an *ad hoc* generalization of linear stability theory called the parabolized stability equations (Herbert 1997). The efficiency of the method is achieved by using a spatial marching technique in the streamwise direction. Initial conditions are specified at the jet inlet and propagated downstream by integration of the equations.

The parabolized stability equations produce quantitatively accurate approximations of the

near-field wavepackets for both supersonic (Colonius et al. 2010, Sinha et al. 2014) and subsonic (Gudmundsson & Colonius 2011) turbulent jets. For supersonic jets, the far-field noise is also predicted with reasonable accuracy (Rodriguez et al. 2013, Sinha et al. 2014). On the other hand, the parabolized stability equations severely under-predict far-field noise for subsonic jets compared to direct solution methods (Cheung & Lele 2007).

In the first part of this thesis, we will develop alternative approximate solution methods that are inspired by the parabolized stability equations, but are able to properly capture acoustic radiation and other multi-modal effects.

#### 1.2.4.4 Nonlinear volumetric forcing

Second, this thesis will investigate the role and form of the nonlinear volumetric forcing term $\hat{f}_{\omega,m}$ on the wavepacket dynamics. In the majority of previous wavepacket models, this term is entirely neglected and wavepackets are excited exclusively by the boundary conditions at the nozzle inlet (Mohseni et al. 2002, Gudmundsson & Colonius 2011, Baqui et al. 2013, Sinha et al. 2014). The near-field wavepackets obtained from these homogeneous models show compelling agreement with those educed from experimental and simulation data for both subsonic and supersonic jets. For supersonic jets, these solutions also contain, with reasonable accuracy, the corresponding far-field acoustic radiation (Sinha et al. 2014). On the other hand, linear modal solutions for subsonic jets have been shown to under-predict far-field acoustic radiation by as much as 40 dB despite the close match in the near-field wavepacket (Baqui et al. 2013, Jordan et al. 2014).

The source of the discrepancy has been hypothesized to be 'jitter' of the wavepackets caused by one of several mechanisms that can be associated with nonlinear volumetric forcing of the wavepackets. The idea is that while the homogeneous linear models can predict reasonably the typical near-field wavepacket, small instantaneous modifications to these wavepackets (jitter) caused by nonlinear forcing can amplify their radiative efficiency. We will use LES data along with mode decomposition techniques to educe and analyze the actual forces experienced by wavepackets in a Mach 0.9 jet.

## 1.3 Contributions and outline

This thesis makes a number of specific contributions to the two aspects of the general wavepacket modeling approach described in the previous section. The summary of these contributions given here also serves as an outline for the remainder of the thesis.

Chapter 2 focuses on spatial integration methods that can be used to obtain approximate solutions of equation (1.12). In section 2.1, we analyze the parabolized stability equations in order to reveal the reason for their inability to capture acoustic radiation in subsonic jets. Specifically, we find that this is caused by the regularization that is required to resolve the well-known ill-posedness of the method. The results of this analysis can be used to qualitatively and quantitatively understand how any quasi-local instability mode of the linear flow equations is effected by the PSE parabolization.

In section 2.2, we introduce a new spatial integration method that can be used to efficiently model wavepackets in jets. Unlike PSE, the new method is well-posed and can capture both near-field wavepackets and their acoustic radiation. The method, which is inspired by outflow boundary conditions, is formulated for general hyperbolic equations and thus has potential applications in many fields of physics and engineering.

In section 2.3, a second well-posed spatial integration method is formulated that resolves two limitations of the first method. Of critical importance, the second method can accommodate inhomogeneous volumetric forcing terms. The foundation of the method is a particular projection operator that distinguishes between upstream and downstream waves. Again, it is formulated for a general hyperbolic system.

Chapter 3 investigates the role of nonlinear volumetric forcing on the dynamic and acoustic of wavepackets using data from a Mach 0.9 jet. To aid in the analysis, we formulate a novel data decomposition technique, called empirical resolvent-mode decomposition, that identifies modes that maximize the gain between input and output data sets. Using this method along with proper orthogonal decomposition, we find that, unlike the flow and acoustic fields, the forcing field lacks energetic coherent structures. The structures that do exist are inefficient sound sources. Instead, the forces that are most efficient at exciting loud wavepackets seem to take the form of random

turbulent fluctuations. This suggests that linear models that capture both the coherent flow and acoustic fields can be constructed if appropriate parameterizations of the turbulent forces can be found.

Finally, Chapter 4 summarizes the thesis and discusses some further extensions of the research.

# Chapter 2

# Spatial Integration Methods

This chapter focuses on spatial integration methods that can be used to obtain approximate solutions of equation (1.12). A spatial integration method is a solution technique in which perturbations are specified at some spatial location and propagated by spatially integrating an appropriate evolution equation in the frequency domain. Naturally, these methods can only capture waves that propagate in the direction of integration. In fact, as we'll discuss in detail throughout this chapter, waves that propagate in the opposite direction must be properly eliminated to achieve stability. For wavepacket-based jet noise models, computing only the downstream propagating waves is reasonable because both the dominant acoustic waves and the wavepackets that excite them are downstream propagating.

For wave propagation problems, spatial integration methods are often referred to as one-way equations. One-way approximations of various forms of the wave equations are routinely used in diverse fields, for example, geophysical migration (Claerbout 1976, 1985) and underwater acoustics (Collins 1989, Jensen et al. 2001). When transformed back to the time domain, they can also be used as approximate nonreflecting boundary conditions (Engquist & Majda 1977, Givoli 2004).

A number of spatial integration methods have been developed for solving the Euler and Navier-Stokes equations. One class of methods, collectively known as parabolized or reduced Navier-Stokes equations, relies on special treatment of the streamwise pressure gradient to obtain an equation that can be stably spatially integrated. A number of variations exist in which this term is treated differently, ranging from neglecting it partially (Korte 1991) or entirely (Rubin & Tannehill 1992)

to prescribing it based on experimental data (Rubin & Tannehill 1992) or empirical approximations. Classical boundary layer equations fall into this category.

As discussed in the introduction, the parabolized stability equations can be used to spatially integrate the linearized Euler or Navier-Stokes equations. We will introduce and analyze this method, with special focus on the reasons behind its inability to capture acoustic radiation, in section 2.1.

In sections 2.2 and 2.3, we introduce two novel spatial integration methods. Unlike the parabolized stability equations, these methods rigorously eliminate upstream propagating waves and are able to properly capture downstream propagating acoustic radiation. They are formulated for general hyperbolic equations and thus have potential applications in many fields of physics and engineering. In particular, we show that they offer a systematic, convergent alternative to the parabolized stability equations for wavepacket modeling.

## 2.1 Parabolized stability equations

The parabolized stability equations (PSE) have been widely used to compute wavepackets in mixing-layers (Day et al. 2001, Cheung & Lele 2009) and jets (Gudmundsson & Colonius 2011, Cavalieri et al. 2013, Sinha et al. 2014). As discussed in the introduction, these models provide rapid approximations of the near-field wavepackets, but for subsonic jets in particular, are unable to capture the associated acoustic radiation. To be clear, the comparison here is between the PSE solutions and direct solutions of equation (1.12). Whether the model predicts the actual sound levels observed in experiments or large-scale simulations depends critically on the model inputs regardless of the solution method (the role of one of these inputs, nonlinear volumetric forcing, is addressed in Chapter 3).

In the following subsections, we briefly review and summarize the PSE equations, their well-known ill-posedness, and the most common regularization techniques that are used to stabilize the method. Then, we give a novel presentation and analysis of the effect of these regularization techniques on acoustic waves, and more generally on any quasi-local mode of the flow equations.

### 2.1.1 A brief introduction to PSE

The fundamental assumption of the PSE method is that the axial behavior of the solution $\hat{q}_{\omega,m}$ can be decomposed into a rapidly-varying wave-like component and a slowly-varying modulation of this wave. This is embodied by the PSE ansatz:

$$\hat{q}_{\omega,m}(x,r) = \tilde{q}_{\omega,m}(x,r)\, e^{i\int \alpha^0_{\omega,m}(x)dx}. \tag{2.1}$$

This ansatz is similar to that of classical linear stability theory, except that here both the shape function $\tilde{q}_{\omega,m}$ and wavenumber $\alpha^0_{\omega,m}$ are allowed to vary in $x$. It also bears resemblance to WKB and multiple-scale expansions of $\hat{q}_{\omega,m}$, but PSE adopts a unique approach for computing the wavenumber and shape-function. There are two parts to this solution strategy. First, an additional constraint is imposed to eliminate the ambiguity associated with permitting $x$ variation in both the wavenumber and shape-function. The substantive goal of the constraint is to force the exponential term to capture as much of the streamwise variation as possible, thus rendering the shapefunction slowly-varying. The most common choice is to set $\alpha^0_{\omega,m}$ such that the logarithmic streamwise derivative of $\hat{q}_{\omega,m}$ matches the logarithmic streamwise derivative that would be obtained by classical linear stability theory, which leads to the constraint

$$\alpha^0_{\omega,m} = -i\frac{\int_r \|\tilde{q}_{\omega,m}\|^2 \frac{\partial}{\partial x}(\ln \tilde{q}_{\omega,m})\, dr}{\int_r \|\tilde{q}_{\omega,m}\|^2 dr}. \tag{2.2}$$

Finally, the PSE governing equations can be obtained by substituting equation (2.1) into equation (1.12) and neglecting axial second derivatives. This equation is then spatially integrated in $x$, while also iteratively enforcing equation (2.2), to yield $\tilde{q}_{\omega,m}$ and $\alpha^0_{\omega,m}$.

### 2.1.2 Ill-posedness and instability

It was noticed soon after the introduction of PSE that its spatial march is unstable if an explicit integrator, or an implicit integrator with a sufficiently small axial step-size, is used (Chang et al.

1991). This instability is a consequence of the fact that PSE is ill-posed as a spatial initial value problem due to the existence of upstream propagating modes within the PSE operator (Li & Malik 1996, 1997). In this section, we will illustrate this ill-posedness and summarize the most common regularization techniques used to stabilize the integration.

To introduce these issues, it is sufficient to use the Euler equations, which are the inviscid limit of equation (1.12), with zero forcing. Solving for the axial derivative term results in an equation of the form

$$\frac{\partial \hat{q}_{\omega,m}}{\partial x} = \mathcal{M}_{\omega,m}\hat{q}_{\omega,m}. \tag{2.3}$$

The operator $\mathcal{M}_{\omega,m}$ governs the spatial evolution of $\hat{q}_{\omega,m}$. We will drop the $(\omega, m)$ subscripts from here on out for notational simplicity. The essential features underpinning the ill-posedness of solving this equation, under the PSE ansatz, as a spatial initial-value-problem can be demonstrated by examining the eigenvalues of $\mathcal{M}$ for a spatially uniform baseflow $\bar{q}$ in two-dimensional Cartesian coordinates. These eigenvalues are

$$i\alpha^c = \frac{ik}{M_x}, \tag{2.4a}$$

$$i\alpha^{\pm}(z) = ik\,\frac{-M_x \pm \mu(z)}{1 - M_x^2}, \tag{2.4b}$$

where $M_x = \bar{u}_x/\bar{c}_\infty$ is the Mach number (which we assume for now to be subsonic), $k = \omega/\bar{c}_\infty$ is the reduced frequency, $\bar{c}_\infty$ is the sound speed of the baseflow, $\eta$ is the transverse Fourier wavenumber, $z = \eta/k$ is a scaled transverse wavenumber, and the function $\mu(z)$ is given by

$$\mu(z) = \sqrt{1 - (1 - M_x^2)z^2}. \tag{2.5}$$

The first eigenvalue, $i\alpha^c$, is a double root and describes the evolution of entropy and vorticity. These modes convect downstream with group velocity $\bar{u}_x$. The eigenvalues $i\alpha^{\pm}$ represent acoustic branches of the spectrum, consisting of acoustic waves propagating in all directions as well as evanes-

cent waves which decay exponentially in $y$. It can be easily verified (Hagstrom et al. 2007) that for all $z$, $i\alpha^{\pm}$ have positive and negative group velocities, respectively. These eigenvalues are shown graphically in Figure 2.1. The parts of the acoustic branches that lie along the stability boundary are the propagating acoustic waves, and the vertical parts are the evanescent modes. Although the preceding analysis is strictly valid only for a uniform baseflow, inhomogeneous flows like jets and mixing layers contain modes with the same qualitative properties as these uniform flow modes.

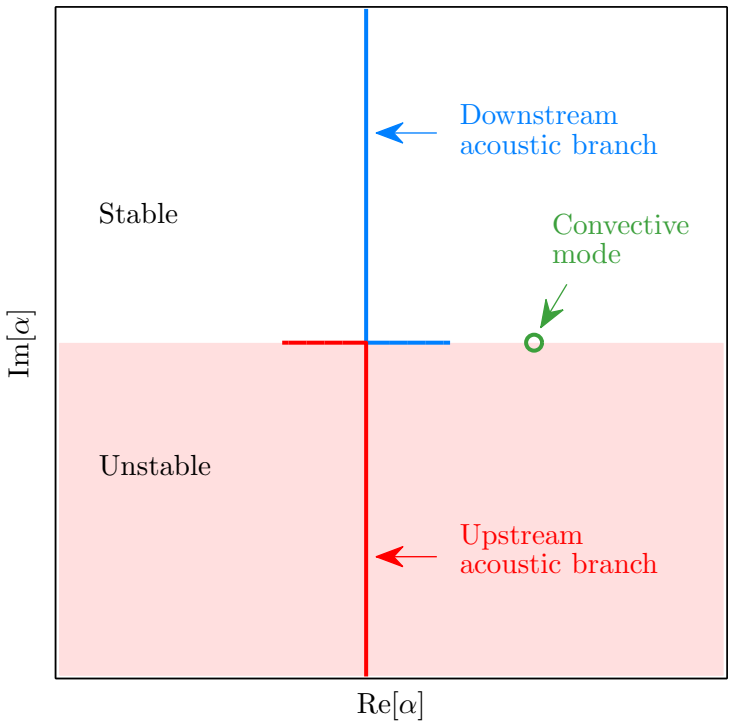


Figure 2.1: Spatial spectrum of the uniform flow Euler equations. The equations support downstream convective modes and downstream and upstream acoustic branches. The upstream acoustic branch makes spatial integration of the equations ill-posed.

Overall, the linearized Euler equations support three downstream propagating modes (double root of $i\alpha^c$ and $i\alpha^+$) and one upstream mode ($\alpha^-$). This result is reflective of the inherent boundary value nature of the subsonic Euler equations. For well-posedness, the downstream modes should be specified at the domain inlet and the upstream mode should be specified at the domain outlet.

If instead the problem is solved as an initial value problem in space – by specifying all modes at

the inlet and marching the solution downstream – the upstream acoustic mode will cause instability in the march. Functionally, this instability occurs because $i\alpha^-$ takes on complex values with negative imaginary part (see Figure 2.1), causing exponential growth of the mode as it is integrated in the positive $x$-direction. Applying the PSE ansatz does not change this; it results in a modified equation

$$\frac{\partial \tilde{q}}{\partial x} = \tilde{\mathcal{M}}\tilde{q}, \tag{2.6}$$

where $\tilde{\mathcal{M}} = \mathcal{M} - i\alpha^0 I$ (assuming a locally parallel flow). Therefore, the PSE ansatz simply shifts the eigenvalues of $\mathcal{M}$ by a constant factor equal to the PSE wavenumber.

### 2.1.3 Regularization

Several different regularization techniques have been proposed to stabilize PSE. The standard approach numerically damps the unstable upstream acoustic waves by using implicit Euler integration with a restriction on the *minimum* step size. This is illustrated in Figure 2.2. The gray region in each plot is the stability region of the implicit Euler integration, while the inner circle is the unstable region. If a sufficiently large step-size is used, the upstream acoustic branch falls entirely inside the region of stability, as shown in Figure 2.2(b). Therefore, the PSE equations can be stably integrated. However, if the step-size is made to be too small, part of the upstream branch enters the unstable region, as shown in Figure 2.2(c), and the integration becomes unstable once more. Therefore, there exists a minimum stable step-size. Using the uniform eigenvalues, the condition for stability is

$$\Delta x > \Delta x_0 = \frac{1}{\left|\mathrm{Re}\left[\alpha^0\right] + \dfrac{\omega M_x^2}{1 - M_x^2}\right|}. \tag{2.7}$$

Setting $M_x = 0$ recovers the more commonly quoted incompressible step-size restriction $\Delta x > 1 \,/\, \mathrm{Re}\left[\alpha^0\right]$.

Although this regularization technique successfully stabilizes the march, it has some serious drawbacks. For one, from Figure 2.2(d) we see that the propagative downstream acoustic modes,

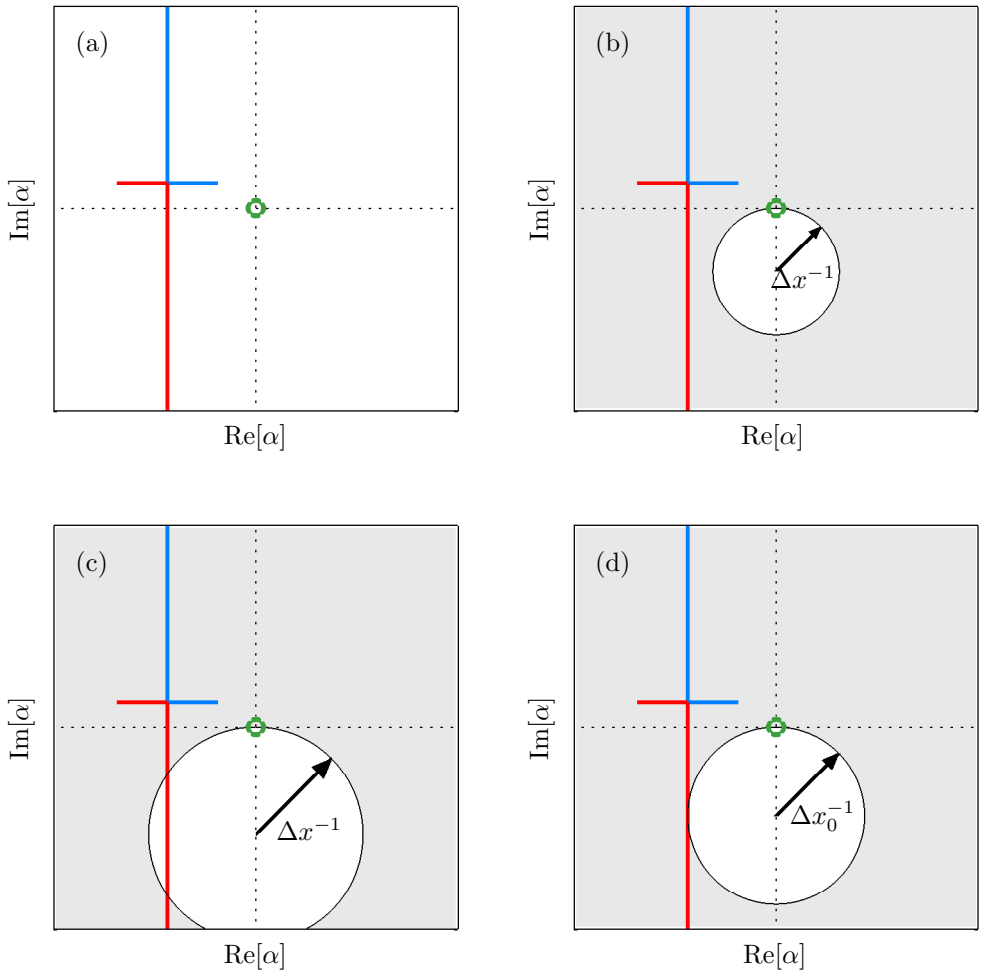


Figure 2.2: Damping of the uniform Euler equations by the implicit Euler PSE regularization. The shaded regions shows the stability region of the implicit Euler integrator. The convective mode (O) has been given a negative imaginary part to represent a convective instability. (a) The PSE wavenumber $\alpha^0$ has the effect of shifting the spectrum so that the convective mode sits at the origin. (b) Using a sufficiently large step-size numerically stabilizes the upstream acoustic branch (———). (c) If the step-size is reduced too much, the upstream acoustic branch again destabilizes the march. (d) Therefore, there exists a minimum step-size restriction for stability. Notice that at this step-size, the propagative part of the downstream acoustic branch (———), which should be neutrally stable, is damped.

which should be neutral, are numerically damped. This explains, for the first time, why PSE struggles to properly capture acoustic radiation. This is actually just one symptom of a more general issue – the minimum step-size restriction makes it impossible to numerically converge the solution. We

will quantify the effect of this in the next section. The inability to reach convergence is clearly an undesirable trait for any method, and the step-size restriction is especially problematic for nonlinear versions of PSE.

The inability to converge the PSE solution led to the conception of two alternative regularization techniques meant to alleviate or eliminate the step-size restriction while still maintaining stability. The first consists of neglecting the streamwise derivative of the pressure component of the shape-function (Chang et al. 1991, Haj-Hariri 1994, Li & Malik 1996). This reduces the minimum stable step-size by roughly an order of magnitude. However, since acoustic waves are inextricably linked to the pressure gradient (consider, for example, the wave equation), this technique has a devastating impact on acoustics. Therefore, we will not consider it further.

The second method stabilizes the PSE march by explicitly adding a damping term (Andersson et al. 1998). Specifically, equation (2.6) is replaced by the modified equation

$$\frac{\partial \tilde{q}}{\partial x} = \tilde{\mathcal{M}}\tilde{q} + s\tilde{\mathcal{M}}\frac{\partial \tilde{q}}{\partial x}, \tag{2.8}$$

where $s$ is a parameter that controls the magnitude of the new damping term. The condition for the stability of implicit Euler integration of this equation can be shown to be

$$\Delta x > \Delta x_0 - 2s, \tag{2.9}$$

where $\Delta x_0$ is given by equation (2.7). Therefore, the step-size restriction can be eliminated by setting $s = \Delta x_0/2$. Although this is useful, especially for nonlinear PSE, it does not resolve the issue at hand; we'll show in the next section that the acoustic eigenvalues, as well as other modes of $\mathcal{M}$, are still damped and distorted.

### 2.1.4 Eigenvalue error analysis

At its core, PSE is designed to track the spatial evolution of a *single* downstream-propagating wave, usually the most spatially-amplified wave supported by the system. This is inferred by the

identification of a single dominant slowly-varying wavelength and growth rate $\alpha^0$. In reality, however, $\mathcal{M}$ supports waves with a range of wavenumbers. This is evident for the uniform flow scenario introduced above, and real flows support even more diverse spectra. In this section, we will analyze the effect of the standard implicit Euler and explicit damping PSE regularization techniques on these other eigenvalues, which we refer to as "secondary" modes.

Our strategy for analyzing the standard implicit Euler regularization is to determine the spectrum that when exactly integrated produces the same solution as PSE when numerically integrated at the minimum allowable step-size. The properties of this spectrum, which we call the equivalent PSE spectrum (Towne & Colonius 2014), then quantify the treatment of the modes of the original operator by the standard PSE regularization.

The implicit Euler integration of standard PSE advances the coefficient $\psi$ of an arbitrary mode of $\mathcal{M}$ with eigenvalue $\imath\alpha$ as

$$\psi_{k+1} = \frac{1}{1 - \Delta x(\imath\alpha - \imath\alpha^0)} e^{\imath\alpha^0 \Delta x} \psi_k, \tag{2.10}$$

where here the subscript $k$ refers to the discrete axial position. Now consider a different operator that supports the same eigenvector but with a different eigenvalue $\imath\alpha^e$. The *exact* advancement of this mode (assuming locally parallel flow) is

$$\psi_{k+1} = e^{\imath\alpha^e \Delta x} \psi_k. \tag{2.11}$$

The effective eigenvalue $i\alpha^e$ describes the PSE approximation of $i\alpha$ if the propagators in equations (2.10) and (2.11) are equal:

$$e^{\imath\alpha^e \Delta x} = \frac{1}{1 - \Delta x(\imath\alpha - \imath\alpha^0)} e^{\imath\alpha^0 \Delta x}. \tag{2.12}$$

Solving for $\imath\alpha^e$ results in the following PSE approximation of $\imath\alpha$:

$$\imath\alpha^e = \imath\alpha^0 - \frac{1}{\Delta x}\log\left(1 - \Delta x(\imath\alpha - \imath\alpha^0)\right). \tag{2.13}$$

As $\Delta x \to 0$, the correct eigenvalue $\imath\alpha$ is recovered, but this limit cannot be approached because of the PSE step-size restriction. At a fixed $\Delta x$, the distortion of each eigenvalue depends on its distance from the primary eigenvalue $\alpha_0$ and the step-size. This error is represented graphically in Figure 2.3. Here, the magnitude of the difference between the original and effective PSE eigenvalue, scaled by the original eigenvalue (a.k.a. $|(\alpha^e - \alpha)/\alpha|$), is plotted as a function of the distance of the original eigenvalue from $\alpha_0$, scaled by $\Delta x$. The error is zero for $\alpha = \alpha^0$, implying that the dominant mode is perfectly captured. In reality, the constraint from equation (2.2) does not force $\alpha^0$ to precisely lock on to the true dominant instability mode, so the actual error in its representation is finite but small. This is why PSE can accurately approximate the dominant convective instabilities in many shear-flows. Moving away from $\alpha = \alpha^0$, the error quickly becomes large; the radius of the region where the error is less than 30% is less than one. For comparison, the range of relevant wavenumbers in jets is $\mathcal{O}(10)$. The conclusion, then, is that standard PSE can accurately capture only modes that lie within a narrow range of wavenumbers and growth rates surrounding the dominant mode. We will use this analysis to specifically address the PSE treatment of acoustic waves later in this section.

Quantifying the effect of the explicit damping regularization technique on secondary modes is straightforward. The eigenvalues of the damped system in equation (2.8) take the form

$$i\alpha^s = i\alpha^0 + \frac{i\alpha - i\alpha^0}{1 - s\,(i\alpha - i\alpha^0)}, \tag{2.14}$$

where $i\alpha$ is again any eigenvalue of $\mathcal{M}$.

We set $s = \Delta x_0/2$ so as to remove the step-size restriction. Then, since the resulting system can be exactly integrated, we can make direct comparisons between $\alpha^s$ and $\alpha$. The scaled error $|(\alpha^s - \alpha)/\alpha|$ is plotted in Figure 2.4 as a function of $\Delta x_0$ and the distance of the original eigenvalue

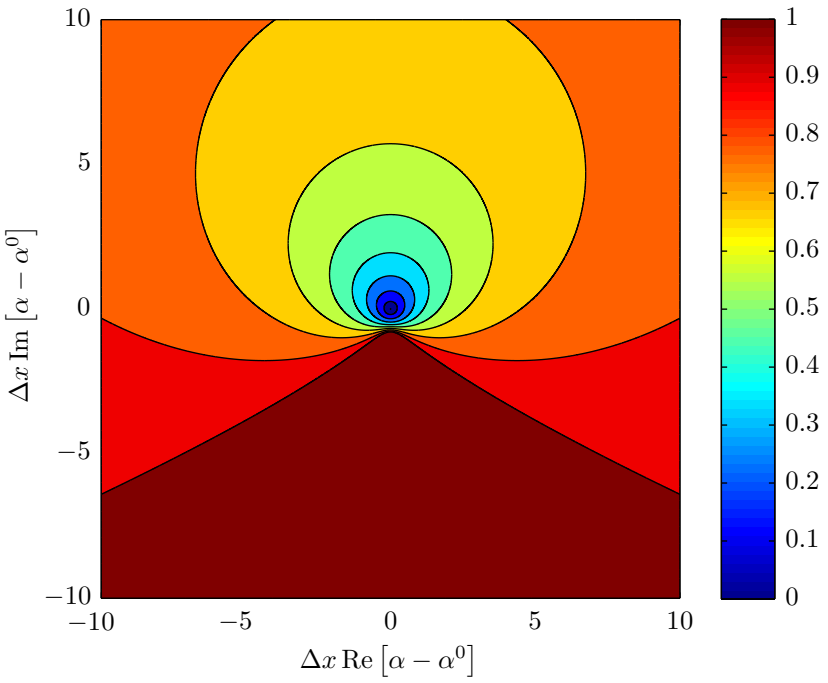


Figure 2.3: Eigenvalue error as a function of $\alpha$ and $\Delta x$ for PSE with implicit Euler regularization. The definition of the error is given in the text.

from $\alpha_0$. The story is the same for the explicit damping method as it was for the implicit Euler method – the dominant mode and its near-neighbors can be accurately captured while all other modes will be dominated by error.

Next, this general analysis is applied to the uniform flow acoustic modes given in equation (2.4b). We set $M_x = 0$, corresponding to a quiescent fluid. These eigenvalues provide a reasonable, analytical approximation of the far-field acoustic modes that exist in many real flows. For this analysis, a specific value must be specified for $\alpha^0/k$. We choose $k/\alpha^0 = 0.6$ to match the approximate convection velocity of wavepackets in high-subsonic jets.

The exact eigenvalues and the eigenvalues associated with the three regularization techniques, scaled by $k = \omega/\bar{c}$, are plotted in Figure 2.5 as a function of the scaled transverse wavenumber $z = \eta/k$. The real part of $\alpha/k$ is the inverse axial phase-speed, while the imaginary part gives the damping. For $z < 1$, the exact eigenvalues have zero imaginary part – these are propagating acoustic waves. For $z > 1$, the modes are evanescent.

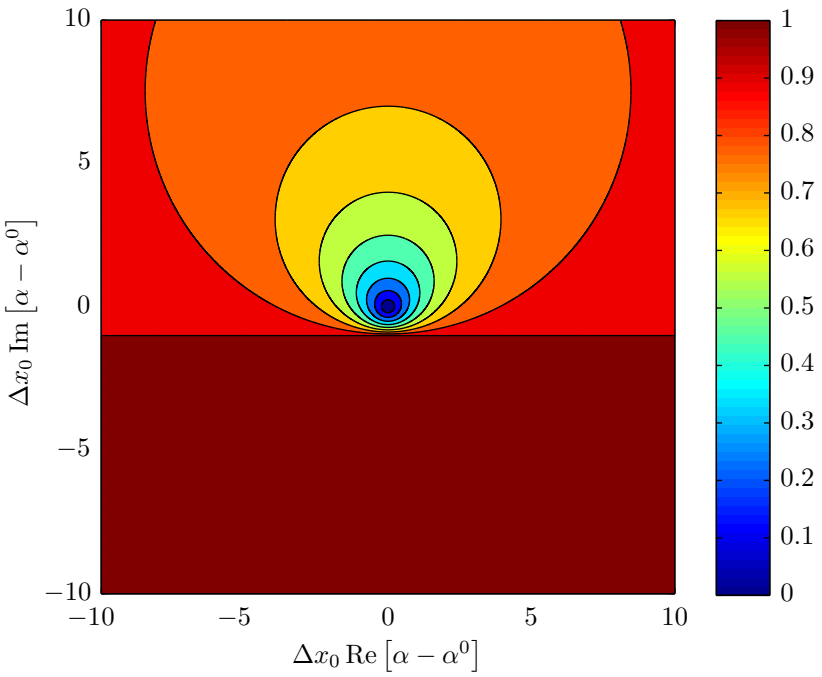


Figure 2.4: Eigenvalue error as a function of $\alpha$ and $\Delta x$ for PSE with explicit damping regularization. The definition of the error is given in the text.

Both versions of PSE underestimate the phase-speed of the propagating waves and cause erroneous damping. To get a grasp on the level of damping, note that the wave will dissipate by a factor of $\exp(-\operatorname{Im}[\alpha])$ per acoustic wavelength of axial propagation distance. Taking $\operatorname{Im}[\alpha] \approx 0.2$ as an estimate for the typical damping of the two PSE methods gives an estimated loss of approximately 2 dB per wavelength of propagation.

Finally, we note that Figures 2.3 and 2.4 give a hint as to why PSE is able to partially capture acoustic radiation in supersonic jets, but not in subsonic jets. In these jets, the dominant mode is associated with the well-known Kelvin-Helmholtz instability. Therefore, modes that are farther from the Kelvin-Helmholtz mode in the $\alpha$ plane are more seriously damaged. The lower phase-speed of the Kelvin-Helmholtz mode in subsonic jets increases the distance of this mode from the sonically-propagating downstream acoustic modes, effectively increasing the error compared to supersonic jets. We will show this quantitatively in section 2.2.8.1.

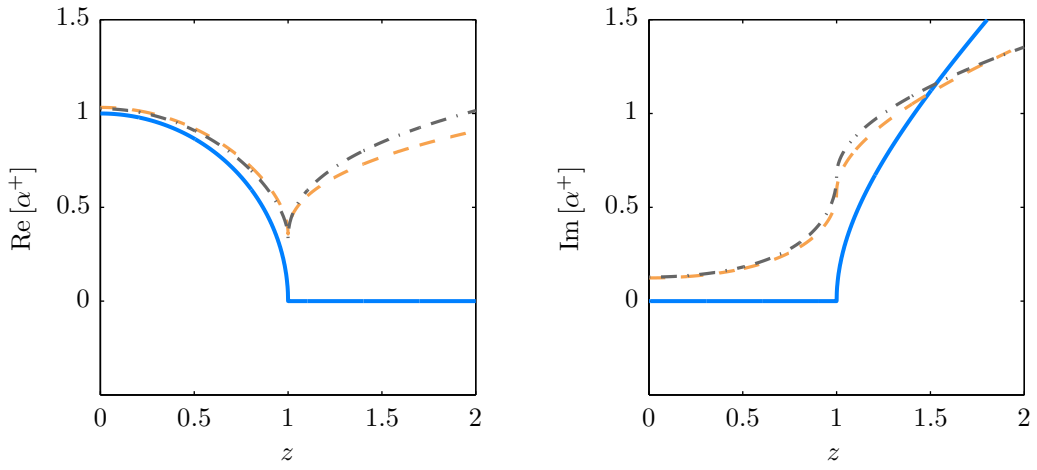


Figure 2.5: Uniform flow Euler downstream acoustic eigenvalue $\alpha_+$ as a function of the scaled transverse wavenumber $z$. The PSE wavenumber has been set to $\alpha_0 = 1/0.6$: exact (———); Standard PSE (– – –); PSE with explicit damping (– – –).

## 2.2 One-way spatial integration – an outflow approach

Motivated by the computational efficiency of PSE, in this section we develop a new spatial marching method that can be used to compute wavepackets *and* their acoustic radiation. This is accomplished by formally removing support for upstream-traveling waves from the equations using concepts related to outflow boundary conditions, resulting in well-posed equations that can be solved by spatial marching without the need for additional regularization. As a result, downstream acoustic modes, as well as all other downstream-traveling waves, are accurately retained, allowing far-field acoustic radiation to be properly captured.

We will formulate the method for a general hyperbolic system. This generality helps place the method on firm theoretical ground and opens up applications in many fields of study. To reflect this generality, we replace our downstream/upstream terminology with the universal terms rightgoing and leftgoing.

After setting up the problem in section 2.2.1, we first derive exact one-way equations in section 2.2.2 based on concepts related to the well-posedness of hyperbolic boundary value problems and then in section 2.2.3 show how the exact equations can be efficiently approximated using tech-

niques that were originally developed for generating high-order nonreflecting boundary conditions. The method is applied to the Euler equations in section 2.2.6, and the accuracy and efficiency of the resulting one-way Euler equations is demonstrated in section 2.2.7 using three example problems. The method is applied to jets in section 2.2.8. Finally, we summarize the method in section 2.2.9.

### 2.2.1 Problem formulation

We begin with a system of linear, strongly hyperbolic partial differential equations:

$$\frac{\partial q}{\partial t} + A\left(x,y\right)\frac{\partial q}{\partial x} + \sum_{j=1}^{d-1} B_j\left(x,y\right)\frac{\partial q}{\partial y_j} + C\left(x,y\right)q = 0. \tag{2.15}$$

Here, $x \in \mathbb{R}$ is the axis along which we will parabolize the equations, $y = \{y_1, \ldots, y_{d-1}\} \in \mathbb{R}^{d-1}$ are additional, transverse spatial dimensions, and $d$ is the total spatial dimensionality of the problem. The coefficients $A$, $B_j$, $C \in \mathbb{C}^{N_q \times N_q}$ are smooth matrix functions of $x$ and $y$ and do not depend on $t$. The vector $q = q(x,y,t) \in \mathbb{C}^{N_q}$ is the solution to be determined.

We discretize equation (2.15) in the transverse directions using a total of $N_y$ degrees of freedom. Standard finite difference discretizations are used throughout this thesis, but in principle any collocation method could be used. We represent the discrete analog of each continuous variable and operator with a bold variable of the same name. The semi-discrete approximation of equation (2.15) can then be written

$$\frac{\partial \boldsymbol{q}}{\partial t} + \boldsymbol{A}\left(x\right)\frac{\partial \boldsymbol{q}}{\partial x} + \boldsymbol{B}\left(x\right)\boldsymbol{q} = 0, \tag{2.16}$$

where $\boldsymbol{B} = \sum_{j=1}^{d-1} \boldsymbol{B}_j \boldsymbol{D}_j + \boldsymbol{C}$ and the matrix $\boldsymbol{D}_j$ approximates the derivative $\frac{\partial}{\partial y_j}$. At this point, transverse boundary conditions must also be incorporated into $\boldsymbol{B}$. It is important that these boundary conditions do not alter the structure of $\boldsymbol{A}$. Common options such as damping layers, perfectly matched layers, and characteristic boundary conditions satisfy this requirement.

Equation (2.16) is a one-dimensional strongly hyperbolic system. In other words, $\boldsymbol{A}$ is diagonalizable and has real eigenvalues. This follows from the fact that the entries of $\boldsymbol{A}$ are a discrete

sampling of the continuous matrix $A$. Specifically, $\boldsymbol{A}$ can be written as a block-diagonal matrix, where each block contains the matrix $A$ evaluated at one of the collocation points. This structure guarantees that $\boldsymbol{A}$ is diagonalizable and that its eigenvalues are real, since they are precisely the eigenvalues of $A$ at the collocation points.

In the preceding development, equation (2.16) inherited strong hyperbolicity from equation (2.15). This is not, however, the only way to arrive at a system equivalent to equation (2.16). For example, higher order $y$ derivatives could be added to equation (2.15), destroying its hyperbolicity, without destroying the hyperbolicity of equation (2.16). The method described in the remainder of this paper can be applied to any linear, one-dimensional, strongly hyperbolic equation, regardless of its origin.

For simplicity, we restrict our attention to the case in which $\boldsymbol{A}$ is invertible for all $x$. This restriction is not necessary but simplifies the discussion. The case where $\boldsymbol{A}$ is singular is treated in Towne & Colonius (2015). Under this assumption, the number of positive and negative eigenvalues of $\boldsymbol{A}$ is fixed for all $x$, and we denote these quantities as $N_+$ and $N_-$, respectively. The total size of the semi-discrete system is $N = N_q N_y = N_+ + N_-$.

It proves useful to work with the characteristic variables of equation (2.16). Since $\boldsymbol{A}$ is diagonalizable, there exists a transformation $\boldsymbol{T}(x)$ such that

$$\boldsymbol{T}\boldsymbol{A}\boldsymbol{T}^{-1} = \tilde{\boldsymbol{A}} = \begin{bmatrix} \tilde{\boldsymbol{A}}_{++} & \boldsymbol{0} \\ \boldsymbol{0} & \tilde{\boldsymbol{A}}_{--} \end{bmatrix}, \tag{2.17}$$

where $\tilde{\boldsymbol{A}}_{++} \in \mathbb{R}^{N_+ \times N_+} > 0$, $\tilde{\boldsymbol{A}}_{--} \in \mathbb{R}^{N_- \times N_-} < 0$, and $\tilde{\boldsymbol{A}}$ are diagonal matrices. The diagonal entries of $\tilde{\boldsymbol{A}}_{++}$ and $\tilde{\boldsymbol{A}}_{--}$ are precisely the positive and negative eigenvalues of $\boldsymbol{A}$, respectively. The transformation $\boldsymbol{T}$ is known analytically since it is the discretization of the matrix $T$ that diagonalizes $A$.

The characteristic variables of equation (2.16) are then $\boldsymbol{\phi}(x,t) = \boldsymbol{T}(x)\boldsymbol{q}(x,t)$, and can be sepa-

rated into positive and negative parts based on the positive and negative blocks of $\boldsymbol{A}$:

$$\boldsymbol{\phi} = \left\{ \begin{array}{c} \boldsymbol{\phi}_+ \\ \boldsymbol{\phi}_- \end{array} \right\} \tag{2.18}$$

with $\boldsymbol{\phi}_+ \in \mathbb{R}^{N_+}$ and $\boldsymbol{\phi}_- \in \mathbb{R}^{N_-}$. In terms of the characteristic variables, equation (2.16) becomes

$$\frac{\partial \boldsymbol{\phi}}{\partial t} + \tilde{\boldsymbol{A}}(x) \frac{\partial \boldsymbol{\phi}}{\partial x} + \tilde{\boldsymbol{B}}(x) \boldsymbol{\phi} = \boldsymbol{0}, \tag{2.19}$$

where $\tilde{\boldsymbol{B}} = \boldsymbol{T}\boldsymbol{B}\boldsymbol{T}^{-1} + \tilde{\boldsymbol{A}}\boldsymbol{T}\frac{d\boldsymbol{T}^{-1}}{dx}$.

Since we wish to obtain a one-way equation in the frequency domain, we proceed by applying a Laplace transform in time to equation (2.19), giving

$$s\,\hat{\boldsymbol{\phi}} + \tilde{\boldsymbol{A}}(x) \frac{\partial \hat{\boldsymbol{\phi}}}{\partial x} + \tilde{\boldsymbol{B}}(x) \hat{\boldsymbol{\phi}} = 0, \tag{2.20}$$

where $\hat{\boldsymbol{\phi}}(x, s)$ is the Laplace transform of $\boldsymbol{\phi}(x, t)$ and $s = \eta - i\omega$ $(\eta, \omega \in \mathbb{R})$ is the Laplace dual of $t$. We have assumed zero initial conditions, but that is unimportant since we are only interested in the long-time stationary behavior of the solution. We will ultimately take $\eta = 0$ and set $\omega$ to a particular value to obtain the stationary solution at that frequency, but keeping the possibility of non-zero $\eta$ will help us distinguish between upstream and downstream solutions of equation (2.19).

Solving equation (2.20) for $x$-derivatives gives

$$\frac{d\hat{\boldsymbol{\phi}}}{dx} = \boldsymbol{M}(x, s)\,\hat{\boldsymbol{\phi}} \tag{2.21}$$

with

$$\boldsymbol{M} = -\tilde{\boldsymbol{A}}^{-1}\left(s\boldsymbol{I} + \tilde{\boldsymbol{B}}\right). \tag{2.22}$$

It is useful to partition $\boldsymbol{M}$ into blocks according to the sizes of the positive and negative characteristic

variables:

$$\frac{d}{dx}\left\{\begin{array}{c}\hat{\boldsymbol{\phi}}_+\\ \hat{\boldsymbol{\phi}}_-\end{array}\right\} = \left[\begin{array}{cc}\boldsymbol{M}_{++} & \boldsymbol{M}_{+-}\\ \boldsymbol{M}_{-+} & \boldsymbol{M}_{--}\end{array}\right]\left\{\begin{array}{c}\hat{\boldsymbol{\phi}}_+\\ \hat{\boldsymbol{\phi}}_-\end{array}\right\}. \tag{2.23}$$

The size of each block is implied by the subscripts; for example, $\boldsymbol{M}_{+-} \in \mathbb{C}^{N_+ \times N_-}$. We will continue to use this convention throughout the paper.

### 2.2.2 Exact one-way equation

In this subsection, we show that there exists an exact parabolization of equation (2.21) for the special case in which $\boldsymbol{M}$ is not a function of $x$. The method will be extended to $x$-dependent operators in section 2.2.4. We also assume that $\boldsymbol{M}$ is diagonalizable. It is shown in Appendix B that the methods developed for diagonalizable matrices can be applied without modification to systems in which $\boldsymbol{M}$ is defective.

The essential step in parabolizing equation (2.21) is distinguishing between its rightgoing and leftgoing solutions. Since equation (2.21) is uniform in $x$, its general solution is the summation of modes

$$\hat{\boldsymbol{\phi}}(x,s) = \sum_{k=1}^{N} \boldsymbol{v}_k(s)\boldsymbol{\psi}_k(x,s), \tag{2.24}$$

where each expansion coefficient $\boldsymbol{\psi}_k$ satisfies

$$\frac{d\boldsymbol{\psi}_k}{dx} = i\alpha_k(s)\boldsymbol{\psi}_k, \tag{2.25}$$

and each $(i\alpha_k, \boldsymbol{v}_k)$ is an eigenvalue-eigenvector pair of $\boldsymbol{M}$. We include the $i$ in our definition of the eigenvalue for consistency with the usual definition of spatial wave-numbers. The real and imaginary parts of $\alpha_k$ are related to the phase-speed and spatial growth rate of the mode.

The task at hand is to determine which of these modes are rightgoing and which are leftgoing, in terms of energy transfer. Briggs (Briggs 1964) developed a criterion for making this distinction:

mode $k$ is rightgoing if

$$\lim_{\eta \to +\infty} \mathrm{Im}\left[\alpha_k(s)\right] = +\infty \tag{2.26}$$

and leftgoing if

$$\lim_{\eta \to +\infty} \mathrm{Im}\left[\alpha_k(s)\right] = -\infty. \tag{2.27}$$

Since $\boldsymbol{M}$ tends to the real diagonal matrix $-\eta \tilde{\boldsymbol{A}}^{-1}$ as $\eta \to +\infty$, it is clear that all of its eigenvalues will exhibit one of these two behaviors. Furthermore, based on the block structure of $\tilde{\boldsymbol{A}}$, there are exactly $N_+$ rightgoing modes and $N_-$ leftgoing modes. When applied to an operator obtained from a constant coefficient hyperbolic system such as equation (2.21), Briggs' criterion is consistent with well-posedness theory for hyperbolic systems as developed by Kreiss (1970).

The exact parabolization of equation (2.21) is obtained by zeroing the leftgoing modes. That is, for each leftgoing mode, equation (2.25) is replaced with the condition

$$\boldsymbol{\psi}_k = 0. \tag{2.28}$$

This is exactly the same condition that is applied to each incoming mode in order to generate nonreflecting boundary conditions at an outflow. Indeed, our parabolization technique can be thought of as applying a nonreflecting outflow boundary condition not just at the boundary, but to the entire domain, since we wish to disallow leftgoing solutions everywhere to achieve a well-posed spatial march.

In order to write the one-way equation clearly and compactly, it is useful to write it in block matrix form. First, the expansion coefficients are arranged in a vector $\boldsymbol{\psi}$ such that the $N_+$ rightgoing

modes appear first followed by the $N_-$ leftgoing modes:

$$\boldsymbol{\psi} = \left\{ \begin{array}{c} \boldsymbol{\psi}_+ \\ \boldsymbol{\psi}_- \end{array} \right\}. \tag{2.29}$$

Then equations (2.24) - (2.25) can be written in matrix form as

$$\hat{\boldsymbol{\phi}} = \boldsymbol{V}\boldsymbol{\psi} \quad \leftrightarrow \quad \boldsymbol{\psi} = \boldsymbol{U}\hat{\boldsymbol{\phi}} \tag{2.30}$$

and

$$\frac{d\boldsymbol{\psi}}{dx} = \boldsymbol{D}\boldsymbol{\psi}. \tag{2.31}$$

The columns of $\boldsymbol{V}$ are the right eigenvectors, the rows of $\boldsymbol{U} = \boldsymbol{V}^{-1}$ are the left eigenvectors, and the entries of the diagonal matrix $\boldsymbol{D}$ are the eigenvalues of $\boldsymbol{M}$, all ordered in the same way as $\boldsymbol{\psi}$, such that $\boldsymbol{M} = \boldsymbol{V}\boldsymbol{D}\boldsymbol{U}$.

We can also partition the matrices $\boldsymbol{V}$, $\boldsymbol{U}$, and $\boldsymbol{D}$ into blocks based on their association with the upstream and downstream expansion coefficients and the positive and negative characteristic variables. Specifically, we write

$$\left\{ \begin{array}{c} \hat{\boldsymbol{\phi}}_+ \\ \hat{\boldsymbol{\phi}}_- \end{array} \right\} = \left[ \begin{array}{cc} \boldsymbol{V}_{++} & \boldsymbol{V}_{+-} \\ \boldsymbol{V}_{-+} & \boldsymbol{V}_{--} \end{array} \right] \left\{ \begin{array}{c} \boldsymbol{\psi}_+ \\ \boldsymbol{\psi}_- \end{array} \right\}, \tag{2.32}$$

$$\left\{ \begin{array}{c} \boldsymbol{\psi}_+ \\ \boldsymbol{\psi}_- \end{array} \right\} = \left[ \begin{array}{cc} \boldsymbol{U}_{++} & \boldsymbol{U}_{+-} \\ \boldsymbol{U}_{-+} & \boldsymbol{U}_{--} \end{array} \right] \left\{ \begin{array}{c} \hat{\boldsymbol{\phi}}_+ \\ \hat{\boldsymbol{\phi}}_- \end{array} \right\}, \tag{2.33}$$

and

$$\frac{d}{dx} \left\{ \begin{array}{c} \boldsymbol{\psi}_+ \\ \boldsymbol{\psi}_- \end{array} \right\} = \left[ \begin{array}{cc} \boldsymbol{D}_{++} & \boldsymbol{0} \\ \boldsymbol{0} & \boldsymbol{D}_{--} \end{array} \right] \left\{ \begin{array}{c} \boldsymbol{\psi}_+ \\ \boldsymbol{\psi}_- \end{array} \right\}. \tag{2.34}$$

Recall that based on our ordering of $\boldsymbol{\psi}$, $\boldsymbol{D}_{++}$ contains the rightgoing eigenvalues and $\boldsymbol{D}_{--}$ contains the leftgoing eigenvalues. We make one additional assumption: that the matrices $\boldsymbol{U}_{++}$, $\boldsymbol{U}_{--}$, $\boldsymbol{V}_{++}$, and $\boldsymbol{V}_{--}$ are full-rank for all $\eta \geq 0$. We discuss the meaning of this assumption and implications of its violation in Appendix B.

The exact parabolization of equation (2.21), in terms of $\boldsymbol{\psi}$, is

$$\frac{d\boldsymbol{\psi}_+}{dx} = \boldsymbol{D}_{++}\boldsymbol{\psi}_+, \tag{2.35a}$$

$$\boldsymbol{\psi}_- = \boldsymbol{0}. \tag{2.35b}$$

This can also be written in terms of the characteristic variables as

$$\frac{d\hat{\boldsymbol{\phi}}_+}{dx} = \boldsymbol{M}_{++}\hat{\boldsymbol{\phi}}_+ + \boldsymbol{M}_{+-}\hat{\boldsymbol{\phi}}_-, \tag{2.36a}$$

$$\boldsymbol{U}_{-+}\hat{\boldsymbol{\phi}}_+ + \boldsymbol{U}_{--}\hat{\boldsymbol{\phi}}_- = \boldsymbol{0}. \tag{2.36b}$$

Equation (2.36) is a differential-algebraic system of index 1, so $\hat{\boldsymbol{\phi}}_-$ can be eliminated, giving an ordinary differential equation for the positive characteristic variable:

$$\frac{d\hat{\boldsymbol{\phi}}_+}{dx} = \boldsymbol{M}^*_{++}\hat{\boldsymbol{\phi}}_+, \tag{2.37}$$

where

$$\boldsymbol{M}^*_{++} = \boldsymbol{M}_{++} - \boldsymbol{M}_{+-}\boldsymbol{U}_{--}^{-1}\boldsymbol{U}_{-+} \tag{2.38a}$$

$$= \begin{bmatrix} \boldsymbol{M}_{++} & \boldsymbol{M}_{+-} \end{bmatrix} \begin{bmatrix} \boldsymbol{I} \\ -\boldsymbol{U}_{--}^{-1}\boldsymbol{U}_{-+} \end{bmatrix} \tag{2.38b}$$

$$= \begin{bmatrix} \boldsymbol{V}_{++} & \boldsymbol{V}_{+-} \end{bmatrix} \begin{bmatrix} \boldsymbol{D}_{++} & \boldsymbol{0} \\ \boldsymbol{0} & \boldsymbol{D}_{--} \end{bmatrix} \begin{bmatrix} \boldsymbol{U}_{++} & \boldsymbol{U}_{+-} \\ \boldsymbol{U}_{-+} & \boldsymbol{U}_{--} \end{bmatrix} \begin{bmatrix} \boldsymbol{I} \\ -\boldsymbol{U}_{--}^{-1}\boldsymbol{U}_{-+} \end{bmatrix} \tag{2.38c}$$

$$= \begin{bmatrix} \boldsymbol{V}_{++} & \boldsymbol{V}_{+-} \end{bmatrix} \begin{bmatrix} \boldsymbol{D}_{++} & \boldsymbol{0} \\ \boldsymbol{0} & \boldsymbol{D}_{--} \end{bmatrix} \begin{bmatrix} \boldsymbol{V}_{++}^{-1} \\ \boldsymbol{0} \end{bmatrix} \tag{2.38d}$$

$$= \boldsymbol{V}_{++}\boldsymbol{D}_{++}\boldsymbol{V}_{++}^{-1}. \tag{2.38e}$$

In going from the third to fourth line, we made use of the identity $\boldsymbol{V}_{++}^{-1} = \boldsymbol{U}_{++} - \boldsymbol{U}_{+-}\boldsymbol{U}_{--}^{-1}\boldsymbol{U}_{-+}$. It is clear from the final equality that the eigenvalues of $\boldsymbol{M}^*_{++}$ are precisely the downstream eigenvalues of $\boldsymbol{M}$. The one-way equation is therefore well-posed and admits the proper rightgoing solutions.

Implementation of the exact one-way equation given by equation (2.36) would require calculation of the $N_-$ left eigenvectors corresponding to the leftgoing eigenvalues of $\boldsymbol{M}$. The resulting computational cost would usually be intolerably high. This is especially true for $x$-dependent systems, in which case local eigenvectors would need to to be recalculated at each $x$ (see section 2.2.4). Instead, we will generate a practical one-way equation by approximating the parabolization condition given by equation (2.36b).

### 2.2.3 Approximate one-way equation

Motivated by the connection between the exact one-way equation and nonreflecting boundary conditions, our approximate parabolization method is based on recursions that were introduced by Givoli & Neta (2003) and Hagstrom & Warburton (2004) for generating nonreflecting boundary conditions. Accordingly, we propose an approximate one-way equation given by the differential-algebraic

system

$$\frac{d\hat{\boldsymbol{\phi}}_+}{dx} = \boldsymbol{M}_{++}\hat{\boldsymbol{\phi}}_+ + \boldsymbol{M}_{+-}\hat{\boldsymbol{\phi}}_-, \tag{2.39a}$$

$$\left(\boldsymbol{M} - i\beta_+^j \boldsymbol{I}\right)\hat{\boldsymbol{\phi}}^j = \left(\boldsymbol{M} - i\beta_-^j \boldsymbol{I}\right)\hat{\boldsymbol{\phi}}^{j+1} \qquad j = 0, \ldots, N_\beta - 1, \tag{2.39b}$$

$$\hat{\boldsymbol{\phi}}_-^{N_\beta} = 0. \tag{2.39c}$$

In this formulation, we have introduced a set of auxiliary variables $\{\hat{\boldsymbol{\phi}}^j : j = 0, \ldots, N_\beta\}$ and a set of complex scalar parameters $\{\beta_+^j, \beta_-^j : j = 0, \ldots, N_\beta - 1\}$. The zero-indexed variable is the physical variable ($\hat{\boldsymbol{\phi}}^0 = \hat{\boldsymbol{\phi}}$) and the remaining auxiliary variables are defined by the recursions. The selection of the recursion parameters will be discussed below. We call $N_\beta$ the order of the approximate one-way equation.

To verify that equation (2.39) is well-posed as a one-way equation, we examine its behavior in the limit as $\eta$ becomes large in accordance with Briggs' criterion. We stipulate that the recursion parameters remain bounded in this limit, which places no practical restriction on their values since they need only be defined at $\eta = 0$, and can be formally continued in any convenient manner for $\eta > 0$. Then, for sufficiently large $\eta$, equation (2.39b) is dominated by the terms involving $\boldsymbol{M}$, and we conclude that $\hat{\boldsymbol{\phi}}^j = \hat{\boldsymbol{\phi}}^{j+1}$ for all $j$. Then equation (2.39c) implies that $\hat{\boldsymbol{\phi}}_- = 0$, which when applied to equation (2.39a) eliminates the second term on the right-hand-side. For large $\eta$, $\boldsymbol{M}_{++}$ tends to the real, negative matrix $-\eta\tilde{\boldsymbol{A}}_{++}^{-1}$. All of the eigenvalues of this final matrix have $\alpha$ with positive imaginary part. Therefore, by construction, equation (2.39) admits only rightgoing modes and is well-posed as a one-way equation.

This represents a fundamental difference between the frequency domain one-way equations pursued in this paper and time domain one-way equations that are often used as nonreflecting boundary conditions. In the time domain case, any parameters that arise in the formulation must be specified as explicit functions of $s$ in order for the equations to be transformed back into the time domain. As a result, the choice of parameters critically effects the well-posedness of the approximate equations (Trefethen & Halpern 1986). In contrast, the recursion parameters do not effect the well-posedness

of our frequency domain one-way equations, allowing for great flexibility in the parameter selection process.

Next, we show that the approximate one-way equation converges to the exact one-way equation as the order of the approximation increases, provided that the recursion parameters are appropriately chosen. Since equation (2.39a) is identical to equation (2.36a), we must only show that equation (2.39b) and equation (2.39c) together converge to equation (2.36b). In other words, we wish to show that $\boldsymbol{\psi}_- \to 0$ as $N_\beta \to \infty$. To do so, we begin by defining $\boldsymbol{\psi}^j = \boldsymbol{U}\hat{\boldsymbol{\phi}}^j$, which is the natural extension of the previous definition $\boldsymbol{\psi} = \boldsymbol{U}\hat{\boldsymbol{\phi}}$. Equation (2.39b) can then be written

$$\left(\boldsymbol{D} - i\beta_+^j \boldsymbol{I}\right)\boldsymbol{\psi}^j = \left(\boldsymbol{D} - i\beta_-^j \boldsymbol{I}\right)\boldsymbol{\psi}^{j+1} \qquad j = 0, \ldots, N_\beta - 1. \tag{2.40}$$

Since $\boldsymbol{D}$ is diagonal, each scalar component of $\boldsymbol{\psi}^j$ can be considered separately:

$$\left(i\alpha_k - i\beta_+^j\right)\boldsymbol{\psi}_k^j = \left(i\alpha_k - i\beta_-^j\right)\boldsymbol{\psi}_k^{j+1} \qquad j = 0, \ldots, N_\beta - 1, \quad k = 1, \ldots, N. \tag{2.41}$$

It is then straightforward to eliminate all of the intermediate ($j = 1, .., N_\beta - 1$) auxiliary variables, leaving

$$\boldsymbol{\psi}_k^{N_\beta} = \mathcal{F}(\alpha_k)\boldsymbol{\psi}_k \qquad k = 1, \ldots, N \tag{2.42}$$

with

$$\mathcal{F}(\alpha) = \prod_{j=0}^{N_\beta - 1} \frac{\alpha - \beta_+^j}{\alpha - \beta_-^j}. \tag{2.43}$$

We now re-assemble equation (2.42) into a single matrix equation for all $k$:

$$\begin{Bmatrix} \boldsymbol{\psi}_+^{N_\beta} \\ \boldsymbol{\psi}_-^{N_\beta} \end{Bmatrix} = \begin{bmatrix} \boldsymbol{F}_{++} & \boldsymbol{0} \\ \boldsymbol{0} & \boldsymbol{F}_{--} \end{bmatrix} \begin{Bmatrix} \boldsymbol{\psi}_+ \\ \boldsymbol{\psi}_- \end{Bmatrix}, \tag{2.44}$$

where $\boldsymbol{F}_{++}$ and $\boldsymbol{F}_{--}$ are diagonal matrices whose entries are the values of $\mathcal{F}(\alpha)$ associated with each rightgoing and leftgoing eigenvalue, respectively.

Next, we apply the termination condition given by equation (2.39c). To do so, we write the left-hand-side of equation (2.44) in terms of $\hat{\boldsymbol{\phi}}^{N_\beta}$:

$$\begin{bmatrix} \boldsymbol{U}_{++} & \boldsymbol{U}_{+-} \\ \boldsymbol{U}_{-+} & \boldsymbol{U}_{--} \end{bmatrix} \begin{Bmatrix} \hat{\boldsymbol{\phi}}_+^{N_\beta} \\ \hat{\boldsymbol{\phi}}_-^{N_\beta} \end{Bmatrix} = \begin{bmatrix} \boldsymbol{F}_{++} & \boldsymbol{0} \\ \boldsymbol{0} & \boldsymbol{F}_{--} \end{bmatrix} \begin{Bmatrix} \boldsymbol{\psi}_+ \\ \boldsymbol{\psi}_- \end{Bmatrix}. \tag{2.45}$$

Applying equation (2.39c) and eliminating $\hat{\boldsymbol{\phi}}_+^{N_\beta}$ leaves

$$\boldsymbol{\psi}_- = \boldsymbol{R}\boldsymbol{\psi}_+, \tag{2.46}$$

with

$$\boldsymbol{R} = \boldsymbol{F}_{--}^{-1}\boldsymbol{W}\boldsymbol{F}_{++}, \tag{2.47}$$

and

$$\boldsymbol{W} = \boldsymbol{U}_{-+}\boldsymbol{U}_{++}^{-1}. \tag{2.48}$$

The rectangular matrix $\boldsymbol{R}$ is analogous to a matrix of reflection coefficients. Each entry of $\boldsymbol{R}$ takes the form

$$\boldsymbol{r}_{mn} = \frac{\mathcal{F}(\alpha_{+,n})}{\mathcal{F}(\alpha_{-,m})}\boldsymbol{w}_{mn}, \tag{2.49}$$

where $\alpha_{+,n}$ is the $n^{\text{th}}$ rightgoing eigenvalue, $\alpha_{-,m}$ is the $m^{\text{th}}$ leftgoing eigenvalue, and $\boldsymbol{w}_{mn}$ is the $(m,n)$ entry of the weighting matrix $\boldsymbol{W}$, which does not depend on the recursion parameters.

To achieve convergence to the exact one-way equation, every $\boldsymbol{r}_{mn}$ must converge toward zero as the order of the approximation increases. Since the weights are fixed, the recursion parameters must

be chosen such that $\mathcal{F}(\alpha_{+,n})/\mathcal{F}(\alpha_{-,m})$ goes to zero for all $m, n$. This is accomplished by forcing $\mathcal{F}(\alpha_{+,n})$ to zero and $\mathcal{F}(\alpha_{-,m})$ to infinity.

The following geometric interpretation of $\mathcal{F}$ is helpful for choosing parameters that accomplish these objectives. Note that $\mathcal{F}$ is composed of a product of factors

$$\mathcal{F}^j(\alpha) = \frac{\alpha - \beta_+^j}{\alpha - \beta_-^j}. \tag{2.50}$$

It is clear that the magnitude of each individual factor is less than one for regions of the complex $\alpha$ plane that are closer to $\beta_+^j$ than $\beta_-^j$ ($|\alpha - \beta_+^j| < |\alpha - \beta_-^j|$) and greater than one for regions that are closer to $\beta_-^j$ than $\beta_+^j$ ($|\alpha - \beta_+^j| > |\alpha - \beta_-^j|$). Therefore, $\mathcal{F}(\alpha_{+,n})$ is driven to zero by placing the $\beta_+^j$ parameters near the rightgoing eigenvalues in the complex plane, and $\mathcal{F}(\alpha_{-,m})$ is driven to infinity by placing the $\beta_-^j$ parameters near the leftgoing eigenvalues.

Suppose that, for a given system, there exists a pair of parameters $\{\beta_+^0, \beta_-^0\}$ for which $|\mathcal{F}^0| < 1$ for all rightgoing eigenvalues and $|\mathcal{F}^0| > 1$ for all leftgoing eigenvalues. Furthermore, define $\kappa$ as the maximum value of $|\mathcal{F}^0(\alpha_{+,n})|/|\mathcal{F}^0(\alpha_{-,m})|$ over all $m, n$. If this parameter pair is then repeated for all $j = 0, \ldots, N_\beta - 1$, the slowest converging entry of $\boldsymbol{R}$ will decrease like $\kappa^{N_\beta}$ as the order of the approximation is increased. Therefore, even for this very simple choice of parameters, the method exhibits spectral convergence. In practice, it is not always possible to find a single pair of recursion parameters for which this supposition holds. Even if such a pair exists, it is typically preferable to distribute the parameters over a range of locations using the above distance-based guidelines, since eigenvalues close to a single repeated parameter converge much more rapidly than those farther away.

The question arises whether it is always possible to find a set of recursion parameters, for some sufficiently high $N_\beta$, that makes every $\boldsymbol{r}_{mn}$ arbitrarily small. Assuming that $\alpha_{+,n} \neq \alpha_{-,m}$ for all $m, n$, the answer is, surprisingly, yes. Specifically, the minimal set that accomplishes this is $\left\{\beta_+^n = \alpha_{+,n},\ \beta_-^n \neq \alpha_{+,n} : n = 1, \ldots, N_+\right\}$ if $N_+ < N_-$ or $\left\{\beta_-^m = \alpha_{-,m},\ \beta_+^m \neq \alpha_{-,m} : m = 1, \ldots, N_-\right\}$ if $N_- < N_+$. This of course requires complete knowledge of the eigenvalues of the discretized sys-

tem, which is rarely possessed in practice. However, for systems that model physical phenomena, the locations of the rightgoing and leftgoing eigenvalues are physically meaningful and can often be estimated by studying simplified systems. This will be demonstrated for the Euler equations in 2.2.6. Furthermore, the spectra of discretized physical systems tend to be structured, such that groups of rightgoing eigenvalues often occupy different regions of the complex plane than groups of leftgoing eigenvalues. Again, this will often be the case for the Euler equations, even when linearized about nonuniform baseflows.

When eigenvalues cluster into groups, $\mathcal{F}$ can be driven to its desired limit for a large number of eigenvalues using a small number of parameters by taking advantage of the short distances between clustered eigenvalues and placing a parameter within the cluster. As will be shown in section 2.2.5, it is precisely the fact that good approximations can be obtained for $N_\beta << N$ that makes the approximate one-way equations cost-effective.

### 2.2.4 Extension to $x$-dependent systems

In the previous two subsections, we developed exact and approximate one-way equations under the assumption that $\boldsymbol{M}$ is homogeneous in $x$. In this subsection, we discuss the extension of these methods to $x$-dependent systems.

First, it is easy to verify that for $x$-dependent systems, the approximate parabolization given by equation (2.39) still converges to the exact parabolization given by equation (2.36) at every $x$. Therefore, we must only evaluate the exact method, and all conclusions will apply also to the approximate formulation.

Central to the concept of parabolization is the identification of rightgoing and leftgoing parts of the solution at each axial location. When $\boldsymbol{M}$ is $x$-dependent, equation (2.21) no longer admits simple modal solutions, so Briggs' criterion no longer strictly applies. However, the theory of well-posedness of variable coefficient hyperbolic systems (Kreiss 1970) provides a means by which to distinguish, locally at each $x$, parts of the solution that are rightgoing and leftgoing. Simply put, the variable coefficient extension of well-posedness theory states that constant coefficient analysis of

the frozen coefficient system at a given $x$ provides the correct (that is, well-posed) division of the solution into rightgoing and leftgoing components. Therefore, the one-way equations derived in the previous two sections will still retain and eliminate the correct parts of the operator at each axial station for $x$-dependent systems, and the equations therefore remain well-posed.

The fundamental difference between the homogeneous and $x$-dependent cases is that in the later, the rightgoing and leftgoing variables no longer evolve *independently*. Except in rare cases, the eigen-expansion $\hat{\boldsymbol{\phi}} = \boldsymbol{V}\boldsymbol{\psi}$ no longer diagonalizes equation (2.21) because $\frac{d\boldsymbol{V}}{dx} \neq \boldsymbol{0}$. As a result, every expansion coefficient $\boldsymbol{\psi}_k$ is potentially coupled with every other coefficient. This coupling is intrinsic to $x$-dependent equations and is deeply linked to important properties of their solutions. For example, this coupling allows the convective wavepacket solutions of the linearized Euler equations that were discussed in section 1.2.4 to excite acoustic waves that propagate in all directions.

The implication of this coupling for our one-way equation is that setting $\boldsymbol{\psi}_- = \boldsymbol{0}$ will cause $\boldsymbol{\psi}_+$ to evolve incorrectly as it propagates. Therefore, accurate one-way approximations can only be obtained when leftgoing waves have a *weak* influence on the evolution of the rightgoing waves. This is not a shortcoming of our particular parabolization method, but rather an inherent limitation on the class of problems for which a one-way solution strategy is sensible. An important situation in which the coupling is weak occurs when the system is *slowly-varying* in $x$. In this case, the slow variation of the system ensures the slow variation of $\boldsymbol{V}$, which in turn implies that the eigen-expansion nearly diagonalizes $\boldsymbol{M}$. A close examination of the meaning of "nearly diagonalizes" reveals that this is akin to the usual short-wavelength condition that is frequently invoked when extending local theory to spatially-varying equations.

To reiterate, the one-way equations are well-posed for all hyperbolic systems, but physical accuracy is guaranteed only for those that are sufficiently slowly-varying in $x$.

### 2.2.5 Computational complexity

The approximate one-way equation given by equation (2.39) defines a set of differential-algebraic equations of the form

$$\frac{d\hat{\boldsymbol{\phi}}_+}{dx} = \boldsymbol{G}_{++}\hat{\boldsymbol{\phi}}_+ + \boldsymbol{G}_{+*}\hat{\boldsymbol{\phi}}_*, \tag{2.51a}$$

$$\mathbf{0} = \boldsymbol{G}_{*+}\hat{\boldsymbol{\phi}}_+ + \boldsymbol{G}_{**}\hat{\boldsymbol{\phi}}_*. \tag{2.51b}$$

Here, $\hat{\boldsymbol{\phi}}_* \in \mathbb{C}^{N_*}$ contains $\hat{\boldsymbol{\phi}}_-$ and all of the auxiliary variables, and $N_* = (NN_\beta + N_-) \propto N_y N_\beta$.

Satisfying the algebraic constraint represented by equation (2.51b) requires the solution of a matrix system with leading dimension $\mathcal{O}(N_y N_\beta)$. For efficiency, it is important for the system to be sparse, which, in turn, requires the use of sparse discretization schemes for the transverse dimensions. When this requirement is observed, the banded structure of the system results in a predicted operation count that scales like $N_y N_\beta^2$. Modern sparse solvers can often exploit additional structure within the system not accounted for in this simple cost estimate, and in practice we observe scaling like $N_y N_\beta^p$ with $1 < p < 2$. Frequently, $p \approx 1.5$.

The eigen-solution required by the exact parabolization method scales like $N_y^3$. The cost savings of the approximate method stems from the fact that $N_\beta \ll N_y$ and therefore $N_\beta^p \ll N_y^2$. Because of the impracticality of the exact parabolization method, from here on out we will refer to the approximate formulation as *the* one-way equations. Direct time domain and frequency domain solutions of the original hyperbolic system scale like $N_y N_t$ and $N_y^2$, respectively, per axial station. In time domain solvers, $N_t$ is the number of time steps required to obtain a stationary solution. Again, the benefit of the one-way equations is that $N_\beta^p \ll N_t$. Finally, PSE usually scales like $N_y N_{it}$, where $N_{it}$ is the number of iterations required to satisfy a nonlinear constraint that is part of the PSE formulation. PSE is typically cheaper than the one-way equations since in most cases $N_{it} < N_\beta^p$.

It's likely that employing an iterative approach for satisfying equation (2.51b) could lead to $N_y N_\beta$ scaling of the one-way method, thus bringing its cost in line with that of PSE. This is an

enticing goal in the ongoing development of the method.

### 2.2.6 Parameter selection for the Euler equations

In this section, our one-way methodology is applied to the linearized Euler equations. The primary task is to determine robust recursion parameters that can be used for a range of problems. To achieve this, we first use analytical eigenvalues for a uniform flow to predict the approximate locations of the eigenvalues of the semi-discretized equations for nonuniform flows. Using these estimates, strategies developed by Hagstrom and colleagues (Hagstrom & Warburton 2004, 2009, Hagstrom et al. 2007, 2012) for choosing parameters for nonreflecting boundary conditions can be adapted to select recursion parameters that result in accurate and convergent one-way equations for many flows. The development outlined here for the Euler equations can be used as a guide for identifying appropriate recursion parameters when applying the method to other hyperbolic systems of equations.

The linearized Euler equations in three-dimensional Cartesian coordinates can be written in the form of equation (2.15) with $d = 3$,

$$A = \begin{bmatrix} \bar{u}_x & -\bar{\nu} & 0 & 0 & 0 \\ 0 & \bar{u}_x & 0 & 0 & \bar{\nu} \\ 0 & 0 & \bar{u}_x & 0 & 0 \\ 0 & 0 & 0 & \bar{u}_x & 0 \\ 0 & \gamma\bar{p} & 0 & 0 & \bar{u}_x \end{bmatrix}, \qquad B_1 = \begin{bmatrix} \bar{u}_{y_1} & 0 & -\bar{\nu} & 0 & 0 \\ 0 & \bar{u}_{y_1} & 0 & 0 & 0 \\ 0 & 0 & \bar{u}_{y_1} & 0 & \bar{\nu} \\ 0 & 0 & 0 & \bar{u}_{y_1} & 0 \\ 0 & 0 & \gamma\bar{p} & 0 & \bar{u}_{y_1} \end{bmatrix},$$

$$B_2 = \begin{bmatrix} \bar{u}_{y_2} & 0 & 0 & -\bar{\nu} & 0 \\ 0 & \bar{u}_{y_2} & 0 & 0 & 0 \\ 0 & 0 & \bar{u}_{y_2} & 0 & 0 \\ 0 & 0 & 0 & \bar{u}_{y_2} & \bar{\nu} \\ 0 & 0 & 0 & \gamma\bar{p} & \bar{u}_{y_2} \end{bmatrix}, \qquad C = \begin{bmatrix} -\nabla\cdot\bar{u} & \frac{\partial\bar{\nu}}{\partial x} & \frac{\partial\bar{\nu}}{\partial y_1} & \frac{\partial\bar{\nu}}{\partial y_2} & 0 \\ \frac{\partial\bar{p}}{\partial x} & \frac{\partial\bar{u}_x}{\partial x} & \frac{\partial\bar{u}_x}{\partial y_1} & \frac{\partial\bar{u}_x}{\partial y_2} & 0 \\ \frac{\partial\bar{p}}{\partial y_1} & \frac{\partial\bar{u}_{y_1}}{\partial x} & \frac{\partial\bar{u}_{y_1}}{\partial y_1} & \frac{\partial\bar{u}_{y_1}}{\partial y_2} & 0 \\ \frac{\partial\bar{p}}{\partial y_2} & \frac{\partial\bar{u}_{y_2}}{\partial x} & \frac{\partial\bar{u}_{y_2}}{\partial y_1} & \frac{\partial\bar{u}_{y_2}}{\partial y_2} & 0 \\ 0 & \frac{\partial\bar{p}}{\partial x} & \frac{\partial\bar{p}}{\partial y_1} & \frac{\partial\bar{p}}{\partial y_2} & \gamma\nabla\cdot\bar{u} \end{bmatrix},$$

and $q = \{\nu, u_x, u_{y_1}, u_{y_2}, p\}^T$. We have chosen as independent variables specific volume $\nu$, velocity $u = \{u_x, u_{y_1}, u_{y_2}\}^T$, and pressure $p$. The equations are linearized about a baseflow $\bar{q} = \{\bar{\nu}, \bar{u}_x, \bar{u}_{y_1}, \bar{u}_{y_2}, \bar{p}\}^T$, and all variables have been appropriately non-dimensionalized by an ambient sound speed and density and a problem dependent length-scale. The fluid is approximated as a perfect gas with specific heat ratio $\gamma$.

The eigenvalues and diagonalizing transformation of $A$ are

$$\tilde{A} = \begin{bmatrix} \bar{u}_x & 0 & 0 & 0 & 0 \\ 0 & \bar{u}_x & 0 & 0 & 0 \\ 0 & 0 & \bar{u}_x & 0 & 0 \\ 0 & 0 & 0 & \bar{u}_x + \bar{c} & 0 \\ 0 & 0 & 0 & 0 & \bar{u}_x - \bar{c} \end{bmatrix}, \qquad T = \begin{bmatrix} 1 & 0 & 0 & 0 & (\bar{\nu}/\bar{c})^2 \\ 0 & 0 & 1 & 0 & 0 \\ 0 & 0 & 0 & 1 & 0 \\ 0 & 1 & 0 & 0 & \bar{\nu}/\bar{c} \\ 0 & 1 & 0 & 0 & -\bar{\nu}/\bar{c} \end{bmatrix},$$

where $\bar{c} = (\gamma \bar{p} \bar{\nu})^{1/2}$ is the speed of sound. The semi-discretized operators $\tilde{\boldsymbol{A}}$ and $\boldsymbol{T}$ are found by sampling $\tilde{A}$ and $T$, respectively, at the discretization points.

The critical step in applying our one-way methodology to any system of equations is determining appropriate recursion parameters. As discussed in section 2.2.3, this requires knowledge of the eigenvalues of the semi-discretized operator $\boldsymbol{M}$ – specifically their location in the complex plane and their direction (rightgoing or leftgoing). For many baseflows, the eigenvalues of the semi-discretized equations form predictable groups that can be approximated and classified using the eigenvalues supported by a uniform flow. These uniform flow eigenvalues can be computed analytically, and therefore provide a means by which to predict the locations and directions of the eigenvalues for nonuniform baseflows. These estimates, in turn, can be used to define recursion parameters that result in convergent one-way approximations of the nonuniform equations.

We now derive the spatial eigenvalues of the Euler equations linearized about a uniform flow. For a uniform baseflow, $C = 0$ and the entries of the remaining three matrix coefficients are constants. Because of this, the transverse directions can be Fourier transformed rather than discretized. Then

equation (2.15) reduces to

$$\frac{\partial q^\dagger}{\partial t} + A\frac{\partial q^\dagger}{\partial x} + ik_1 B_1 q^\dagger + ik_2 B_2 q^\dagger = 0, \tag{2.53}$$

where $q^\dagger$ is the Fourier transform of $q$ and $k_{1,2}$ are the Fourier duals of $y_{1,2}$. Proceeding as in section 2.2.1, equation (2.53) is then written in terms of its characteristic variables $\phi^\dagger = Tq^\dagger$, Laplace transformed in time, and solved for the axial derivative term, finally resulting in an equation of the form

$$\frac{d\hat{\phi}^\dagger}{dx} = M^\dagger \hat{\phi}^\dagger \tag{2.54}$$

with

$$M^\dagger = ikTA^{-1}\left(I - z_1 B_1 - z_2 B_2\right)T^{-1}. \tag{2.55}$$

Here, $\hat{\phi}^\dagger$ is the Laplace transform of $\phi^\dagger$, $k = (\omega + i\eta)/\bar{c}$ is a scaled Laplace variable, and $z_{1,2} = k_{1,2}/k$ are scaled transverse wavenumbers.

The eigenvalues of $M^\dagger$ are

$$i\alpha_c = \frac{ik}{\bar{M}_x}, \qquad i\alpha_{a_1}(z) = ik\,\frac{-\bar{M}_x + \mu(z)}{1-\bar{M}_x^2}, \qquad i\alpha_{a_2}(z) = ik\,\frac{-\bar{M}_x - \mu(z)}{1-\bar{M}_x^2}, \tag{2.56}$$

where $\bar{M}_x = \bar{u}_x/\bar{c}$ is the local Mach number, $z = \left(z_1^2 + z_2^2\right)^{1/2}$ is a composite wavenumber, and the function $\mu(z)$ is given by

$$\mu(z) = \sqrt{1 - (1-\bar{M}_x^2)z^2}. \tag{2.57}$$

The discrete eigenvalue $i\alpha_c$ has multiplicity three and describes the convection of entropy and vorticity, while the remaining two eigenvalues are continuous branches and describe both propagating and evanescent acoustic waves. These are the three dimensional analogue of the two dimensional

uniform flow eigenvalues discussed in section 2.1.2.

Each of these eigenvalues can be identified as either rightgoing or leftgoing for different values of the Mach number using Briggs' criterion. Each eigenvalue also has a singular point at a particular Mach number corresponding to a singular point of $A$. This is discussed further in Appendix B, but for the purpose of parameter selection these infinite eigenvalues can be ignored. The results are summarized as a function of the Mach number in Table 2.1, in which a $(+)$ indicates that an eigenvalue is rightgoing, a $(-)$ indicates that an eigenvalue is leftgoing, and a zero indicates a singular point. With these directions determined, we set $\eta = 0$ from here on out.

Table 2.1: Classification of the eigenvalues of the uniform Euler equations: rightgoing $(+)$, leftgoing $(-)$, or singular $(0)$.

| Eigenvalue | $\bar{M}_x < -1$ | $\bar{M}_x = -1$ | $-1 < \bar{M}_x < 0$ | $\bar{M}_x = 0$ | $0 < \bar{M}_x < 1$ | $\bar{M}_x = 1$ | $\bar{M}_x > 1$ |
|---|---|---|---|---|---|---|---|
| $\alpha_c$ | $-$ | $-$ | $-$ | $0$ | $+$ | $+$ | $+$ |
| $\alpha_{a_1}$ | $-$ | $0$ | $+$ | $+$ | $+$ | $+$ | $+$ |
| $\alpha_{a_2}$ | $-$ | $-$ | $-$ | $-$ | $-$ | $0$ | $+$ |

The eigenvalues of semi-discretized nonuniform Euler equations can often be sorted into groups associated with these three uniform flow eigenvalues. First, nonuniform Euler equations typically support convective modes that travel with phase speeds ranging from the slowest to fastest axial velocities within the flow. The location and direction of these eigenvalues are given by evaluating $\alpha_c$ with $\bar{M}_x$ varied over this range of velocities.

Second, nonuniform Euler equations usually support branches of acoustic modes that are well approximated by $\alpha_{a_1}$ and $\alpha_{a_2}$ with $\bar{M}_x$ set to its asymptotic value as $|y|$ becomes large. If multiple asymptotic values of $\bar{M}_x$ exist, multiple branches of acoustic eigenvalues will exist that can be approximated by evaluating $\alpha_{a_1}$ and $\alpha_{a_2}$ separately at each asymptotic value. These uniform flow acoustic eigenvalues are continuous branches while the eigenvalues of the semi-discretized nonuniform equations are necessarily discrete. One consequence of this is that the continuous eigenvalues need only be considered up to the maximum wavenumber $z_{max}$ that is supported by the transverse grid, since no eigenvalues of the semi-discretized equations exist beyond this limit.

These eigenvalue estimates can also be used when the Euler equations are written in different

coordinate systems. The uniform flow equations in two-dimensional Cartesian coordinates admit the same analytical eigenvalues, but the convective eigenvalue has multiplicity two instead of three. When written in cylindrical coordinates, some of the matrix coefficients depend on the radial coordinate, so strictly speaking, analytical eigenvalues cannot be derived using spatial Fourier transforms. In spite of this, we have found that the above eigenvalues still provide a good representation of the discretized eigenvalues for both uniform and nonuniform baseflows.

These predictions for the locations and directions of the eigenvalues of $\boldsymbol{M}$ can now be used to choose appropriate recursion parameters. As established in section 2.2.3, the $\beta_+^j$ parameters must be placed near the rightgoing eigenvalues so that $\mathcal{F}$ is small for every rightgoing eigenvalue, while the $\beta_-^j$ parameters must be placed near the leftgoing eigenvalues so that $\mathcal{F}$ is large for every leftgoing eigenvalue. In other words, the $\beta_+^j$ and $\beta_-^j$ parameters should be distributed over the predicted locations of the rightgoing and leftgoing eigenvalues, respectively.

As an example, we expound this procedure for the commonly encountered case where $0 < \bar{M}_x < 1$ everywhere in the flow. Then $\alpha_c$ and $\alpha_{a_1}$ are rightgoing while $\alpha_{a_2}$ is leftgoing. A complete set of recursion parameters is constructed by defining several subsets related to different parts of the predicted spectrum. Strategies for choosing these subsets are described in the following paragraphs, and their precise definitions are given in Table 2.2.

First, a set $\beta_\pm^c$ with $N_c$ parameter pairs is defined with the goal of making $\mathcal{F}$ small for the convective eigenvalues. The $\beta_+^j$ parameters are evenly distributed over the range of predicted values of $\alpha_c$. The corresponding $\beta_-^j$ parameters should be placed far away from the convective eigenvalues so that the magnitude of the $\mathcal{F}^j$ factors for these parameters are as small as possible in the vicinity of the convective eigenvalues. However, it is also desirable for these $\mathcal{F}^j$ factors to be small at $\alpha_{a_1}$ and large at $\alpha_{a_2}$. A good compromise between these two competing objectives is obtained by rotating the $\beta_+^c$ parameters by -90 degrees around the asymptotic value of $\bar{M}_x$ that is used to predict the acoustic parameters. Then, $|\mathcal{F}^j| \leq 1$ for all values of $\alpha_{a_1}$ and $|\mathcal{F}^j| \geq 1$ for all values of $\alpha_{a_2}$.

In choosing parameters to target the predicted acoustic eigenvalues, we exploit the rotational symmetry between $\alpha_{a_1}$ and $\alpha_{a_2}$ (about $k\frac{-\bar{M}_x}{1-\bar{M}_x^2}$ for each asymptotic value of $\bar{M}_x$). This allows

parameter pairs to be chosen that simultaneously make the corresponding $\mathcal{F}^j$ factors small for the rightgoing eigenvalues and large for the leftgoing eigenvalues. Specifically, the $\beta_+^j$ parameters are distributed along $\alpha_{a_1}$ and the $\beta_-^j$ parameters are distributed along $\alpha_{a_2}$. The most straightforward approach to distributing the parameters is to choose a set of values of $z$ or $\mu(z)$ and define the pairs by evaluating both acoustic eigenvalues at each value. This choice guarantees the desired behavior of the $\mathcal{F}^j$ factors. However, Hagstrom et al. (2012) showed that the uniform flow reflection coefficient (which is the analytical analogous to equation (2.46)) can be made zero at twice as many locations by offsetting the points at which $\alpha_{a_1}$ and $\alpha_{a_2}$ are evaluated.

Note that $\alpha_{a_1}$ and $\alpha_{a_2}$ are purely real up to a critical value of $z$, at which point they become purely imaginary. The real parts of the branches correspond to propagating acoustic waves, while the imaginary parts represent evanescent acoustic waves. We distribute the parameter pairs separately for these two sections of the branches. For the propagating modes, the angle of propagation is $\theta = \cos^{-1}(\mu(z))$. To choose a set $\beta_\pm^p$ with $N_p$ offset parameter pairs, take $2N_p + 1$ equally spaced angles on the closed interval $[0, \pi/2]$ and discard the final angle $\theta = \pi/2$. Then, starting with $\theta = 0$, use every-other angle to define a $\beta_+^j$ and $\beta_-^j$ parameter. To choose a set $\beta_\pm^e$ with $N_e$ parameters for the evanescent section of the acoustic branches, define $2N_e + 1$ equally spaced points on the closed interval $[0, \mu(z_{max})]$ and discard the point $\mu = 0$. Then, starting with the next value, use every-other point to define a $\beta_+^j$ and $\beta_-^j$ parameter.

The reason for omitting the values $\theta = \pi/2$ and $\mu(z) = 0$ (which are the same point in the complex plane) in both acoustic parameter sets is that they represent energy transfer that is tangent to the parabolization axis, which can never be captured by one-way spatial marching. Furthermore, the rightgoing branch $\alpha_{a_1}$ and the leftgoing branch $\alpha_{a_2}$ intersect at this point, and it is clearly impossible to make $\mathcal{F}$ both large and small at the same time. This is of no practical concern because the equivalent branches that occur in discretized equations do not intersect in this manner due to the incorporation of nonreflecting transverse boundary conditions (see for example the eigenvalues in Figure 2.7).

Rather than defining the acoustic parameters using equally spaced angles (propagating) and

points along $\mu$ (evanescent), the parameters can instead be chosen by formally minimizing $\mathcal{F}(\alpha_{a_1})/\mathcal{F}(\alpha_{a_2})$ with respect to some norm. Following Hagstrom & Warburton (2009), we have carried out this calculation using a weighted minimax norm, but found very little improvement over equal spacing. The optimized parameters offered moderate improvements at high propagation angles, but at the cost of a degradation of evanescent and low angles waves. In practice, we therefore use the simple approach based on equal spacing.

The final set of recursion parameters is defined by taking the union of all of the subsets related to the different parts of the predicted spectrum. Typically, we use roughly the same number of parameters for each subset.

Table 2.2: Recursion parameter sets that target the three predicted groups of eigenvalues for $0 < \bar{M}_x < 1$.

| Type | Spacing | $\beta_+^j/k$ | $\beta_-^j/k$ |
|---|---|---|---|
| **Convective** | $b^h = \frac{1}{M_{max}} + \left(\frac{1}{M_{min}} - \frac{1}{M_{max}}\right)\frac{h}{N_c-1}$ | $b^j$ | $-ib^j + (1+i)\dfrac{-\bar{M}_x}{1-\bar{M}_x^2}$ |
| $\beta_\pm^c = \{\beta_\pm^j : j = 0, \ldots, N_c - 1\}$ | $h = 0, \ldots, N_c - 1$ | | |
| **Acoustic, propagating** | $\theta^h = \frac{\pi}{2}\frac{h}{2N_p}$ | $\dfrac{-\bar{M}_x + \cos\theta^{2j}}{1-\bar{M}_x^2}$ | $\dfrac{-\bar{M}_x - \cos\theta^{2j+1}}{1-\bar{M}_x^2}$ |
| $\beta_\pm^p = \{\beta_\pm^j : j = 0, \ldots, N_p - 1\}$ | $h = 0, \ldots, 2N_p - 1$ | | |
| **Acoustic, evanescent** | $\mu^h = \mu_{max}\frac{h}{2N_e}$ | $\dfrac{-\bar{M}_x + \mu^{2j}}{1-\bar{M}_x^2}$ | $\dfrac{-\bar{M}_x - \mu^{2j+1}}{1-\bar{M}_x^2}$ |
| $\beta_\pm^e = \{\beta_\pm^j : j = 0, \ldots, N_e - 1\}$ | $h = 0, \ldots, 2N_e - 1$ | | |

The effectiveness of these parameters for a given baseflow can be evaluated by computing the local eigenvalues of the original and one-way operators at a few $x$ locations. This is carried out, for example, in section 2.2.7.1 for a quiescent baseflow and in section 2.2.8.1 for two characteristic jet profiles. If necessary, the eigenvalues of the original operator can then be used to guide modifications to the parameter sets based on the rule of placing the plus and minus parameters near the rightgoing and leftgoing eigenvalues, respectively. In particular, it's important to ensure that the parameters are chosen so that all of the one-way eigenvalues are stable (i.e., have positive imaginary part), except for those associated with the convective instabilities of the original operator. If this is not accomplished, the one-way integration, although well-posed, can become numerically unstable.

### 2.2.7 Validation results

In this section, we use the one-way Euler equations to solve three problems. First, a simple case involving the propagation of monopole acoustic waves in a quiescent fluid is used to demonstrate the convergence of the one-way equations. Second, the scattering of acoustic waves by a vortex is calculated using the one-way equations and compared to published direct-numerical-simulation results. Third, convectively unstable wavepackets in a compressible two-dimentional mixing layer are modeled using the one-way equations and compared to direct frequency domain and PSE solutions of the same equations.

For all simulations, the equations are discretized in the transverse direction using fourth-order central finite differences with summation-by-parts boundary closure (Mattsson & Nordstrm 2004). Far-field radiation boundary conditions are enforced at free transverse boundaries using a super-grid damping layer (Appelo & Colonius 2009) truncated by Thompson characteristic conditions (Thompson 1987). The one-way Euler equations are integrated in $x$ using a third-order, L-stable diagonally-implicit Runge-Kutta scheme (Hairer & Wanner 1971). Recursion parameters are selected using the strategies described in the previous section.

#### 2.2.7.1 Monopole acoustic waves in a quiescent fluid

In this problem, a monopole disturbance is placed just upstream of the computational domain in a quiescent fluid. The monopole generates an acoustic field for which an analytical solution exists. Since the system is $x$-independent and the solution is comprised exclusively of downstream propagating waves, this set-up allows the convergence of the one-way equation to be verified.

The computational domain extends six wavelengths in both $x$ and $y$ and is discretized using 300 equally spaced points in each direction. Along the inlet of the domain, the exact monopole solution is supplied as an incoming fluctuation which is then propagated through the domain by integrating the one-way Euler equations. The calculation is performed using different orders of the

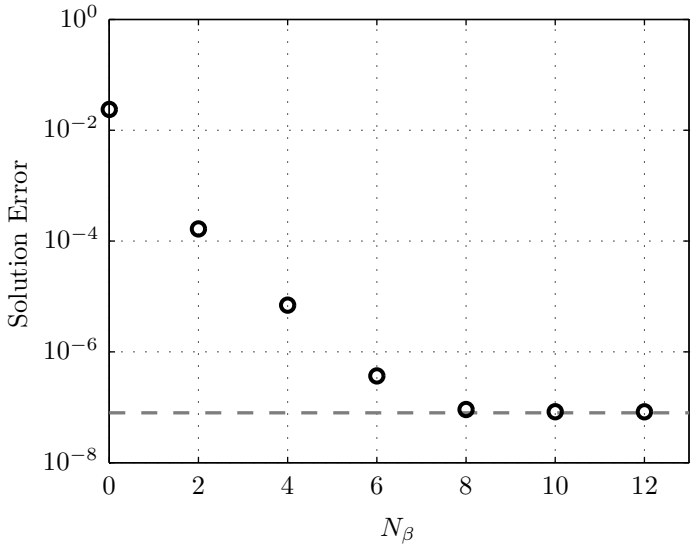


Figure 2.6: Solution error (defined in equation (2.58)) for the monopole problem for the approximate (O) and exact (– – –) one-way Euler equations.

approximation and also using the exact one-way equation. The solution error is defined as

$$\frac{1}{\mathcal{A}} \int_{\mathcal{A}} \left| \frac{p_{owe} - p_{exact}}{p_{max}} \right|^2 d\mathcal{A}, \tag{2.58}$$

where $p_{owe}$ is the pressure computed by the one-way Euler equations, $p_{exact}$ is the exact analytical pressure, and $p_{max}$ is the maximum value of the exact pressure in the domain. The integration is over the area $\mathcal{A}$ of the physical domain, not including the far-field damping layers.

The solution error results are plotted in Figure 2.6. The convergence of the one-way solution over $0 < N_\beta < 8$ is spectral. For $N_\beta > 8$, the error plateaus at a level equal to the error of the exact one-way solution. Recall that the one-way Euler eigenvalues converge toward the eigenvalues of the *discretized* equations; the properties of the underlying discretization are unaltered by the parabolization method. Therefore, the convergence plateau indicates that the parabolization error has become smaller than other numerical errors, such as those related to boundary conditions and finite difference approximation. By the time this occurs for the discretization used here, the error in the one-way solution has dropped by five orders of magnitude.

A useful way to visualize the convergence of the method is to compare the eigenvalues of the

one-way operator to those of the full operator $\boldsymbol{M}$. As the one-way system converges, its eigenvalues should converge to the rightgoing eigenvalues of $\boldsymbol{M}$. For the problem under consideration, all of the eigenvalues of $\boldsymbol{M}$ correspond to either rightgoing or leftgoing acoustic waves; no convective eigenvalues exist because the fluid is quiescent.

Figure 2.7 compares the eigenvalues at several orders of the approximation. At $N_\beta = 0$, the upstream acoustic waves have been removed (since the equations are well-posed even at zero order), but the downstream eigenvalues are poorly represented. As $N_\beta$ is increased, all the eigenvalues of the one-way system converge toward the rightgoing eigenvalues of the full operator. The convergence is quantified in Figure 2.8 for four eigenvalues corresponding to acoustic radiation to approximately 20, 40, 60, and 80 degrees to the parabolization axis (based on a simple plane-wave estimate). As expected, the higher angle eigenvalue converges more slowly than the lower angle eigenvalues, but the steady spectral convergence for all four angles confirms the quality of the recursion parameters that were derived in the previous section. The specific values of $\beta_+^j$ and $\beta_-^j$ used are also shown graphically in Figure 2.7.

#### 2.2.7.2 Scattering of acoustic waves by a vortex

Here, we use the one-way Euler equations to calculate the scattering of a plane acoustic wave by a homentropic vortex. This problem was previously investigated using a one-way wave equation (Candel 1979) (which the author called a parabolic approximation) and direct numerical simulation (Colonius et al. 1994). We will compare our one-way Euler results to the later.

In our formulation, the Euler equations are linearized about a steady, homentropic vortex that exactly satisfies the two-dimensional nonlinear Euler equations. The tangential velocity about the center of the vortex is

$$\bar{u}_\theta = \frac{\Gamma}{2\pi r}\left(1 - \exp\left(-ar^2\right)\right), \tag{2.59}$$

where $a = 1.256431$ is a constant chosen such that the maximum velocity occurs at $r = 1$. We define this to be the core radius, and non-dimensionalize by this length scale. The radial velocity is zero

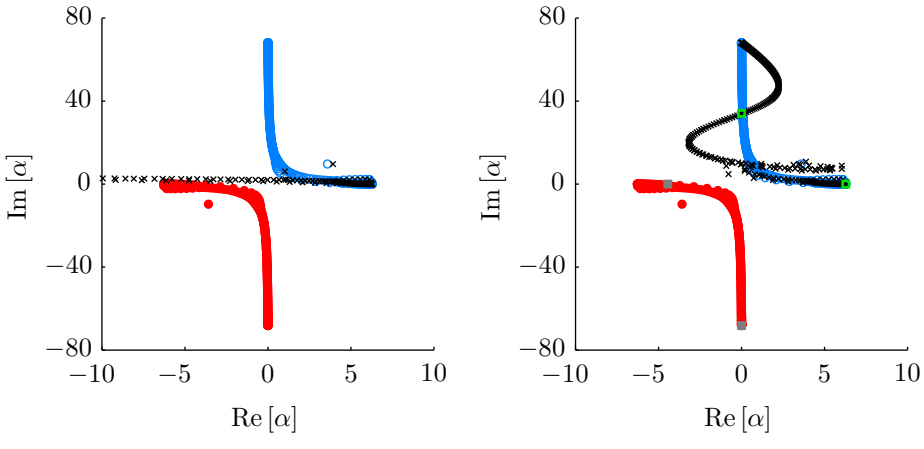


(a) $N_\beta = 0$ (b) $N_\beta = 2$

(c) $N_\beta = 4$ (d) $N_\beta = 6$

Figure 2.7: Comparison between the eigenvalues of the full and one-way Euler operators for the monopole problem at several orders of the approximation. The full equations support rightgoing ( ○ ) and leftgoing ( ● ) acoustic modes. The eigenvalues of the one-way equations ( × ) converge to the rightgoing modes. Also shown are the $\beta_+^j$ ( □ ) and $\beta_-^j$ ( ■ ) recursion parameters used for each order of the approximation.

and the pressure is given by

$$\bar{p} = \frac{1}{\gamma}\left(1 - \frac{(\gamma-1)\Gamma^2}{4\pi^2 r^2} f\left(ar^2\right)\right)^{\frac{\gamma}{\gamma-1}}, \tag{2.60}$$

where

$$f(w) = \frac{1}{2} - \exp(-w) + \frac{1}{2}\exp(-2w) + w\mathrm{Ei}(-2w) - w\mathrm{Ei}(-w) \tag{2.61}$$

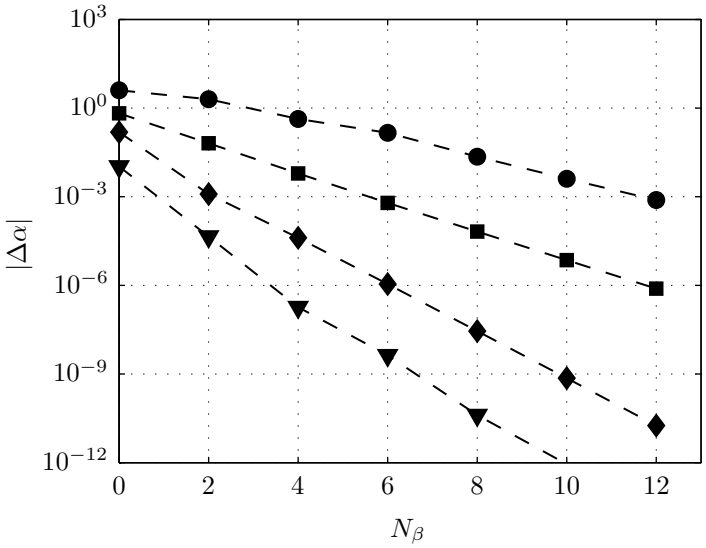


Figure 2.8: Distance between the exact and one-way Euler eigenvalue for the monopole problem corresponding to acoustic radiation to several angles relative to the axis of parabolization: 20°(▼); 40°(◆); 60°(■); 80°(●).

and Ei is the exponential integral function. The specific volume is related to the pressure by the homentropic relation

$$\bar{\nu} = (\gamma \bar{p})^{\frac{-1}{\gamma}} . \tag{2.62}$$

The maximum mean velocity induced by the vortex is

$$\bar{u}_\Gamma = \frac{\Gamma}{2\pi}. \tag{2.63}$$

We set $\bar{u}_\Gamma = 0.0625$ to match one of the DNS cases (Colonius et al. 1994).

The computational domain extends ten core radii in $x$ and $y$ from the center of the vortex, and the transverse $y$ direction is discretized using 250 equally spaced points. An incoming plane acoustic wave with a wavelength of four core radii is specified at the left-hand boundary, and advanced by integrating the one-way equations with a step size of $\Delta x = 0.08$, corresponding to 50 points per wavelength. The solution is well converged using $N_\beta = 12$.

The scattered wave field is defined as the difference between the wave distorted by the vortex and

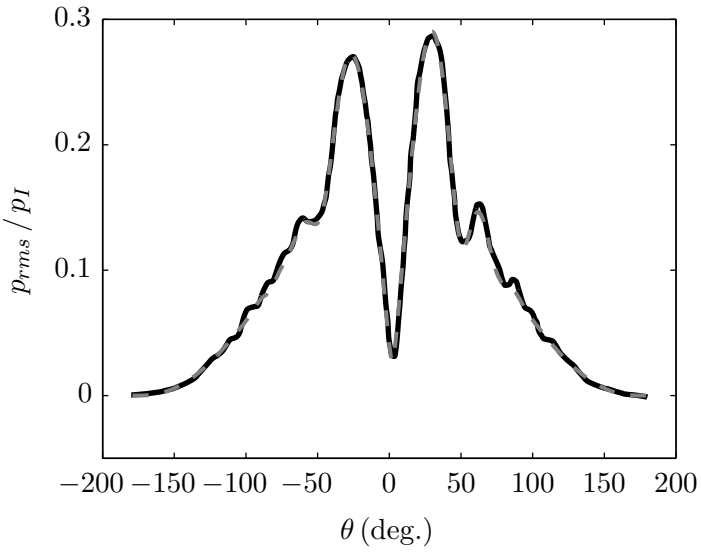


Figure 2.9: Root-mean-square pressure level of the scattered wave at $r = 10$ computed by: direct numerical simulation (———) and the one-way Euler equations (– – –).

an undistorted plane wave. In Figure 2.9, the root-mean-square of the scattered pressure at $r = 10$ is plotted as a function of angle, with $\theta = 0$ corresponding to the forward direction of the incident wave. The DNS results of Colonius et al. (1994) are also shown. The agreement between the two solutions is excellent. The discernible error is confined to high forward angles ($80 < \theta < 90$) and backward angles ($\theta > 90$) for which the one-way solution is expected to degrade. The reasonable accuracy even at these high angles reveals that the scattered wave field at these angles is dominated by refraction effects due to the slowly decaying vortex rather than direct scattering from the vortex core, since by definition the one-way solution does not contain leftgoing waves.

Analogous results can be obtained for stronger vortices up to $\bar{u}_\Gamma = 0.2$. Above this threshold, spurious eigenvalues appear in the spectrum of $\boldsymbol{M}$ that are not properly accounted for using our standard set of recursion parameters, leading to instability of the march. This highlights a limitation of our one-way methodology: recursion parameters must be specified that properly converge all of the eigenvalues of the discretized system, including those associated with both spurious nonphysical and unexpected physical dynamics. In this case, the offending eigenvalues are spurious – that is, a nonphysical artifact of the discretization. Such eigenvalues are by definition sensitive to details of the discretization, making them difficult to account for in the parameter selection process. It is

likely that more sophisticated approaches to selecting parameters could alleviate this issue, but it's also worth emphasizing that our simple approach has proven effective for the majority of problems so far encountered.

#### 2.2.7.3 Sound generation in a two-dimensional mixing-layer

In this problem, the generation and propagation of sound in a two-dimensional mixing layer is modeled using the one-way Euler equations. The baseflow is a second-order approximation of a self-similar solution of the incompressible boundary layer equations using Prandtl's eddy viscosity model Yule (1972). The Mach number of the fast and slow free-streams are 0.8 and 0.2, respectively. The shear layer thickness grows linearly, with the spread rate chosen to match experiments. The initial condition at the inlet is a pure Kelvin-Helmholtz eigenfunction computed at $x = 0$ under a locally-parallel assumption. We show results for the most unstable frequency near the inlet.

The solution is computed using PSE and the one-way Euler equations with $N_\beta = 15$. The one-way Euler solution is well-converged at this order. The accuracy of the one-way Euler solution is verified by comparing it to a direct frequency domain solution of the linearized Euler equations (LEE), which fully accounts for the non-parallel baseflow, and therefore can be considered the correct solution for this problem, up to numerical error. See Towne & Colonius (2013) for additional details.

Figure 2.10 shows the pressure field as computed by LEE, PSE, and OWE. First, consider the LEE solution. The near-field is dominated by a growing, then decaying wavepacket. The location where the wavepacket begins to decay acts as a sound source, creating acoustic radiation in all directions but especially in the downstream direction in the slow-stream ($y < 0$). Comparing the PSE and LEE solutions, two deficiencies are clearly discernible. First the PSE near-field wavepacket decays too rapidly. Second, the PSE solution contains almost no acoustic field at all. Again, this is due to the fact that the downstream acoustic modes in the PSE equations were heavily damped to allow a stable march.

The one-way Euler solution does not suffer from either of these problems. The near-field wavepacket in the one-way Euler solution is indistinguishable from the LEE wavepacket, and the

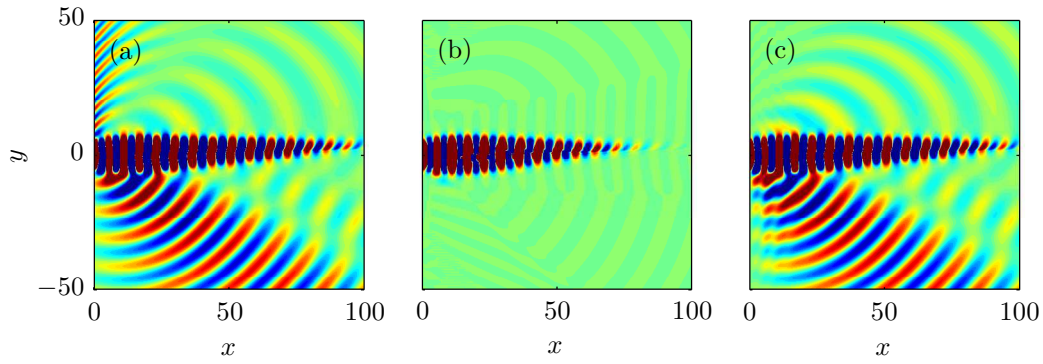


Figure 2.10: Pressure field generated by a wavepacket in a turbulent mixing layer computed using (a) direct solution of the linearized Euler equations, (b) PSE, (c) the one-way Euler equations.

downstream acoustic radiation is accurately captured. Two differences can be identified between the LEE and one-way Euler solutions. First, the one-way Euler solution does not capture the upstream acoustic radiation. This is inherent to any spatial marching technique. We note, however, that in this case, we believe that the upstream radiation in the LEE solution near the inlet may be an artifact of the inlet boundary conditions. Second, the downstream acoustic radiation to very high angles is somewhat inaccurate. This occurs because the eigenvalues associated with high angle acoustic radiation are typically difficult to converge. This error can be reduced by increasing the order of the recursions, but in many applications, including jet aeroacoustics, this high angle sound is unimportant compared to low angle sound, which is well captured using fairly lower order recursions.

Figure 2.11(a) shows the pressure field along $x = 50$ for each method. The exponential decay of the near-field pressure in all of the solutions is consistent with the asymptotic behavior of the Kelvin-Helmholtz mode. The LEE and one-way Euler pressure fields level off due to the presence of propagating acoustic waves that radiate to the far-field, and the agreement between these two solutions is excellent. In contrast, the damped remnants of acoustic radiation in the PSE solution is at least four orders of magnitude too small. Figure 2.11(b) shows the pressure field along a circular arc of radius 50 centered at the origin passing through the slow stream. It is clear that the primary error in the one-way Euler pressure field occurs at high angles, and that the solution at low and

intermediate angles is in close agreement with the LEE solution.

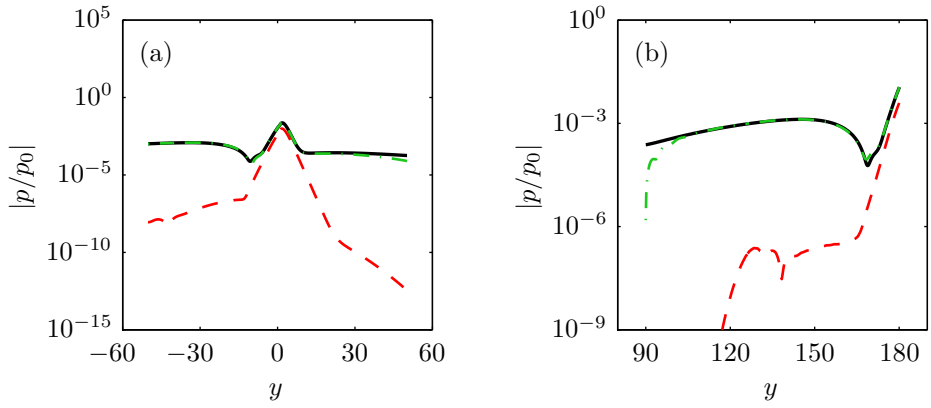


Figure 2.11: LEE (———), OWE (–·–·–), and PSE (– – –) pressure amplitude for the turbulent mixing layer (a) along the transverse slice $x = 50$, and (b) along a circular arc of radius 50 centered at the origin, sweeping through the slow stream. The angle is measured counter-clockwise from the negative $x$-axis.

Recall that the purpose of developing an improved spatial marching technique was to efficiently obtain accurate approximate solutions. We have seen here that the one-way Euler equations can produce accurate results. Table 2.3 shows the improved efficiency obtained over the direct LEE method for this mixing layer problem. Compared to LEE, the one-way Euler method offers a speed-up of 42 times and a factor of 242 times reduction in memory usage. We note that time domain implementations of the linearized Euler equations are less memory intensive than the frequency domain solver used here, but they are also slower, so the one-way Euler method would also offer attractive savings over a time domain LEE solver. The low CPU and RAM requirements of PSE are achieved at the expense of accuracy, as we have seen.

Table 2.3: Computational costs for the mixing layer problem.

| **Method** | **CPU Hours** | **RAM (GB)** |
|---|---|---|
| LEE | 136.0 | 194.1 |
| OWE | 3.2 | 0.8 |
| PSE | 0.02 | 0.08 |

### 2.2.8 Application to jets

In this section, we present results related to the application of the one-way Euler equations to jets. First, we demonstrate the ability of the one-way equations to accurately represent the typical mode-families that exist in supersonic and subsonic parallel jets, and in particular highlight the improved representation of important low-angle acoustic eigenvalues. Second, we calculate wavepackets in a Mach 0.9 turbulent jet using the one-way Euler equations and compare the results to those obtained using PSE and a direct time domain method. The computational details are the same as those reported at the beginning of section 2.2.7, and cylindrical coordinate pole conditions are implemented using the scheme of Mohseni & Colonius (2000).

#### 2.2.8.1 One-way spectra for typical jet profiles

Here, we apply the one-way Euler method to supersonic and subsonic parallel jets to demonstrate its ability to properly parabolize typical jet spectra. The base axial velocity is taken as

$$\bar{u}_x = \frac{\bar{u}_{jet} - \bar{u}_{co}}{2}\left(1 + \tanh\left(\frac{1}{4H}\left(\frac{1}{2r} - 2r\right)\right)\right) + \bar{u}_{co}, \tag{2.64}$$

where $\bar{u}_{jet}$ is the jet velocity, $\bar{u}_{co}$ is the co-flow velocity, and $H$ controls the momentum thickness of the shear-layer. With properly chosen $H$, this profile fits well with experimentally measured velocity profiles near the end of the potential core (Michalke 1971). In the following sections, we study Mach 1.5 and 0.9 jets with a Mach 0.1 co-flow. For both cases, we use the experimentally motivated thickness parameter $H = 0.16$ (Morris 1976). The pressure and specific volume are taken to be constant, and the radial and azimuthal velocities are zero.

The computational domain extends five jet diameters in the radial direction, and the radial coordinate is discretized using 350 points. A coordinate transformation is used to cluster grid-points in the shear-layer. Even though our discretization is stable in the inviscid limit, we use a Reynolds number of one million to further damp all spurious modes.

The spatial spectra of the Euler and Navier-Stokes equations for parallel supersonic and sub-

sonic jets have been extensively studied (Mattingly & Chang 1974, Morris 1976, Michalke 1984, Tam & Hu 1989). Within different flow regimes, several distinct families of modes have been identified and characterized. Although jet spectra have been shown to be sensitive to Mach number, temperature ratio, shear-layer thickness, and Reynolds number, the two simple jets considered here contain the main families of modes that exist for supersonic and subsonic jets over a wide range of operating conditions. The spatial spectra for the two jets at $St = 0.3$ and $m = 0$ are shown in Figure 2.12. Other frequencies and azimuthal modes within our range of interest have qualitatively similar spectra. We have taken the liberty to omit from these plots a number of stable spurious modes which inevitably arise due to the dispersive nature of the finite-difference discretization used to approximate radial derivatives. Spurious modes can be distinguished from physical ones by the tendency of their eigenvalues to change significantly as the grid is refined and the prevalence of point-to-point oscillations in their eigenfunctions. We have also omitted stable convective modes to reduce clutter.

For supersonic jets, six families of modes can be distinguished and are denoted by color in Figure 2.12(a). First, there is a single convectively unstable mode – the Kelvin-Helmholtz mode (O). Second, there are two continuous branches of vorticity and entropy modes that stably convect downstream at speeds ranging between the jet velocity and the co-flow velocity (omitted from plot). The third and fourth families are continuous branches of upstream (O) and downstream (O) free stream acoustic modes, which together radiate sound to all angles in the far-field. The fifth and sixth families are core pressure modes generated by resonant acoustic waves trapped within the potential core (O). These modes are discrete because of the confinement caused by the shear layer. One of these families has subsonic phase velocity and one has supersonic phase velocity, but they both have positive group velocity because of the supersonic flow in the core, and so they are both downstream families of modes (Tam & Hu 1989).

The spectrum of the Euler equations for the subsonic jet is shown in Figure 2.12(b). Seven families of modes can be identified. The first four families are unchanged from the supersonic case: the discrete Kelvin-Helmholtz mode (O), the continuous convective vorticity and entropy branches

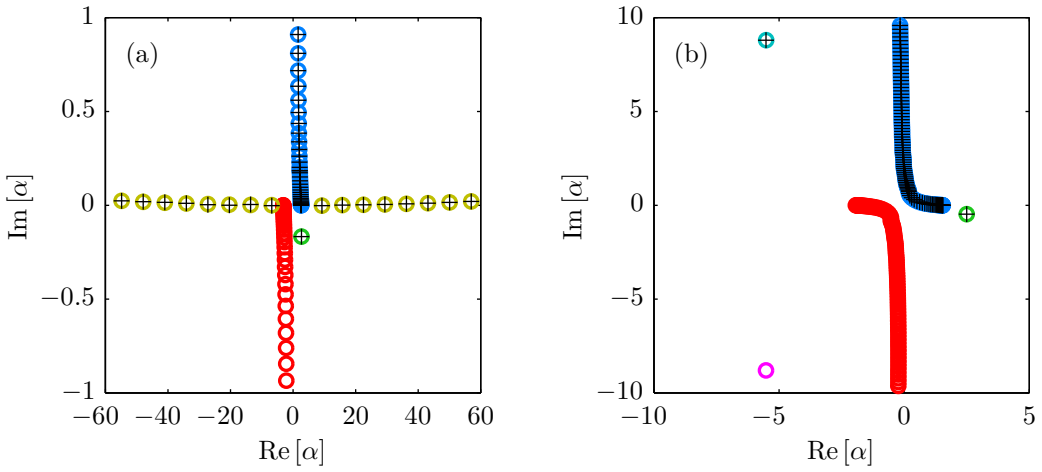


Figure 2.12: Spatial spectrum of the Euler equations for (a) supersonic jet, (b) subsonic jet. The following legend applies to both sub-figures: (O) Kevin-Helmholtz; (O) downstream free-stream acoustic; (O) upstream free-stream acoustic; (O) Tam's subsonic core modes; (O, O) high-subsonic jet core modes . The spectrum of the one-way Euler operator for each jet is given by the (+) symbols. In both cases, the upstream modes are properly removed, and all downstream modes are accurately represented.

(again omitted), and upstream (O) and downstream (O) free-stream acoustic branches. The remaining three mode families are related to acoustic waves in the jet core, but their characteristics are markedly different than the supersonic core modes. At low frequencies, the first of these mode families is neutrally upstream propagating (these modes are hidden amidst the upstream far-field modes in the figure), the second is a downstream traveling evanescent wave (O), and the third is an upstream traveling evanescent wave (O). For low subsonic Mach numbers, these categories hold at all frequencies (Tam & Hu 1989). On the other hand, for Mach numbers above approximately 0.8, these three families of modes exhibit behavior that was not observed by Tam & Hu (1989). Specifically, the two evanescent modes move together as the frequency increases and coalesce on the real $\alpha$ axis at some critical frequency. The two modes then move along the real axis in opposite directions until the mode moving toward the origin coalesces with the third neutral mode at a second critical frequency, at which point these two modes move off the real axis and become evanescent. This behavior has important physical ramifications, and is the subject of an ongoing investigation by Towne et al. (2016, in prep.).

The (+) symbols in Figure 2.12 are the eigenvalues of the one-way Euler operator for the supersonic and subsonic jets with $N_\beta = 18$ and $N_\beta = 14$, respectively. In both cases, all downstream modes are accurately represented and the upstream acoustic modes have been removed.

The behavior of the trapped acoustic modes in high-subsonic jets effects parabolization near the critical frequencies. Specifically, the coalescence of upstream and downstream modes at the critical frequencies corresponds to a neutral absolute instability (Huerre & Monkewitz 1990) and violates the condition that the rightgoing and leftgoing eigenvalues be distinct that is required for the existence of convergent recursions parameters, as described in section 2.2.3. Therefore, the one-way equations cannot be used in narrow frequency bands in the vicinity of these frequencies. We emphasize, however, that this should not be viewed as a flaw of our one-way methodology; rather, the existence of a neutral absolute instability makes spatial integration physically inappropriate.

For use as a jet noise model, it is especially important that the one-way Euler equations accurately represent the low-angle free-stream acoustic modes. Figure 2.13 concentrates on these low-angle acoustic modes and the Kelvin-Helmholtz mode and compares their one-way Euler and PSE representations, the latter of which were defined in section 2.1.4.

Recall that for PSE, the distortion of modes farther away from the Kelvin-Helmholtz mode is greater than for modes closer to it. For the supersonic jet, the relatively short distance between the Kelvin-Helmholtz mode and the low-angle acoustic modes allows PSE to retain them with reasonable accuracy. Still, the one-way Euler equations are much more accurate and represent the true eigenvalues almost perfectly. The main error in the PSE acoustic modes is an increase in wavelength (and therefore a reduction in phase speed), since the real parts of the eigenvalues move to higher values. There is, however, little excess damping. Since PSE already gives reasonable far-field sound predictions for supersonic jets, it is unclear how much the improvement achieved in the spectrum of the one-way Euler operator will ultimately improve noise predictions in this case.

For the subsonic jet, the distance between the Kelvin-Helmholtz mode and the downstream acoustic modes is comparatively large. As a result, the PSE acoustic modes contain much more error. Their phase velocity is much too low and they are also significantly damped. The one-way

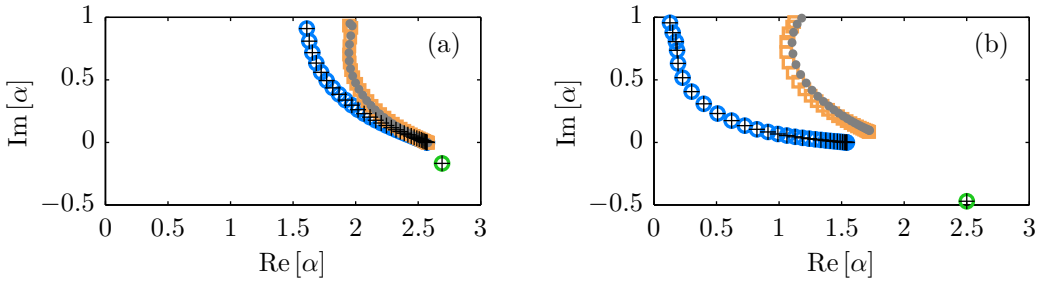


Figure 2.13: Comparison of the one-way Euler (+), standard PSE (□), and explicit damping PSE (●) low-angle acoustic modes to their full Euler counterparts (○) for the (a) supersonic and (b) subsonic jets. The one-way Euler modes are far more accurate than the PSE modes, especially for the subsonic jet. The location of the Kelvin-Helmholtz mode is also shown (○).

Euler acoustic modes, on the other hand, are represented extremely accurately. This suggests that the one-way Euler method is capable of delivering greatly improved far-field noise predictions for subsonic jets, compared to PSE. This inference is confirmed in the next section.

#### 2.2.8.2 Linear wavepackets in a Mach 0.9 turbulent jet

Finally, we use the one-way equations to compute linear wavepackets and their associated acoustic radiation in a Mach 0.9 jet. The Navier-Stokes equations are linearized about the mean turbulent flow-field from a large-eddy-simulation of an isothermal Mach 0.9 jet (Brès et al. 2014, 2015). Axial second derivatives are neglected, as they are in other spatial marching methods such as the reduced and parabolized Navier-Stokes equations (Rubin & Tannehill 1992). Radial and azimuthal second derivatives are retained. As discussed in 2.2.1, this ruins the hyperbolicity of the continuous system, but has no bearing on the parabolization process since the semi-discrete system defined in equation (2.16) remains hyperbolic. The computational domain extends fifteen jet diameters in the radial direction, and is discretized with 600 points that are clustered near the jet lip line ($r = 1/2$).

Half a diameter downstream of the inlet, the local Kelvin-Helmholtz eigenfunction is specified as an incoming fluctuation. The system is solved using the one-way Euler equations with $N_\beta = 12$, and also using the parabolized stability equations, which have frequently been employed within the context of wavepacket-based jet noise modeling (Gudmundsson & Colonius 2011, Sinha et al. 2014). We also compare to a previous solution (Jordan et al. 2014) computed using time-domain integration,

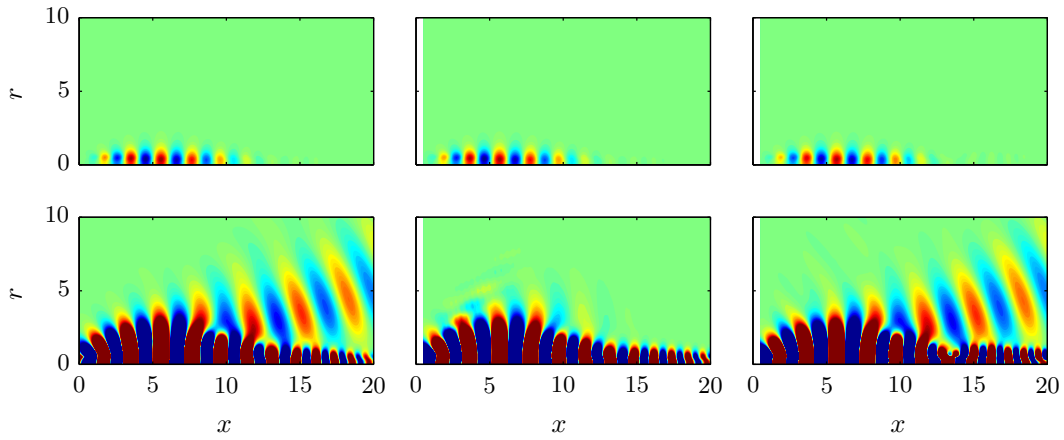


Figure 2.14: Contours of axisymmetric pressure fluctuations at $St = 0.35$ in a Mach 0.9 jet, scaled by the maximum amplitude. Top row: fifty equally spaced contour levels between $\pm 1$. Bottom row: fifty equally spaced contour levels between $\pm 4 \times 10^{-3}$, chosen to show acoustic radiation. First column: direct solution. Second column: PSE. Third column: one-way Euler equations. The one-way Euler solution captures both the near-field wavepacket and the associated acoustic radiation at a fraction of the cost of the direct solution, while PSE completely misses the acoustic radiation.

which we call the direct solution. Since this solution captures radiation is all directions, it can be thought of as the correct solution of the linear system.

Figure 2.14 shows the axisymmetric part of the pressure fluctuation at a Strouhal number of $St = \frac{fD}{U_{jet}} = 0.35$, which is near the most amplified frequency. The direct, PSE, and one-way Euler solutions appear in the first, second, and third column, respectively. In the top row, contour levels are chosen to show the near-field wavepacket, which is approximated well by both the PSE and one-way Euler solutions. In the bottom row, the contour levels are reduced to highlight the acoustic radiation, which is almost three orders of magnitude smaller than the near-field fluctuations. The direct solution contains a beam of acoustic radiation that propagates to the far-field. Unlike the PSE solution, the one-way Euler solution accurately captures this acoustic radiation. The advantage of the one-way solution over the direct solution is computational speed: the direct solution used 37.5 CPU hours while the one-way solution used only 1.2 CPU hours, a 34 times speed-up. For comparison, the PSE solution required 0.063 CPU hours, but this speed is achieved at the expense of accuracy.

### 2.2.9 Summary of the outflow method

We have formulated and demonstrated a method for constructing well-posed one-way approximations of hyperbolic equations. First, an exact one-way equation is derived for systems that do not vary in $x$. We then construct an efficient approximation of the exact equation based on recursions originally developed for generating nonreflecting boundary conditions. The approximate equations are shown to be well-posed and are able to approximate the exact equations with increasing accuracy as the order of the recursions is increased, provided that the recursion parameters are properly chosen. When the method is applied to $x$-dependent systems, the one-way equation remains well-posed, but physical accuracy is guaranteed only when the variation is sufficiently slow such that leftgoing waves do not significantly modify the evolution of the rightgoing waves. This is not a shortcoming of our formulation, but rather an inherent limitation on the class of problems for which a one-way solution strategy is sensible. Computational cost scaling estimates are derived that explain the improved efficiency of the approximate one-way equations over traditional solution methods.

Next, the method is applied to the linearized Euler equations. A process by which appropriate recursion parameters can be identified is described in detail, which can be used as a guide in the application of the method to other hyperbolic equations. In particular, analytical eigenvalues of the uniform flow Euler equations can be used as a proxy for the eigenvalues of the discretized nonuniform equations for the purpose of parameter selection. The utility of the resulting one-way Euler equations is then demonstrated using several example problems and the ability of the method to properly parabolize the Euler equations for typical jet profiles is demonstrated. Finally, when used to compute wavepackets in a Mach 0.9 jet, the one-way equations produce accurate results at a fraction of the cost of a direct method. Unlike PSE, the one-way solution properly captures the acoustic radiation.

## 2.3 One-way spatial integration – a projection approach

### 2.3.1 Introduction

In this section, we develop a second approach for the one-way spatial integration of hyperbolic equations that resolves two limitations of the method described in section 2.2.

First, the previous outflow method is not amenable to the inclusion of a forcing term on the right-hand-side of equation (2.15). Second, the outflow method assumes that the fluctuation specified at the computational inlet is composed of entirely incoming waves. From a theoretical perspective, this is a very reasonable assumption; in fact it must be true for the problem to be well-posed. In practice, however, it is common to work with boundary conditions that may not always satisfy this requirement, for example those extracted from experimental or computational data. It would be desirable for the method to automatically remove the unwanted incoming waves.

Both of these limitations can be alleviated by formulating a new one-way equation in terms of a particular projection operator that separates rightgoing and leftgoing waves. The remainder of section 2.3 describes the development and validation of this projection-based approach to one-way spatial integration.

### 2.3.2 Problem formulation

We begin with the non-homogeneous form of equation (2.15):

$$\frac{\partial q}{\partial t} + A\left(x,y\right)\frac{\partial q}{\partial x} + \sum_{j=1}^{d-1} B_j\left(x,y\right)\frac{\partial q}{\partial y_j} + C\left(x,y\right)q = f(x,y,t). \tag{2.65}$$

This is a special case of equation (1.9) and encompasses the Euler equations. The initial problem development then follows the same steps as in section 2.2.1, so for brevity we skip ahead to the modified form of equation (2.21):

$$\frac{d\hat{\boldsymbol{\phi}}}{dx} = \boldsymbol{M}\left(x,s\right)\hat{\boldsymbol{\phi}} + \hat{\boldsymbol{g}}\left(x,s\right). \tag{2.66}$$

$\boldsymbol{M}$ and $\hat{\boldsymbol{\phi}}$ retain their previous definitions, and $\hat{\boldsymbol{g}} = \tilde{\boldsymbol{A}}^{-1}\boldsymbol{T}\hat{\boldsymbol{g}}$, where $\tilde{\boldsymbol{A}}$ and $\boldsymbol{T}$ are defined by equation (2.17) and $\hat{\boldsymbol{f}}$ is the Laplace transform of the discretization of the inhomogeneous term $f$.

The rightgoing and leftgoing components of the solution of equation (2.66) can be identified based on the eigenvalues and eigenvectors of $\boldsymbol{M}$. Although Briggs' criteria (equations (2.26) and (2.27)) do not strictly apply to $x$-dependent systems, well-posedness theory (Kreiss 1970) can be evoked to reach the same conclusion: the mode associated with the eigenvalue $\alpha_k(x, s)$ is rightgoing at $x = x_0$ if

$$\lim_{\eta \to +\infty} \operatorname{Im}\left[\alpha_k\left(x_0, s\right)\right] = +\infty \tag{2.67}$$

and leftgoing if

$$\lim_{\eta \to +\infty} \operatorname{Im}\left[\alpha_k\left(x_0, s\right)\right] = -\infty. \tag{2.68}$$

The eigenvalue decomposition of $\boldsymbol{M}$ can be written

$$\boldsymbol{M} = \begin{bmatrix} \boldsymbol{V}_+ & \boldsymbol{V}_- \end{bmatrix} \begin{bmatrix} \boldsymbol{D}_{++} & \boldsymbol{0} \\ \boldsymbol{0} & \boldsymbol{D}_{--} \end{bmatrix} \begin{bmatrix} \boldsymbol{U}_+ \\ \boldsymbol{U}_- \end{bmatrix}, \tag{2.69}$$

where the columns of $\boldsymbol{V}_+ \in \mathbb{C}^{N \times N_+}$ and $\boldsymbol{V}_- \in \mathbb{C}^{N \times N_-}$ and the rows of $\boldsymbol{U}_+ \in \mathbb{C}^{N_+ \times N}$ and $\boldsymbol{U}_- \in \mathbb{C}^{N_- \times N}$ contain the left and right eigenvectors associated with the rightgoing and leftgoing eigenvalues of $\boldsymbol{M}$, respectively, which are contained in the diagonal matrices $\boldsymbol{D}_{++} \in \mathbb{C}^{N_+ \times N_+}$ and $\boldsymbol{D}_{--} \in \mathbb{C}^{N_- \times N_-}$. The eigenvectors are normalized such that

$$\begin{bmatrix} \boldsymbol{V}_+ & \boldsymbol{V}_- \end{bmatrix} \begin{bmatrix} \boldsymbol{U}_+ \\ \boldsymbol{U}_- \end{bmatrix} = \begin{bmatrix} \boldsymbol{U}_+ \\ \boldsymbol{U}_- \end{bmatrix} \begin{bmatrix} \boldsymbol{V}_+ & \boldsymbol{V}_- \end{bmatrix} = \boldsymbol{I}. \tag{2.70}$$

This partitioning of the eigenvectors can be related to that used in the previous section:

$$\boldsymbol{V}_+ = \begin{bmatrix} \boldsymbol{V}_{++} \\ \boldsymbol{V}_{-+} \end{bmatrix} \quad \boldsymbol{V}_- = \begin{bmatrix} \boldsymbol{V}_{+-} \\ \boldsymbol{V}_{--} \end{bmatrix} \quad \boldsymbol{U}_+ = \begin{bmatrix} \boldsymbol{U}_{++} & \boldsymbol{U}_{+-} \end{bmatrix} \quad \boldsymbol{U}_- = \begin{bmatrix} \boldsymbol{U}_{-+} & \boldsymbol{U}_{--} \end{bmatrix}. \tag{2.71}$$

The solution of equation (2.66) can be written as a summation over the right eigenvectors (as in equation (2.24)):

$$\hat{\boldsymbol{\phi}} = \boldsymbol{V}_+ \boldsymbol{\psi}_+ + \boldsymbol{V}_- \boldsymbol{\psi}_-, \tag{2.72}$$

where $\boldsymbol{\psi}_+$ and $\boldsymbol{\psi}_-$ are vectors of expansion coefficients for the rightgoing and leftgoing modes, respectively. Therefore, the rightgoing part of the solution is

$$\hat{\boldsymbol{\phi}}' = \boldsymbol{V}_+ \boldsymbol{\psi}_+ \tag{2.73}$$

and the leftgoing part is

$$\hat{\boldsymbol{\phi}}'' = \boldsymbol{V}_- \boldsymbol{\psi}_-. \tag{2.74}$$

### 2.3.3 Exact projection operator

Next, we define a projection operator that exactly splits the solution $\hat{\boldsymbol{\phi}}$ into rightgoing and leftgoing components at each $x$:

$$\boldsymbol{P} = \begin{bmatrix} \boldsymbol{V}_+ & \boldsymbol{V}_- \end{bmatrix} \begin{bmatrix} \boldsymbol{I} & \boldsymbol{0} \\ \boldsymbol{0} & \boldsymbol{0} \end{bmatrix} \begin{bmatrix} \boldsymbol{U}_+ \\ \boldsymbol{U}_- \end{bmatrix}, \tag{2.75}$$

and

$$\hat{\boldsymbol{\phi}}' = \boldsymbol{P}\hat{\boldsymbol{\phi}}, \tag{2.76a}$$

$$\hat{\boldsymbol{\phi}}'' = (\boldsymbol{I} - \boldsymbol{P})\,\hat{\boldsymbol{\phi}}. \tag{2.76b}$$

To show that $\boldsymbol{P}$ is a projection, we verify that $\boldsymbol{P}\boldsymbol{P} = \boldsymbol{P}$ using equations (2.75) and (2.70):

$$\boldsymbol{P}\boldsymbol{P} = \begin{bmatrix} \boldsymbol{V}_+ & \boldsymbol{V}_- \end{bmatrix} \begin{bmatrix} \boldsymbol{I} & \boldsymbol{0} \\ \boldsymbol{0} & \boldsymbol{0} \end{bmatrix} \begin{bmatrix} \boldsymbol{U}_+ \\ \boldsymbol{U}_- \end{bmatrix} \begin{bmatrix} \boldsymbol{V}_+ & \boldsymbol{V}_- \end{bmatrix} \begin{bmatrix} \boldsymbol{I} & \boldsymbol{0} \\ \boldsymbol{0} & \boldsymbol{0} \end{bmatrix} \begin{bmatrix} \boldsymbol{U}_+ \\ \boldsymbol{U}_- \end{bmatrix} \tag{2.77a}$$

$$= \begin{bmatrix} \boldsymbol{V}_+ & \boldsymbol{V}_- \end{bmatrix} \begin{bmatrix} \boldsymbol{I} & \boldsymbol{0} \\ \boldsymbol{0} & \boldsymbol{0} \end{bmatrix} \begin{bmatrix} \boldsymbol{I} & \boldsymbol{0} \\ \boldsymbol{0} & \boldsymbol{I} \end{bmatrix} \begin{bmatrix} \boldsymbol{I} & \boldsymbol{0} \\ \boldsymbol{0} & \boldsymbol{0} \end{bmatrix} \begin{bmatrix} \boldsymbol{U}_+ \\ \boldsymbol{U}_- \end{bmatrix} \tag{2.77b}$$

$$= \begin{bmatrix} \boldsymbol{V}_+ & \boldsymbol{V}_- \end{bmatrix} \begin{bmatrix} \boldsymbol{I} & \boldsymbol{0} \\ \boldsymbol{0} & \boldsymbol{0} \end{bmatrix} \begin{bmatrix} \boldsymbol{U}_+ \\ \boldsymbol{U}_- \end{bmatrix} \tag{2.77c}$$

$$= \boldsymbol{P}. \tag{2.77d}$$

Equation (2.76a) follows from equations (2.72) and (2.73):

$$\boldsymbol{P}\hat{\boldsymbol{\phi}} = \begin{bmatrix} \boldsymbol{V}_+ & \boldsymbol{V}_- \end{bmatrix} \begin{bmatrix} \boldsymbol{I} & \boldsymbol{0} \\ \boldsymbol{0} & \boldsymbol{0} \end{bmatrix} \begin{bmatrix} \boldsymbol{U}_+ \\ \boldsymbol{U}_- \end{bmatrix} \begin{bmatrix} \boldsymbol{V}_+ & \boldsymbol{V}_- \end{bmatrix} \begin{bmatrix} \boldsymbol{\psi}_+ \\ \boldsymbol{\psi}_- \end{bmatrix} \tag{2.78a}$$

$$= \begin{bmatrix} \boldsymbol{V}_+ & \boldsymbol{V}_- \end{bmatrix} \begin{bmatrix} \boldsymbol{I} & \boldsymbol{0} \\ \boldsymbol{0} & \boldsymbol{0} \end{bmatrix} \begin{bmatrix} \boldsymbol{I} & \boldsymbol{0} \\ \boldsymbol{0} & \boldsymbol{I} \end{bmatrix} \begin{bmatrix} \boldsymbol{\psi}_+ \\ \boldsymbol{\psi}_- \end{bmatrix} \tag{2.78b}$$

$$= \begin{bmatrix} \boldsymbol{V}_+ & \boldsymbol{V}_- \end{bmatrix} \begin{bmatrix} \boldsymbol{I} & \boldsymbol{0} \\ \boldsymbol{0} & \boldsymbol{0} \end{bmatrix} \begin{bmatrix} \boldsymbol{\psi}_+ \\ \boldsymbol{\psi}_- \end{bmatrix} \tag{2.78c}$$

$$= \boldsymbol{V}_+\boldsymbol{\psi}_+ \tag{2.78d}$$

$$= \hat{\boldsymbol{\phi}}'. \tag{2.78e}$$

Similarly, using that

$$\boldsymbol{I}-\boldsymbol{P}=\begin{bmatrix}\boldsymbol{V}_+ & \boldsymbol{V}_-\end{bmatrix}\begin{bmatrix}\boldsymbol{0} & \boldsymbol{0}\\ \boldsymbol{0} & \boldsymbol{I}\end{bmatrix}\begin{bmatrix}\boldsymbol{U}_+\\ \boldsymbol{U}_-\end{bmatrix}, \tag{2.79}$$

equation (2.76b) follows from equations (2.72) and (2.74):

$$(\boldsymbol{I}-\boldsymbol{P})\,\hat{\boldsymbol{\phi}}=\begin{bmatrix}\boldsymbol{V}_+ & \boldsymbol{V}_-\end{bmatrix}\begin{bmatrix}\boldsymbol{0} & \boldsymbol{0}\\ \boldsymbol{0} & \boldsymbol{I}\end{bmatrix}\begin{bmatrix}\boldsymbol{U}_+\\ \boldsymbol{U}_-\end{bmatrix}\begin{bmatrix}\boldsymbol{V}_+ & \boldsymbol{V}_-\end{bmatrix}\begin{bmatrix}\boldsymbol{\psi}_+\\ \boldsymbol{\psi}_-\end{bmatrix} \tag{2.80a}$$

$$=\begin{bmatrix}\boldsymbol{V}_+ & \boldsymbol{V}_-\end{bmatrix}\begin{bmatrix}\boldsymbol{0} & \boldsymbol{0}\\ \boldsymbol{0} & \boldsymbol{I}\end{bmatrix}\begin{bmatrix}\boldsymbol{I} & \boldsymbol{0}\\ \boldsymbol{0} & \boldsymbol{I}\end{bmatrix}\begin{bmatrix}\boldsymbol{\psi}_+\\ \boldsymbol{\psi}_-\end{bmatrix} \tag{2.80b}$$

$$=\begin{bmatrix}\boldsymbol{V}_+ & \boldsymbol{V}_-\end{bmatrix}\begin{bmatrix}\boldsymbol{0} & \boldsymbol{0}\\ \boldsymbol{0} & \boldsymbol{I}\end{bmatrix}\begin{bmatrix}\boldsymbol{\psi}_+\\ \boldsymbol{\psi}_-\end{bmatrix} \tag{2.80c}$$

$$=\boldsymbol{V}_-\boldsymbol{\psi}_- \tag{2.80d}$$

$$=\hat{\boldsymbol{\phi}}''. \tag{2.80e}$$

### 2.3.4 One-way equation

We now obtain a one-way equation for the rightgoing component of the solution $\hat{\boldsymbol{\phi}}'$ by applying the projection $\boldsymbol{P}$ to equation (2.66). This gives

$$\boldsymbol{P}\frac{d\hat{\boldsymbol{\phi}}}{dx}=\boldsymbol{P}\boldsymbol{M}\hat{\boldsymbol{\phi}}+\boldsymbol{P}\hat{\boldsymbol{g}}. \tag{2.81}$$

To obtain an evolution equation for $\hat{\boldsymbol{\phi}}'$, we must move $\boldsymbol{P}$ inside the derivative. Using the chain rule, we have

$$\frac{d\hat{\boldsymbol{\phi}}'}{dx}=\frac{d\boldsymbol{P}\hat{\boldsymbol{\phi}}}{dx}=\boldsymbol{P}\frac{d\hat{\boldsymbol{\phi}}}{dx}+\frac{d\boldsymbol{P}}{dx}\hat{\boldsymbol{\phi}}. \tag{2.82}$$

Using that $\boldsymbol{P}$ and $\boldsymbol{M}$ commute (since they have the same eigenvectors by equations (2.69) and (2.75)), the first term on the right-hand-side of equation (2.81) can also be written in terms of $\hat{\boldsymbol{\phi}}'$:

$$\boldsymbol{P}\boldsymbol{M}\hat{\boldsymbol{\phi}} = \boldsymbol{P}\boldsymbol{P}\boldsymbol{M}\hat{\boldsymbol{\phi}} = \boldsymbol{P}\boldsymbol{M}\boldsymbol{P}\hat{\boldsymbol{\phi}} = \boldsymbol{P}\boldsymbol{M}\hat{\boldsymbol{\phi}}'. \tag{2.83}$$

Therefore, using equations (2.82) and (2.83), equation (2.81) can be written

$$\frac{d\hat{\boldsymbol{\phi}}'}{dx} = \boldsymbol{P}\left(\boldsymbol{M}\hat{\boldsymbol{\phi}}' + \hat{\boldsymbol{g}}\right) + \frac{d\boldsymbol{P}}{dx}\hat{\boldsymbol{\phi}}. \tag{2.84}$$

Following the same steps, but with $\boldsymbol{I} - \boldsymbol{P}$ replacing $\boldsymbol{P}$, we similarly obtain

$$\frac{d\hat{\boldsymbol{\phi}}''}{dx} = (\boldsymbol{I} - \boldsymbol{P})\left(\boldsymbol{M}\hat{\boldsymbol{\phi}}'' + \hat{\boldsymbol{g}}\right) - \frac{d\boldsymbol{P}}{dx}\hat{\boldsymbol{\phi}}. \tag{2.85}$$

By neglecting $\frac{d\boldsymbol{P}}{dx}\hat{\boldsymbol{\phi}}$ in equations (2.84) and (2.85), we arrive at the following one-way equations for the rightgoing and leftgoing components of the solution:

$$\frac{d\hat{\boldsymbol{\phi}}'}{dx} = \boldsymbol{P}\left(\boldsymbol{M}\hat{\boldsymbol{\phi}}' + \hat{\boldsymbol{g}}\right), \tag{2.86}$$

$$\frac{d\hat{\boldsymbol{\phi}}''}{dx} = (\boldsymbol{I} - \boldsymbol{P})\left(\boldsymbol{M}\hat{\boldsymbol{\phi}}'' + \hat{\boldsymbol{g}}\right). \tag{2.87}$$

When $\boldsymbol{M}$ is $x$-independent, $\frac{d\boldsymbol{P}}{dx} = \boldsymbol{0}$ and equations (2.86) and (2.87) exactly describe the evolution of rightgoing and leftgoing waves, respectively. When $\boldsymbol{M}$ is $x$-dependent, $\frac{d\boldsymbol{P}}{dx} \neq \boldsymbol{0}$ and equations (2.86) and (2.87) are approximate. Insight into the nature of the approximation can be gained by solving both equation (2.84) and equation (2.85) for $\frac{d\boldsymbol{P}}{dx}\hat{\boldsymbol{\phi}}$ and equating the expressions:

$$\frac{d\hat{\boldsymbol{\phi}}'}{dx} - \boldsymbol{P}\left(\boldsymbol{M}\hat{\boldsymbol{\phi}}' + \hat{\boldsymbol{g}}\right) = -\left(\frac{d\hat{\boldsymbol{\phi}}''}{dx} - (\boldsymbol{I} - \boldsymbol{P})\left(\boldsymbol{M}\hat{\boldsymbol{\phi}}'' + \hat{\boldsymbol{g}}\right)\right) = \frac{d\boldsymbol{P}}{dx}\hat{\boldsymbol{\phi}}. \tag{2.88}$$

Comparing equations (2.86) and (2.88) reveals that neglecting $\frac{d\boldsymbol{P}}{dx}\hat{\boldsymbol{\phi}}$ is equivalent to setting $\boldsymbol{\phi}'' = 0$

when calculating $\boldsymbol{\phi}'$. In other words, the one-way equation (2.86) neglects the influence of the leftgoing waves on the evolution of the rightgoing waves. In the same way, comparing equations (2.87) and (2.88) reveals that neglecting $\frac{d\boldsymbol{P}}{dx}\hat{\boldsymbol{\phi}}$ is equivalent to setting $\boldsymbol{\phi}' = 0$ when calculating $\boldsymbol{\phi}''$; the one-way equation (2.87) neglects the influence of the rightgoing waves on the evolution of the leftgoing waves. As discussed in detail in section 2.2.4, it is reasonable to neglect the influence of leftgoing waves on the rightgoing waves (and vice versa) when $\boldsymbol{M}$ is *slowly-varying* in $x$.

Next, we'll show that equations (2.86) and (2.87) are well-posed as one-way equations. This amounts to showing that their eigenvalues correspond to rightgoing and leftgoing modes, respectively. Focusing first on equation (2.86), the relevant operator is

$$\boldsymbol{PM} = \begin{bmatrix} \boldsymbol{V}_+ & \boldsymbol{V}_- \end{bmatrix} \begin{bmatrix} \boldsymbol{I} & \boldsymbol{0} \\ \boldsymbol{0} & \boldsymbol{0} \end{bmatrix} \begin{bmatrix} \boldsymbol{U}_+ \\ \boldsymbol{U}_- \end{bmatrix} \begin{bmatrix} \boldsymbol{V}_+ & \boldsymbol{V}_- \end{bmatrix} \begin{bmatrix} \boldsymbol{D}_{++} & \boldsymbol{0} \\ \boldsymbol{0} & \boldsymbol{D}_{--} \end{bmatrix} \begin{bmatrix} \boldsymbol{U}_+ \\ \boldsymbol{U}_- \end{bmatrix} \tag{2.89a}$$

$$= \begin{bmatrix} \boldsymbol{V}_+ & \boldsymbol{V}_- \end{bmatrix} \begin{bmatrix} \boldsymbol{D}_{++} & \boldsymbol{0} \\ \boldsymbol{0} & \boldsymbol{0} \end{bmatrix} \begin{bmatrix} \boldsymbol{U}_+ \\ \boldsymbol{U}_- \end{bmatrix}. \tag{2.89b}$$

Therefore, compared to the original elliptic operator $\boldsymbol{M}$, the eigenvectors and rightgoing eigenvalues of the one-way operator $\boldsymbol{PM}$ are unchanged, but the leftgoing eigenvalues have been eliminated. Therefore, equation (2.86) is well-posed as a one-way equation and can be solved by integrating the equations in the positive $x$ direction.

The relevant operator for the well-posedness of equation (2.87) is

$$(\boldsymbol{I} - \boldsymbol{PM}) = \begin{bmatrix} \boldsymbol{V}_+ & \boldsymbol{V}_- \end{bmatrix} \begin{bmatrix} \boldsymbol{0} & \boldsymbol{0} \\ \boldsymbol{0} & \boldsymbol{I} \end{bmatrix} \begin{bmatrix} \boldsymbol{U}_+ \\ \boldsymbol{U}_- \end{bmatrix} \begin{bmatrix} \boldsymbol{V}_+ & \boldsymbol{V}_- \end{bmatrix} \begin{bmatrix} \boldsymbol{D}_{++} & \boldsymbol{0} \\ \boldsymbol{0} & \boldsymbol{D}_{--} \end{bmatrix} \begin{bmatrix} \boldsymbol{U}_+ \\ \boldsymbol{U}_- \end{bmatrix} \tag{2.90a}$$

$$= \begin{bmatrix} \boldsymbol{V}_+ & \boldsymbol{V}_- \end{bmatrix} \begin{bmatrix} \boldsymbol{0} & \boldsymbol{0} \\ \boldsymbol{0} & \boldsymbol{D}_{--} \end{bmatrix} \begin{bmatrix} \boldsymbol{U}_+ \\ \boldsymbol{U}_- \end{bmatrix}. \tag{2.90b}$$

The rightgoing eigenvalues have been eliminated, so equation (2.87) is well-posed as a one-way equation and can be solved by integrating the equations in the negative $x$ direction.

### 2.3.5 Approximated projection operator

The eigen-decomposition of $\boldsymbol{M}$ is required at every $x$ to construct the exact projection $\boldsymbol{P}$, resulting in intolerably high computational cost. We therefore construct an approximation of $\boldsymbol{P}$ that can be efficiently computed. Specifically, the following recursions approximate the action of $\boldsymbol{P}$ on an arbitrary vector $\hat{\boldsymbol{\phi}}$:

$$\hat{\boldsymbol{\phi}}_{+}^{-N_\beta} = 0 \tag{2.91a}$$

$$\left(\boldsymbol{M} - i\beta_{-}^{j}\boldsymbol{I}\right)\hat{\boldsymbol{\phi}}^{-j} - \left(\boldsymbol{M} - i\beta_{+}^{j}\boldsymbol{I}\right)\hat{\boldsymbol{\phi}}^{-j-1} = 0 \qquad j = 1, \ldots, N_\beta - 1 \tag{2.91b}$$

$$\left(\boldsymbol{M} - i\beta_{-}^{0}\boldsymbol{I}\right)\hat{\boldsymbol{\phi}}^{0} - \left(\boldsymbol{M} - i\beta_{+}^{0}\boldsymbol{I}\right)\hat{\boldsymbol{\phi}}^{-1} = \left(\boldsymbol{M} - i\beta_{-}^{0}\boldsymbol{I}\right)\hat{\boldsymbol{\phi}} \tag{2.91c}$$

$$\left(\boldsymbol{M} - i\beta_{+}^{j}\boldsymbol{I}\right)\hat{\boldsymbol{\phi}}^{j} - \left(\boldsymbol{M} - i\beta_{-}^{j}\boldsymbol{I}\right)\hat{\boldsymbol{\phi}}^{j+1} = 0 \qquad j = 0, \ldots, N_\beta - 1 \tag{2.91d}$$

$$\hat{\boldsymbol{\phi}}_{-}^{N_\beta} = 0. \tag{2.91e}$$

Here, we have introduced a set of auxiliary variables $\{\hat{\boldsymbol{\phi}}^j : j = -N_\beta, \ldots, N_\beta\}$ and a set of complex scalar recursion parameters $\{\beta_{+}^{j}, \beta_{-}^{j} : j = 0, \ldots, N_\beta - 1\}$. $N_\beta$ is the order of the approximate projection.

We will now show that the zero-indexed variable is the approximate projection of $\hat{\boldsymbol{\phi}}$ (a.k.a. $\hat{\boldsymbol{\phi}}^0 \approx \hat{\boldsymbol{\phi}}'$), and that the approximation converges as $N_\beta \to \infty$ provided that the recursion parameters are appropriately chosen. We begin by writing equations (2.91b) - (2.91d) in terms of the expansion coefficients $\boldsymbol{\psi}^j = \boldsymbol{U}\hat{\boldsymbol{\phi}}^j$:

$$\left(\boldsymbol{D} - i\beta_{-}^{j}\boldsymbol{I}\right)\boldsymbol{\psi}^{-j} - \left(\boldsymbol{D} - i\beta_{+}^{j}\boldsymbol{I}\right)\boldsymbol{\psi}^{-j-1} = 0 \qquad j = 1, \ldots, N_\beta - 1 \tag{2.92a}$$

$$\left(\boldsymbol{D} - i\beta_{-}^{0}\boldsymbol{I}\right)\boldsymbol{\psi}^{0} - \left(\boldsymbol{D} - i\beta_{+}^{0}\boldsymbol{I}\right)\boldsymbol{\psi}^{-1} = \left(\boldsymbol{D} - i\beta_{-}^{0}\boldsymbol{I}\right)\boldsymbol{\psi} \tag{2.92b}$$

$$\left(\boldsymbol{D} - i\beta_{+}^{j}\boldsymbol{I}\right)\boldsymbol{\psi}^{j} - \left(\boldsymbol{D} - i\beta_{-}^{j}\boldsymbol{I}\right)\boldsymbol{\psi}^{j+1} = 0 \qquad j = 0, \ldots, N_\beta - 1. \tag{2.92c}$$

Since $\boldsymbol{D}$ is diagonal, each scalar component of $\boldsymbol{\psi}^j$ can be treated separately:

$$\left(i\alpha_k - i\beta_-^j \boldsymbol{I}\right)\boldsymbol{\psi}_k^{-j} - \left(i\alpha_k - i\beta_+^j \boldsymbol{I}\right)\boldsymbol{\psi}_k^{-j-1} = 0 \qquad j = 1,\ldots,N_\beta - 1 \tag{2.93a}$$

$$\left(i\alpha_k - i\beta_-^0 \boldsymbol{I}\right)\boldsymbol{\psi}_k^{0} - \left(i\alpha_k - i\beta_+^0 \boldsymbol{I}\right)\boldsymbol{\psi}_k^{-1} = \left(i\alpha_k - i\beta_-^0 \boldsymbol{I}\right)\boldsymbol{\psi}_k \tag{2.93b}$$

$$\left(i\alpha_k - i\beta_+^j \boldsymbol{I}\right)\boldsymbol{\psi}_k^{j} - \left(i\alpha_k - i\beta_-^j \boldsymbol{I}\right)\boldsymbol{\psi}_k^{j+1} = 0 \qquad j = 0,\ldots,N_\beta - 1 \tag{2.93c}$$

for $k = 1,\ldots,N$. The intermediate auxiliary variables ($j = -N_\beta + 1,\ldots,N_\beta - 1$) can then be easily eliminated, leaving

$$\boldsymbol{\psi}_k^{-N_\beta} = \mathcal{F}^{-1}(\alpha_k)\left(\boldsymbol{\psi}_k^0 - \boldsymbol{\psi}_k\right), \tag{2.94a}$$

$$\boldsymbol{\psi}_k^{N_\beta} = \mathcal{F}(\alpha_k)\boldsymbol{\psi}_k^0. \tag{2.94b}$$

The function $\mathcal{F}(\alpha)$ is the same as in equation (2.43). Equation (2.95) can be written for all $k$ as

$$\begin{Bmatrix} \boldsymbol{\psi}_+^{-N_\beta} \\ \boldsymbol{\psi}_-^{-N_\beta} \end{Bmatrix} = \begin{bmatrix} \boldsymbol{F}_{++}^{-1} & \boldsymbol{0} \\ \boldsymbol{0} & \boldsymbol{F}_{--}^{-1} \end{bmatrix} \begin{Bmatrix} \boldsymbol{\psi}_+^0 - \boldsymbol{\psi}_+ \\ \boldsymbol{\psi}_-^0 - \boldsymbol{\psi}_- \end{Bmatrix}, \tag{2.95a}$$

$$\begin{Bmatrix} \boldsymbol{\psi}_+^{N_\beta} \\ \boldsymbol{\psi}_-^{N_\beta} \end{Bmatrix} = \begin{bmatrix} \boldsymbol{F}_{++} & \boldsymbol{0} \\ \boldsymbol{0} & \boldsymbol{F}_{--} \end{bmatrix} \begin{Bmatrix} \boldsymbol{\psi}_+^0 \\ \boldsymbol{\psi}_-^0 \end{Bmatrix}, \tag{2.95b}$$

where, as before, $\boldsymbol{F}_{++}$ and $\boldsymbol{F}_{--}$ are diagonal matrices whose entries are the values of $\mathcal{F}(\alpha)$ associated with each rightgoing and leftgoing eigenvalue, respectively.

To apply the termination conditions given by equations (2.91a) and (2.91e), first write the left-hand-sides of equation (2.95) in terms of $\hat{\boldsymbol{\phi}}^{\pm N_\beta}$:

$$\begin{bmatrix} \boldsymbol{U}_{++} & \boldsymbol{U}_{+-} \\ \boldsymbol{U}_{-+} & \boldsymbol{U}_{--} \end{bmatrix} \begin{Bmatrix} \hat{\boldsymbol{\phi}}_+^{-N_\beta} \\ \hat{\boldsymbol{\phi}}_-^{-N_\beta} \end{Bmatrix} = \begin{bmatrix} \boldsymbol{F}_{++}^{-1} & \boldsymbol{0} \\ \boldsymbol{0} & \boldsymbol{F}_{--}^{-1} \end{bmatrix} \begin{Bmatrix} \boldsymbol{\psi}_+^0 - \boldsymbol{\psi}_+ \\ \boldsymbol{\psi}_-^0 - \boldsymbol{\psi}_- \end{Bmatrix}, \tag{2.96a}$$

$$\begin{bmatrix} \boldsymbol{U}_{++} & \boldsymbol{U}_{+-} \\ \boldsymbol{U}_{-+} & \boldsymbol{U}_{--} \end{bmatrix} \begin{Bmatrix} \hat{\boldsymbol{\phi}}_+^{N_\beta} \\ \hat{\boldsymbol{\phi}}_-^{N_\beta} \end{Bmatrix} = \begin{bmatrix} \boldsymbol{F}_{++} & \boldsymbol{0} \\ \boldsymbol{0} & \boldsymbol{F}_{--} \end{bmatrix} \begin{Bmatrix} \boldsymbol{\psi}_+^0 \\ \boldsymbol{\psi}_-^0 \end{Bmatrix}. \tag{2.96b}$$

Applying equations (2.91a) and (2.91e) and eliminating $\hat{\boldsymbol{\phi}}_{-}^{-N_\beta}$ and $\hat{\boldsymbol{\phi}}_{+}^{N_\beta}$ leaves

$$\begin{bmatrix} \boldsymbol{I} & -\boldsymbol{R}_{+-} \\ -\boldsymbol{R}_{-+} & \boldsymbol{I} \end{bmatrix} \begin{Bmatrix} \boldsymbol{\psi}_{+}^{0} \\ \boldsymbol{\psi}_{-}^{0} \end{Bmatrix} = \begin{bmatrix} \boldsymbol{I} & \boldsymbol{0} \\ \boldsymbol{0} & \boldsymbol{0} \end{bmatrix} \begin{bmatrix} \boldsymbol{I} & -\boldsymbol{R}_{+-} \\ -\boldsymbol{R}_{-+} & \boldsymbol{I} \end{bmatrix} \begin{Bmatrix} \boldsymbol{\psi}_{+} \\ \boldsymbol{\psi}_{-} \end{Bmatrix} \tag{2.97}$$

with

$$\boldsymbol{R}_{+-} = \boldsymbol{F}_{++}\boldsymbol{W}_{+-}\boldsymbol{F}_{--}^{-1}, \tag{2.98a}$$

$$\boldsymbol{R}_{-+} = \boldsymbol{F}_{--}^{-1}\boldsymbol{W}_{-+}\boldsymbol{F}_{++}, \tag{2.98b}$$

and

$$\boldsymbol{W}_{+-} = \boldsymbol{U}_{-+}\boldsymbol{U}_{++}^{-1}, \tag{2.99a}$$

$$\boldsymbol{W}_{-+} = \boldsymbol{U}_{+-}\boldsymbol{U}_{--}^{-1}. \tag{2.99b}$$

Solving equation (2.97) for $\boldsymbol{\psi}^0$ and reverting to $\hat{\boldsymbol{\phi}}$ variables gives

$$\hat{\boldsymbol{\phi}}^{0} = \boldsymbol{P}_{N_\beta}\hat{\boldsymbol{\phi}}, \tag{2.100}$$

where

$$\boldsymbol{P}_{N_\beta} = \begin{bmatrix} \boldsymbol{V}_{+} & \boldsymbol{V}_{-} \end{bmatrix} \begin{bmatrix} \boldsymbol{I} & -\boldsymbol{R}_{+-} \\ -\boldsymbol{R}_{-+} & \boldsymbol{I} \end{bmatrix}^{-1} \begin{bmatrix} \boldsymbol{I} & \boldsymbol{0} \\ \boldsymbol{0} & \boldsymbol{0} \end{bmatrix} \begin{bmatrix} \boldsymbol{I} & -\boldsymbol{R}_{+-} \\ -\boldsymbol{R}_{-+} & \boldsymbol{I} \end{bmatrix} \begin{bmatrix} \boldsymbol{U}_{+} \\ \boldsymbol{U}_{-} \end{bmatrix}. \tag{2.101}$$

$\boldsymbol{P}_{N_\beta}$ is the approximation of the exact projection $\boldsymbol{P}$ that is implicitly defined by equation (2.91). It is easy to verify that $\boldsymbol{P}_{N_\beta}\boldsymbol{P}_{N_\beta} = \boldsymbol{P}_{N_\beta}$ so $\boldsymbol{P}_{N_\beta}$ is itself a projection. Furthermore, comparing equations (2.75) and (2.101), we see that $\boldsymbol{P}_{N_\beta} \to \boldsymbol{P}$ as $\boldsymbol{R}_{+-}, \boldsymbol{R}_{+-} \to \boldsymbol{0}$. Therefore, the approximation converges if every entry of $\boldsymbol{R}_{+-}$ and $\boldsymbol{R}_{+-}$ converge toward zero as the order of the approximation

increases. These entries take the form

$$(\boldsymbol{r}_{+-})_{nm} = \frac{\mathcal{F}(\alpha_{+,n})}{\mathcal{F}(\alpha_{-,m})} (\boldsymbol{w}_{+-})_{nm}\,, \tag{2.102a}$$

$$(\boldsymbol{r}_{-+})_{mn} = \frac{\mathcal{F}(\alpha_{+,n})}{\mathcal{F}(\alpha_{-,m})} (\boldsymbol{w}_{-+})_{mn}\,, \tag{2.102b}$$

where $\alpha_{+,n}$ is the $n^{\text{th}}$ rightgoing eigenvalue, $\alpha_{-,m}$ is the $m^{\text{th}}$ leftgoing eigenvalue, $(\boldsymbol{w}_{+-})_{nm}$ is the $(n,m)$ entry of the weight matrix $\boldsymbol{W}_{+-}$, and $(\boldsymbol{w}_{-+})_{mn}$ is the $(m,n)$ entry of the weight matrix $\boldsymbol{W}_{-+}$. Since the weights are fixed, the recursion parameters must be chosen such that $\mathcal{F}(\alpha_{+,n})/\mathcal{F}(\alpha_{-,m})$ goes to zero for all $m,n$.

This is exactly the same requirement for convergence as derived for the approximate outflow-based one-way method in section 2.2.3. This has two important implications. First, as established in section 2.2.3, if $\alpha_{+,n} \neq \alpha_{-,m}$ for all $m$,$n$, there always exist recursion parameters that make the approximation error arbitrarily small. Second, any recursion parameters derived for the previous method can be used without modification for the projection approach, including those derived for the Euler equations in section 2.2.6.

Finally, we must show that equations (2.86) and (2.87) remain well-posed as one-way equations when $\boldsymbol{P}_{N_\beta}$ is used in place of $\boldsymbol{P}$. To do so, it suffices to show that $\boldsymbol{P}_{N_\beta} \to \boldsymbol{P}$ as $\eta \to \infty$, since we know that the eigenvalues of $\boldsymbol{PM}$ and $(\boldsymbol{I}-\boldsymbol{P})\,\boldsymbol{M}$ exhibit the correct behavior for well-posedness, as defined by equations (2.67) and (2.68), in this limit. Therefore, the task at hand is to show that $\boldsymbol{R}_{+-}$ and $\boldsymbol{R}_{-+}$ go to zero as $\eta \to \infty$. In this limit, $\boldsymbol{M}$ tends to the diagonal matrix $-\eta\tilde{\boldsymbol{A}}^{-1}$. Since it is diagonal, its eigenvector matrices are also diagonal and unitary; $\boldsymbol{U}_{++}$ and $\boldsymbol{U}_{--}$ are appropriate sized identity matrices and $\boldsymbol{U}_{+-}$ and $\boldsymbol{U}_{-+}$ are zero. Also, the eigenvalues of the asymptotic form of $\boldsymbol{M}$ approach infinity, which causes $\mathcal{F}(\alpha_k) \to 1$ for every $k$ since the recursion parameters are bounded as $\eta \to \infty$ (see section 2.2.3). Consequently, $\boldsymbol{F}_{++}$ and $\boldsymbol{F}_{--}$ become identity matrices. Putting this all together, we conclude from equation (2.98) that $\boldsymbol{R}_{+-}$ and $\boldsymbol{R}_{-+}$ go to zero as $\eta \to \infty$. Therefore, equations (2.86) and (2.87) are well-posed when $\boldsymbol{P}_{N_\beta}$ is used in place of $\boldsymbol{P}$.

### 2.3.6 Computational considerations

The recursions given by equation (2.91) can be written as

$$\hat{\boldsymbol{\phi}}^0 = \boldsymbol{P}_3 \hat{\boldsymbol{\phi}}^a, \tag{2.103a}$$

$$\boldsymbol{P}_2 \hat{\boldsymbol{\phi}}^a = \boldsymbol{P}_1 \hat{\boldsymbol{\phi}}. \tag{2.103b}$$

The matrices $\boldsymbol{P}_1 \in \mathbb{C}^{N_a \times N}$, $\boldsymbol{P}_2 \in \mathbb{C}^{N_a \times N_a}$, $\boldsymbol{P}_1 \in \mathbb{C}^{N \times N_a}$ are defined by the recursions, $\hat{\boldsymbol{\phi}}_a \in \mathbb{C}^{N_a}$ contains all of the $j \neq 0$ auxiliary variables, and $N_a = 2\left(N_\beta - 1\right) N \propto N_y N_\beta$.

Eliminating $\hat{\boldsymbol{\phi}}^a$ requires the solution of the matrix system given by equation (2.103b), whose leading dimension is $\mathcal{O}\left(N_y N_\beta\right)$. Comparing to the scaling derived in section 2.2.5, we see that the computational cost of the projection approach scales in the same way as the outflow approach. However, the actual size of the matrix system that must be solved is approximately two times larger for the projection method, since $N_a \approx 2N_*$. This reflects the fact that about twice as many auxiliary variables are defined at a given order for the projection approach relative to the outflow approach. Using again the $N_\beta^p$ scaling from section 2.2.5 for matrix equation solution, with $p \approx 1.5$, we conclude that the projection method is roughly $2^{1.5} \approx 3$ times more computationally costly. As before, we anticipate that an iterative approach for satisfying equation (2.103b) could substantially reduce the cost of the method.

An additional issue arises in the practical implementation of the method. Specifically, errors incurred during the numerical integration of equation (2.86) do not necessarily lie entirely in the rightgoing subspace. In other words, the numerical approximation of $\hat{\boldsymbol{\phi}}'$ collects an error that projects onto the zero eigenvalues of $\boldsymbol{P}_{N_\beta} \boldsymbol{M}$, which is then propagated along during the march. This causes an accumulation of error that contaminates the solution. Fortunately, there is an easy fix: apply the projection operator to the solution after each step in the march. Typically, this requires no additional computational effort, since the LU decomposition of the recursion equations that define the projection will have already been computed. This issue does not arise in the outflow-based method because there the rightgoing expansion coefficient is intrinsically zeroed (see equation (2.35b)), whereas in

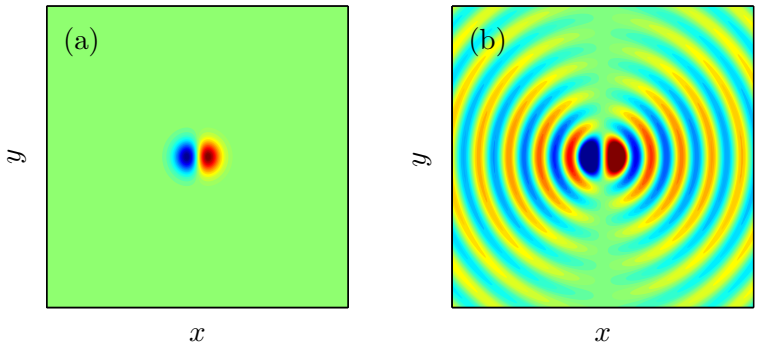


Figure 2.15: Dipole test case: (a) forcing applied to the energy equation, and (b) exact pressure response.

the projection-based approach, the *derivative* of the rightgoing expansion coefficient is zeroed:

$$\frac{\partial \psi_-}{\partial x} = 0. \tag{2.104}$$

This last equation is obtained by writing equation (2.86) in terms of expansion coefficients, assuming an $x$-independent operator.

### 2.3.7 Sample results

In this section, we present two example problems to demonstrate and validate the projection-based one-way approach. The starting point of both problems is the linearized Euler equations. The computational details are identical to those described in section 2.2.7, and the recursion parameters are selected using the strategies outlined in section 2.2.6.

#### 2.3.7.1 Dipole forcing of a quiescent fluid

In this problem, a dipole force is used to excite waves in an inviscid quiescent fluid. The right-hand-side force that is applied to the energy equation is shown in Figure 2.15(a), and the proper forcing terms are applied to the other equations in order to produce a dipole response in the pressure field, which is shown in Figure 2.15(b). This is an exact solution of the Euler equations.

We use the projection-based one-way equations to obtain an approximate solution. The com-

putational domain extends eight wavelengths in both $x$ and $y$ and is discretized using 200 equally spaced points in each direction. No incoming fluctuations are specified at the domain boundaries – the waves are excited exclusively by the inhomogeneous forcing terms. Note that the original outflow-based one-way equations cannot be used for this problem due to the non-zero forces.

The pressure-field obtained by integrating the one-way equations from left to right is shown in Figure 2.16(a). Clearly, the rightgoing waves are accurately captured. Similarly, the pressure-field obtained by integrating from right to left is shown in Figure 2.16(b). This time, the rightgoing waves are captured. Since the governing equations are $x$-independent in this problem, the full solution can be recovered by summing the rightgoing and leftgoing solutions, which is shown in Figure 2.16(c).

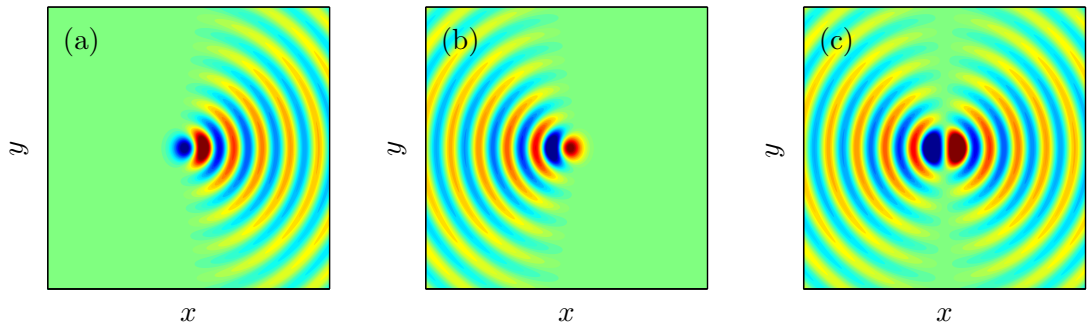


Figure 2.16: One-way approximation of the dipole response: (a) rightgoing solution, (b) leftgoing solution, (c) full solution recovered by summing the rightgoing and leftgoing solutions.

#### 2.3.7.2 Linear wavepackets in a Mach 0.9 turbulent jet

Finally, we repeat our previous problem of computing linear wavepackets in a Mach 0.9 turbulent jet to confirm that the projection-based method can deliver results that are equivalent to those obtained using the outflow-based method. Please refer to section 2.2.8.2 for the description and details of the problem set-up.

In Figure 2.17, the pressure field computed by the projection-based one-way method (bottom) is compared to that computed by the outflow-based one-way method (top). The only noticeable difference is that the solution from the projection-based method contains some additional acoustic radiation to high angles, but its magnitude is small compared to the dominant low-angle radiation.

Since the outflow-based solution compared well with a direct solution in section 2.2.8.2, we conclude that the projection-based method can likewise be used to efficiently compute wavepackets and their acoustic radiation in jets. As discussed in section 2.3.6, the projection-based method is approximately three times more computationally expensive than to the outflow-based method. For this problem, the two methods required 1.2 and 3.8 CPU hours, respectively.

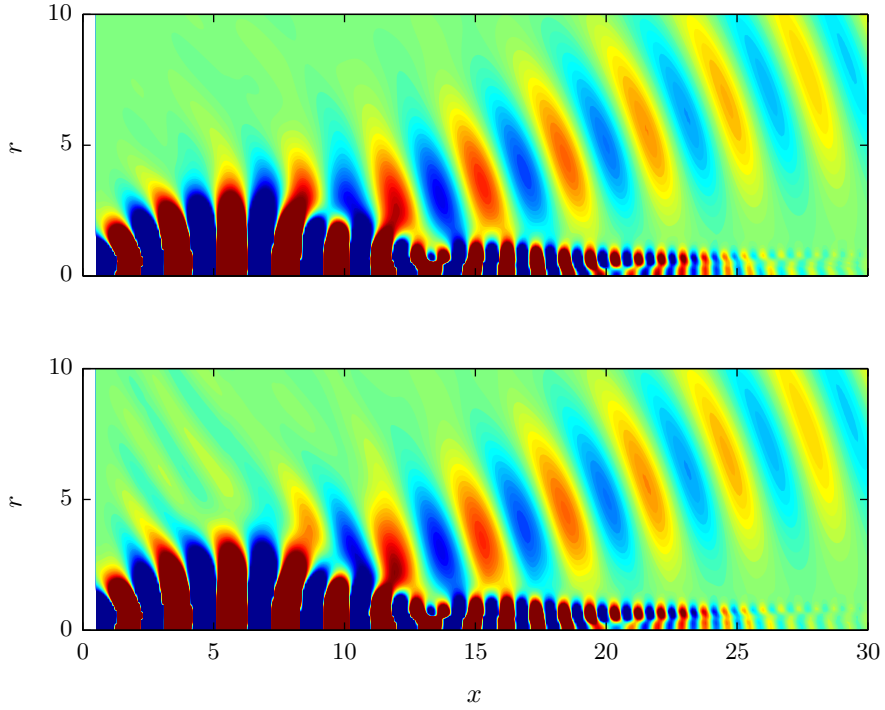


Figure 2.17: Wavepackets in a Mach 0.9 jet: comparison between outflow and projection one-way Euler solutions.

### 2.3.8 Summary of the projection method

In summary, we have formulated and verified a second well-posed spatial integration method for hyperbolic equations that resolves two limitation of the original outflow-based method, and in particular accommodates an inhomogeneous forcing term. The method is based on a recursive approximation of the projection operator that rigorously splits the solution vector into rightgoing and leftgoing components. It uses the same recursion parameters as the outflow-based method, and also inherits

its convergence properties. The ability of the method to accurately compute wavepackets and their acoustic radiation in a Mach 0.9 jet has been verified.

## 2.4 Chapter summary

This chapter has made two contributions related to solution methods for wavepacket models. First, we showed that the inability of the parabolized stability equations to capture acoustic radiation in subsonic jets is a consequence of regularization that is required to resolve the well-known ill-posedness of the method. The results of this analysis can be used to qualitatively and quantitatively understand how any quasi-local instability mode of the linear equations is effected by the PSE parabolization.

Second, we developed two alternative spatial integration methods that can be used to efficiently model wavepackets in jets. Unlike PSE, the new methods are well-posed and are capable of capturing both near-field wavepackets and their acoustic radiation. Compared to direct time domain or frequency domain solutions of the linearized flow equations, the one-way spatial integration methods offer an order-of-magnitude reduction in computational cost.

The methods are formulated for general hyperbolic equations and thus have potential applications outside of the context of jet noise modeling. The most obvious application is to inhomogeneous wave propagation problems that arise in many fields. Examples include underwater acoustics, medical imaging, seismology, and non-isotropic elastic wave problems. One-way equations based on our methodology for these problems could prove to be faster than traditional time domain methods and more accurate than existing one-way equations that are based on factorization and subsequent approximation of quasi-uniform analytical dispersion relations. Additional applications include noise, stability, and transition analysis of free-shear flows such as mixing-layers and jets, as well as wall-bounded flows (for which transverse viscous terms can be incorporated without hindering parabolization) ranging from classical flat-plate boundary layers to complicated swept wings. Unlike the parabolized stability equations, the one-way equations could capture multi-modal behavior within these problems, such as the generation of acoustic waves (as we've seen) or interaction between

multiple instability modes.

# Chapter 3

# Nonlinear and stochastic forcing of wavepackets

In this chapter, we turn our attention to the second main subject of this thesis – the nonlinear and stochastic forcing of wavepackets in jets.

## 3.1 Motivation and approach

As discussed in the introduction, the impact of nonlinear and stochastic forcing is entirely neglected in the majority of previous wavepacket models. The influence of turbulence in these models is therefore relegated to its role in establishing the mean flow field; it does not directly force the wavepackets. Instead, wavepackets are excited in the near-nozzle region using inlet perturbations and evolve linearly throughout the domain. These models produce good approximations of the average observed near-field wavepackets in both subsonic (Gudmundsson & Colonius 2011) and supersonic (Sinha et al. 2014) jets, but vastly under-predict the associated acoustic radiation in the subsonic case despite the close match in the near-field wavepacket (Baqui et al. 2013, Jordan et al. 2014).

A hypothesized explanation for this discrepancy is acoustic amplification due to wavepacket intermittency, or 'jitter'. Unlike the wavepackets obtained from unforced linear models, real wavepackets undergo intermittent, low frequency modulation of their envelope and phase. 'Jitter' refers to the resulting temporal variability in the shape of the wavepackets, e.g., their amplitude, phase, wavelength, axial extent, smoothness, etc. This is represented schematically in Figure 3.1.

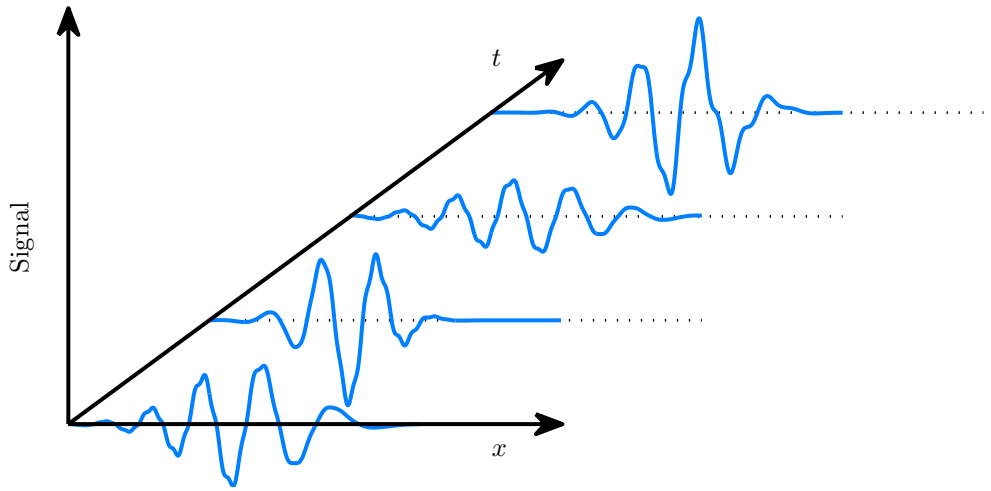


Figure 3.1: Schematic of wavepacket jitter. The wavepackets observed within the jet at different time instances exhibit variability in their spatial form.

The acoustic efficiency of a wavepacket is highly sensitive to these modulations, so flow events that lead to small near-field changes in the wavepacket can give rise to large amplifications in the acoustic field (Cavalieri et al. 2011). Consequently, the average wavepacket does not produce the average sound, a conclusion also reached via statistical analysis of low Reynolds number simulation data (Freund & Colonius 2009). Instead, the coherence decay of the wavepackets must be accounted for to properly capture the observed sound levels (Cavalieri et al. 2011, Kerhervé et al. 2012, Zhang et al. 2014). In other words, the variability in the form of the wavepackets in a jet, i.e., wavepacket jitter, is critically important for sound production.

The physical mechanisms responsible for wavepacket jitter are not well-understood. One possible mechanism – slow-time variation of the turbulent mean flow field – was recently explored by Jordan et al. (2014). The idea, supported by scale separation arguments, was that low frequency variation of the mean flow could lead to low frequency wavepacket intermittency and subsequent acoustic amplification. To explore this idea, two separate approaches were analyzed using LES data of a Mach 0.9 turbulent jet: time-domain linearized Euler equations were solved using an unsteady base flow obtained by low-pass-filtering the LES fields, and frequency-domain solutions were found

using parabolized stability equations and one-way Euler equations with an ensemble of different short-duration averages of the mean flow field as the baseflow $\bar{q}$. The results of this analysis showed that accounting for intermittency in either way increased the acoustic output of the wavepackets by up to 20dB at peak aft angles, but there remained a discrepancy of as much as 20dB compared to the LES (and experimental) acoustic field.

A second possible mechanism for wavepacket jitter is the presence of broadband stochastic inlet perturbations, which could be represented within our modeling framework by stochastic ensembles of the boundary condition $\hat{q}^{BC}_{\omega,m}$. However, this is not a promising option. Since the model remains entirely linear, the statistical effects of any imposed fluctuation (for example setting the amplitude or phase of the inlet disturbances to random values) is simply propagated through the system without meaningfully modifying the wavepackets or their acoustic efficiency.

The goal of the present analysis is to investigate a third mechanism of wavepacket intermittency: nonlinear and stochastic forcing. This effect is bound up in the volumetric forcing term $\hat{f}_{\omega,m}$. The idea is that the nonlinear terms of the Navier-Stokes equations, which are usually neglected in wavepacket models, can act as a stochastic force that perturbs (jitters) the otherwise linearly developing wavepackets, leading to the variability necessary for acoustic amplification. Specifically, we wish to determine the nature of the nonlinear forces responsible for producing acoustically efficient wavepackets. Do they represent deterministic nonlinear interactions amongst large-scale wavepackets (i.e., a direct nonlinear feedback mechanism), or do they take the form of random turbulent interactions?

Our approach is to compute these forces using LES data from a Mach 0.9 turbulent jet. Then, ensembles of the flow and force data are analyzed to educe the actual forcing experienced by wavepackets in this jet, and in particular to distill the forces that are primarily responsible for exciting loud wavepackets.

The remainder of the chapter is organized as follows. Section 3.2 describes the LES database used in this study and describes our method for computing the nonlinear forcing terms and generating ensembles of these data sets. In section 3.3, we introduce two data decomposition techniques, one

of which is novel, that are used to uncover the structure and role of the forces. The results of the investigation are presented and interpreted in section 3.4. Finally, section 3.5 summarizes the main results of the chapter, with special emphasis on their implications for wavepacket modeling.

## 3.2 Flow and force data ensembles

### 3.2.1 LES database

We use data from a high-fidelity large eddy simulation (LES) of an isothermal Mach 0.9 jet issued from a contoured convergent-straight nozzle (Brès et al. 2014). The accuracy of the LES data was verified via extensive comparisons with measurements taken from a companion experiment conducted at the PPRIME Institute, Poitiers (Brès et al. 2015).

The experimental jet was carefully tripped to ensure a fully turbulent boundary layer at the nozzle exit. To replicate this effect, the LES employed localized adaptive mesh refinement, synthetic turbulence, and wall modeling inside the nozzle, which was explicitly included in the computational domain. Figure 3.2 compares the experimental and LES boundary layer velocity profiles at the nozzle exit. The close agreement between the experimental and LES profiles indicates that the boundary layer in the simulation is turbulent at the nozzle exit.

Figure 3.3 compares experimental measurements of the noise spectra on an array of microphones at a constant distance of $50D$ from the nozzle exit to corresponding predictions obtained from the LES using the Ffowcs-Williams & Hawkings (1969) method to project the acoustic field beyond the computational domain. The LES predictions are excellent for $St < 3$. Therefore, the LES database must accurately contain the mechanisms responsible for producing sound at low and moderate frequencies.

For the purpose of analysis, the LES data has been interpolated from the original unstructured LES grid onto a structured cylindrical grid that extends thirty jet diameters in the axial direction and six jet diameters in the radial direction. The grid spacings in both directions are nonuniform and were chosen to approximately correspond to the underlying LES resolution, with a total of

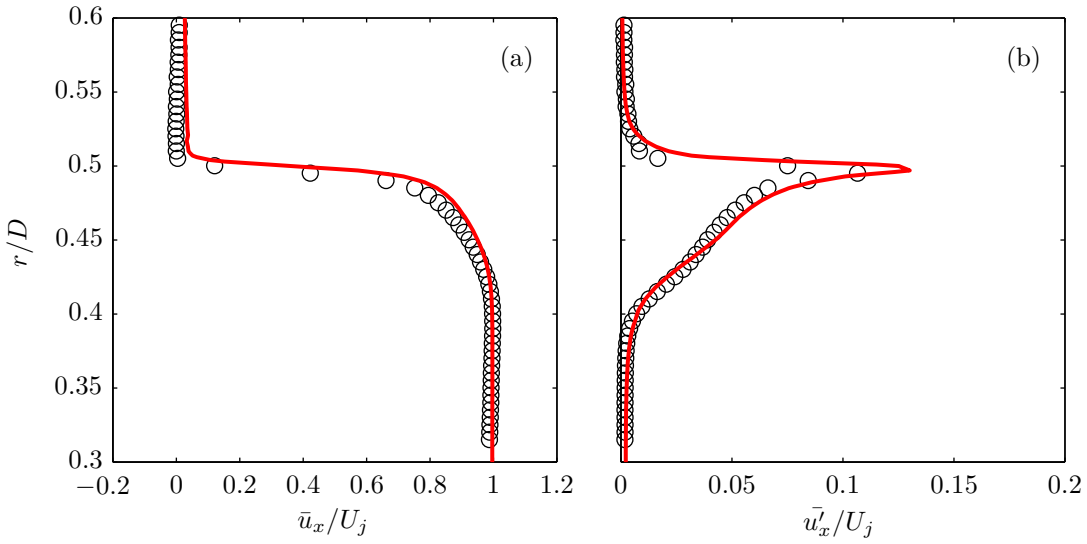


Figure 3.2: Nozzle exit boundary layer axial velocity profiles from experiment ( ○ ) and LES (———): (a) mean and (b) root-mean-square.

656 points in $x$ and 138 points in $r$. The azimuthal grid consists of 128 uniformly spaced angles. The final database consists of time series, sampled at an interval of 0.2 acoustic time units, for the primitive flow variables on this grid.

### 3.2.2 Force computation

The LES approximation of the Navier-Stokes operator is used to compute the nonlinear forcing terms. Recall (from section 1.2.4) that the compressible Navier-Stokes equations can be written conceptually as

$$\frac{\partial q}{\partial t} = \mathcal{F}(q), \tag{3.1}$$

where $q = [q_1, q_2, q_3, q_4, q_5]^T = [\nu, u_x, u_r, u_\theta, p]^T$. Applying the standard Reynolds decomposition $q(x, r, \theta, t) = \bar{q}(x, r) + q'(x, r, \theta, t)$ and isolating terms that are linear in $q'$ leads to an equation of the form

$$\frac{\partial q'}{\partial t} - \mathcal{A}(\bar{q})\, q' = f(x, r, \theta, t), \tag{3.2}$$

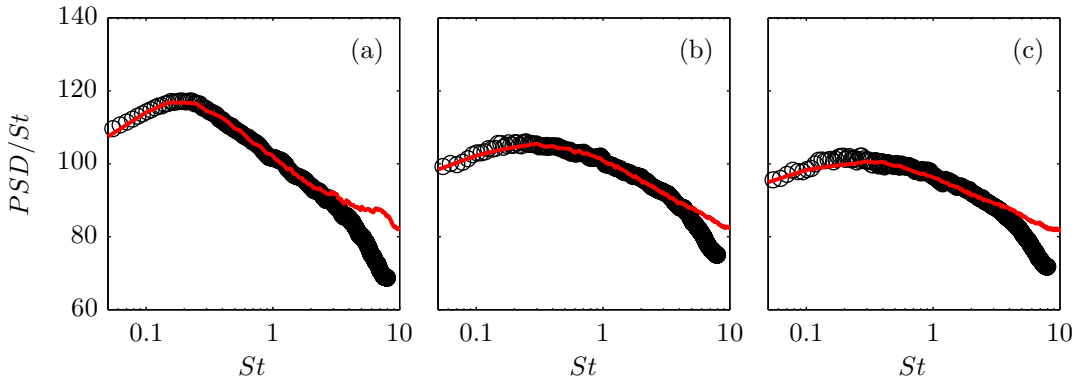


Figure 3.3: Comparison of the noise spectra from experiment ( ○ ) and LES (———) at (a) 150˚, (b) 120˚, and (c) 90˚. The angles are measured from the upstream polar axis.

where

$$\mathcal{A}\left(\bar{q}\right) = \frac{\partial \mathcal{F}}{\partial q}\left(\bar{q}\right) \tag{3.3}$$

and $f$ contains the remaining nonlinear terms. Equations (3.1) - (3.3) are identical to equations (1.7) - (1.10) and are repeated here for convenience to aid the following discussion.

From the equality of equation (3.2), the nonlinear forcing term $f$ can be obtained by computing the two linear left-hand-side terms. The first term can be computed as

$$\frac{\partial q'}{\partial t} = \frac{\partial q}{\partial t} = \mathcal{F}\left(q\right) \tag{3.4}$$

since $\bar{q}$ does not depend on time. The second term can be approximated as

$$\mathcal{A}\left(\bar{q}\right) q' = \frac{\partial \mathcal{F}}{\partial q}\left(\bar{q}\right) q' \approx \frac{\mathcal{F}\left(\bar{q} + \epsilon q'\right) - \mathcal{F}\left(\bar{q}\right)}{\epsilon} \tag{3.5}$$

for some $\epsilon \ll 1$. We take $\epsilon = 10^{-7}$, and note that the results are nearly independent of $\epsilon$ over a range spanning at least four orders of magnitude.

There is an additional subtlety in the practical implementation of this procedure: the actual LES code is written in terms of different variables and therefore a different Navier-Stokes operator. We

represent the LES approximation of the Navier-Stokes equations as

$$\frac{\partial \breve{q}}{\partial t} = \breve{\mathcal{F}}\left(\breve{q}\right), \tag{3.6}$$

where $\breve{q} = \left[\breve{q}_1, \breve{q}_2, \breve{q}_3, \breve{q}_4, \breve{q}_5\right]^T = \left[\rho, \rho u_x, \rho u_y, \rho u_z, p\right]^T$ are the Cartesian, conservative variables used in the LES code and $\breve{\mathcal{F}}$ is the LES operator.

To obtain the desired quantities given by equations (3.4) and (3.5), the remaining task is to write $\mathcal{F}(q)$ in terms of $\breve{\mathcal{F}}(\breve{q})$. The transformation from $\breve{q}$ to $q$ is

$$q = H\left(\breve{q}\right) = \begin{bmatrix} \frac{1}{\breve{q}_1} \\ \frac{\breve{q}_2}{\breve{q}_1} \\ \frac{1}{\breve{q}_1}\left(\breve{q}_3 \cos\theta + \breve{q}_4 \sin\theta\right) \\ \frac{1}{\breve{q}_1}\left(-\breve{q}_3 \sin\theta + \breve{q}_4 \cos\theta\right) \\ (\gamma-1)\breve{q}_5 - \frac{\gamma-1}{2}\frac{1}{\breve{q}_1}\left(\breve{q}_2^2 + \breve{q}_3^2 + \breve{q}_4^2\right) \end{bmatrix} \tag{3.7}$$

and the transformation from $q$ to $\breve{q}$ is

$$\breve{q} = H^{-1}\left(q\right) = \begin{bmatrix} \frac{1}{q_1} \\ \frac{u_2}{q_1} \\ \frac{1}{q_1}\left(q_3 \cos\theta - q_4 \sin\theta\right) \\ \frac{1}{q_1}\left(q_3 \sin\theta + q_4 \cos\theta\right) \\ \frac{1}{\gamma-1}q_5 + \frac{1}{2}\frac{1}{q_1}\left(q_2^2 + q_3^2 + q_4^2\right) \end{bmatrix}. \tag{3.8}$$

The polar angle $\theta$ is measured from the $y$ axis. The relationship between $\mathcal{F}(q)$ and $\breve{\mathcal{F}}(\breve{q})$ can be obtained by inserting equation (3.7) into equation (3.1):

$$\mathcal{F}\left(q\right) = \frac{\partial q}{\partial t} = \frac{\partial}{\partial t}\left(H(\breve{q})\right) = \frac{\partial H}{\partial \breve{q}}\left(\breve{q}\right)\frac{\partial \breve{q}}{\partial t}\left(\breve{q}\right) = \frac{\partial H}{\partial \breve{q}}\left(\breve{q}\right)\breve{F}\left(\breve{q}\right). \tag{3.9}$$

Here, $\breve{q}$ and $q$ are not independent; they are related by equations (3.7) and (3.8). The Jacobian of

$H$ is

$$\frac{\partial H}{\partial \breve{q}}\left(\breve{q}\right) = \begin{bmatrix} -\frac{1}{\breve{q}_1^2} & 0 & 0 & 0 & 0 \\ -\frac{\breve{q}_2}{\breve{q}_1^2} & \frac{1}{\breve{q}_1} & 0 & 0 & 0 \\ -\frac{1}{\breve{q}_1^2}\left(\breve{q}_3\cos\theta + \breve{q}_4\sin\theta\right) & 0 & \frac{1}{\breve{q}_1}\cos\theta & \frac{1}{\breve{q}_1}\sin\theta & 0 \\ -\frac{1}{\breve{q}_1^2}\left(-\breve{q}_3\sin\theta + \breve{q}_4\cos\theta\right) & 0 & -\frac{1}{\breve{q}_1}\sin\theta & \frac{1}{\breve{q}_1}\cos\theta & 0 \\ \frac{\gamma-1}{2}\frac{1}{\breve{q}_1^2}\left(\breve{q}_2^2+\breve{q}_3^2+\breve{q}_4^2\right) & -(\gamma-1)\frac{\breve{q}_2}{\breve{q}_1} & -(\gamma-1)\frac{\breve{q}_3}{\breve{q}_1} & -(\gamma-1)\frac{\breve{q}_4}{\breve{q}_1} & \gamma-1 \end{bmatrix}. \quad (3.10)$$

In an earlier iteration of this study (Towne et al. 2015), we used a different method for computing the forces. Specifically, we constructed a finite difference approximation of $\mathcal{L}_{\omega,m}$ and obtained the time derivative term in the frequency domain by multiplication by $i\omega$. This method yielded similar results to those reported in this chapter, but we have found the method described above to be superior both conceptually and in terms of the signal-to-noise ratio of the forces.

### 3.2.3 Data ensembles

Real jets undergo stochastic excitation. The forcing is organic in the case of experiments, consisting of environmental fluctuations, turbulence inside the nozzle feeding the jet, and so on. In the case of simulations, the forcing is artificially introduced through randomized inlet or nozzle boundary layer fluctuations meant to reproduce realistic turbulence.

This stochastic excitation can be formally represented by adding a zero-mean stochastic forcing term to equation (3.1):

$$\frac{\partial q^{(k)}}{\partial t} = \mathcal{F}\left(q^{(k)}\right) + \eta^{(k)}\left(x,r,\theta,t\right), \quad (3.11)$$

where $\eta^{(k)}$ is the $k$-th realization of the stochastic force and $q^{(k)}$ is the corresponding flow response. Upon applying the Reynolds decomposition and isolating linear terms, the stochastic force is ab-

sorbed into the nonlinear forcing term, giving

$$\frac{\partial q'^{(k)}}{\partial t} - \mathcal{A}\left(\bar{q}\right) q'^{(k)} = f^{(k)}. \tag{3.12}$$

Taking temporal and azimuthal Fourier transforms (see section 1.2.4) leads to an equation of the form

$$\mathcal{L}_{\omega,m} \hat{q}^{(k)}_{\omega,m} = \hat{f}^{(k)}_{\omega,m} \tag{3.13}$$

for each $(\omega, m)$ Fourier-mode pair.

Because of the stochasticity within the large-eddy-simulation, different temporal segments of the flow and force data can be regarded as statistically distinct realizations of the jet. That is, segments of $q'$ and $f$ can be used to represent $q'^{(k)}$ and $f^{(k)}$. These segments are then Fourier transformed to obtain an ensemble of realizations for $\hat{q}^{(k)}_{\omega,m}$ and $\hat{f}^{(k)}_{\omega,m}$.

We use segments containing 256 instantaneous snapshots of the jet, which gives a frequency resolution of $\Delta St = 2\pi\Delta\omega D/U_{jet} = 0.0217$. The time interval of each segment is 56 times longer than the eddy turnover time ($D/U_j$) and 51 times longer than the acoustic time scale ($D/c_\infty$). These segments are long enough that the convection of a wavepacket and the propagation of its emitted sound fits within a single segment. This is important in order to ensure that when we later identify data segments with strong acoustic content, the wavepacket responsible for producing that sound is also contained in the same data segment rather than some other nearby segment. To capture as many of these processes as possible, we overlap the segments by 75%, resulting in 154 segments. With this overlap, each segment is offset by approximately fourteen eddy turnover times, so each segment can be viewed as an independent realizations of the jet, as discussed previously.

We systematically studied the impact of the segment length and overlap percentage to ensure that the final results of our analysis are independent of these parameters. A brief overview of this analysis is given in Appendix A. To summarize, we found that a segment length of at least 256 snapshots should be used to ensure that wavepackets and their associated radiation are contained

in the same block. The overlap percentage was found to have little impact on the most energetic wavepackets (as educed by proper orthogonal decomposition), but increasing the overlap did help converge higher order modes.

## 3.3 Decompositions

In this section we describe two modal decompositions that will be applied to the LES flow and force data in order to educe the nonlinear forces associated with hydrodynamically and acoustically important coherent structures in the jet.

### 3.3.1 Preliminaries

In simulations and models, the partial differential equations above are discretized in space, resulting in a system of ODEs in the time domain and algebraic equations in the frequency domain. For notational simplicity in what follows, we use the same symbols to denote the flow variables and their discrete representation on the grid. For example, $\hat{q}^{(k)}_{\omega,m}$ becomes a vector of the five flow variables at each grid point. The linear operator $\mathcal{L}_{\omega,m}$ is approximated by a matrix $L_{\omega,m}$. The specifics of the discretization are inherited from the LES code. Where it will not cause ambiguity, we also drop the subscripts $(\omega, m)$.

It is helpful to write equation (3.13) as an input-output system:

$$L\hat{q}^{(k)} = B\hat{u}^{(k)}, \tag{3.14a}$$

$$\hat{y}^{(k)} = C\hat{q}^{(k)}, \tag{3.14b}$$

where $\hat{u}^{(k)}$ are inputs, $\hat{y}^{(k)}$ are outputs, and $B$ and $C$ are (not necessarily square) matrices. In linear dynamical systems, $\hat{u}^{(k)}$ represents a control input, such as the voltage to an actuator. In the present context, we interpret $\hat{u}^{(k)}$ as the full nonlinear and stochastic forcing term, $\hat{f}^{(k)}$, and therefore take $B = I$. Thus we allow the forcing to excite each degree of freedom of the system.

We will consider three different choices for the output (i.e., different choices of $C$). The first

is simply $C = I$, meaning the entire flow field over $0 < x/D < 30$, $0 < r/D < 6$ is included in the output. The second, which we label $C = P$, is a constant matrix with zeros in the entries corresponding to all variables except pressure, and at all points in space except a portion of the acoustic field, namely the sub region $0 < x/D < 30$ and $5 < r/D < 6$. The third choice is to set $C = L$, which returns the right-hand-side forcing field as the output, as expanded upon below.

We note that the acoustic field we are considering is not the asymptotic far-field, though the pressure field is entirely propagative at these values of $r$ for all the frequencies considered here, and the directivity is close to that of the far-field. Defining the region comprising the acoustic output as different subsets of the selected region has minimal impact on the presented results.

The ensembles of LES data described in section 3.2.3 provide $N_s = 154$ realizations of the system. Specifically the frequency-azimuthal wavenumber flow and force ensembles represent $N_s$ solutions of equation (3.14a), and the chosen output (flow field, acoustic field, or forcing field) of each is given by equation (3.14b). As is typical in modal analysis, this can be compactly denoted by forming a matrix whose columns represent the different realizations:

$$Q = \left[\hat{q}^{(1)} \quad \hat{q}^{(2)} \quad \dots \quad \hat{q}^{(N_s)}\right], \tag{3.15a}$$

$$F = \left[\hat{f}^{(1)} \quad \hat{f}^{(2)} \quad \dots \quad \hat{f}^{(N_s)}\right], \tag{3.15b}$$

$$Y = \left[\hat{y}^{(1)} \quad \hat{y}^{(2)} \quad \dots \quad \hat{y}^{(N_s)}\right]. \tag{3.15c}$$

Since each realization is a solution, we have

$$LQ = F, \tag{3.16a}$$

$$Y = CQ. \tag{3.16b}$$

### 3.3.2 Linear modes

The modal decompositions we consider construct modes as linear combinations of the data:

$$\tilde{q}^{(j)} = \sum_{k=1}^{N_s} \hat{q}^{(k)} \psi_{kj}, \tag{3.17}$$

which can be written in matrix form as

$$\tilde{Q} = Q\ \Psi, \tag{3.18}$$

where the modes are columns of $\tilde{Q}$, ordered in some natural way. Note that the tilde accent used here is unrelated to its previous use related to PSE in Chapter 2. The goal of each decomposition is to determine the coefficient matrix $\Psi$ that produces modes that optimally satisfy an objective. The coefficient matrix also defines the output and forcing that correspond to each mode:

$$\tilde{F} = F\ \Psi, \tag{3.19a}$$

$$\tilde{Y} = Y\ \Psi. \tag{3.19b}$$

By right-multiplying equation (3.16) by $\Psi$, it is clear that $\tilde{Q}$, $\tilde{F}$, and $\tilde{Y}$ together satisfy the linear system. That is, the modes satisfy the linear equations.

### 3.3.3 Norms

The two modal decomposition techniques described in the following sections are defined in terms of norms of the input and output data. For simplicity, we use in all cases the Euclidean norm

$$\|a\|^2 = a^* a, \tag{3.20}$$

where $a$ represents any input or output vector and the asterisk denotes the conjugate transpose. This approximately represents a volume integral of the input or output quantity, although appropriate

weights are required to make this precise. We found such volume weights to make little difference in the final results and therefore discarded them for simplicity.

The meaning of the norm depends critically on the particular quantity under consideration. For the flow field output $C = I$, the norm is dominated by the velocity terms in the near-field jet, and therefore can be thought of as a kinetic energy integral over the near flow field. For the acoustic output $C = P$, the norm represents the acoustic power summed over the previously described output region. Finally, for the inputs, or equivalently for $C = L$, the norm represents a summation of mass, momentum, and energy sources. The relative scaling of these different components is set by the non-dimentionalization of the LES (which is consistent with that described in section 1.2.1) and results in a roughly equal contribution from each component. This is in line with one of the common choices for the norm of the forcing term within resolvent analysis, which is described shortly.

### 3.3.4 Proper orthogonal decomposition

The most common technique of extracting modes from empirical data is principle component analysis, which within fluid mechanics is usually called proper orthogonal decomposition (POD) (Lumley 1967, Sirovich 1987). POD constructs orthogonal modes from linear combinations of statistically independent data samples that optimally represent the data in terms of energy content (which is equivalent to variance if the mean is subtracted). The first POD mode is a coherent structure that accounts for a maximal portion of the energy of the data, as measured by the norm $\|a\|^2$, and subsequent modes represent smaller and smaller portions of the energy. Therefore, reconstructing the data using POD modes captures the largest possible portion of the total energy using any given number of modes. We will compute POD modes of the output $Y$. This results in $\tilde{Y}$, $\tilde{Q}$ and $\tilde{F}$ modes that are optimal for describing the energy of $Y$. When the output is anything other than the full data-set (a.k.a $C \neq I$) or the norm is singular (a semi-norm), this is sometimes referred to as *extended POD* (Maurel et al. 2001, Borée 2003).

Although the eigenvalue problem that defines the POD modes is well known, it is useful for later comparison to formulate the formal maximization problem that defines the POD expansion

coefficients

$$\Psi_{POD} = \left[\psi_{POD}^{(1)} \quad \psi_{POD}^{(2)} \quad \cdots \quad \psi_{POD}^{(N_s)}\right]. \tag{3.21}$$

The vector $\psi_{POD}^{(j)}$ defines the $j$-th POD mode. These optimal coefficient vectors are the solution of the optimization problem

$$\psi_{POD}^{(j)} = \arg\max_{\|\psi\|=1} \|Y_j\psi\|^2 = \arg\max_{\psi} \frac{\psi^* Y_j^* Y_j \psi}{\psi^*\psi}. \tag{3.22}$$

Here, $Y_0 = Y$ and

$$Y_j = Y - \sum_{s=1}^{j-1} Y\psi_{POD}^{(s)}\kappa_{POD}^{(s)} \tag{3.23}$$

is a modified data matrix in which all content within of range of the first $j-1$ modes has been removed such that it is orthogonal to these modes. The vectors

$$\kappa_{POD}^{(s)} = \left(\psi_{POD}^{(s)}\right)^*, \tag{3.24}$$

are coefficients for reconstructing the data from the modes. The quantity being optimized is the energy of the output, and mode $j$ is constrained to the subspace spanned by $Y_j$. Therefore, the optimization in equation (3.22) finds the most energetic mode that is orthogonal to all previous modes.

To solve the maximization problem, we seek the extremum of the function

$$J = \psi^* Y_j^* Y_j \psi - \lambda\left(\psi^*\psi - 1\right), \tag{3.25}$$

which are obtained when

$$\frac{\partial J}{\partial \psi} = 2\left(Y_j^* Y_j \psi - \lambda\psi\right) = 0. \tag{3.26}$$

We therefore have the eigenvalue problem

$$Y_j^* Y_j \psi_{POD}^{(j)} = \lambda_{POD}^{(j)} \psi_{POD}^{(j)}. \tag{3.27}$$

The global extremum is given by the eigenvector corresponding to the largest eigenvalue. Since the matrix $Y_j^* Y_j$ is Hermitian, its eigenvectors are orthogonal and we can combine the eigenvalue problem for every $k$ into the single eigenvalue problem

$$Y^* Y \Psi_{POD} = \Psi_{POD} \Lambda_{POD}. \tag{3.28}$$

The energy of each mode is given by its eigenvalue $\lambda_{POD}^{(j)}$, which is found within the diagonal matrix $\Lambda_{POD}$. The energy captured by a reduced-order reconstruction of the first $N_{ro}$ modes is found by summing the first $N_{ro}$ eigenvalues.

POD and related techniques have been applied broadly in fluid mechanics and in particular to the flow fields (Arndt et al. 1997, Citriniti & George 2000, Gordeyev & Thomas 2000) and acoustic fields (Freund & Colonius 2009) of jets. The results of these analyses are summarized in a recent review (Jordan & Colonius 2013).

### 3.3.5 Empirical resolvent-mode decomposition

The computation of resolvent modes is a popular method for studying the input/output behavior of fluid dynamical systems (Schmid & Henningson 2001, Jovanović & Bamieh 2005, Sipp et al. 2010, McKeon & Sharma 2010). These modes maximize the gain $\|y\|/\|u\|$ between the input $u$ and output $y$ of the system. For linear time invariant systems such as equation (3.14), these solutions can be obtained at each frequency $\omega$ by computing the singular value decomposition of the transfer function $G(\omega) = CL^{-1}B$. Note that in the present case, $B = I$ and $\hat{u} = \hat{f}$ so the inputs represent the nonlinear and stochastic forcing terms, while the outputs are any linear combination of the flow variables. The singular values give the optimal gains and the right and left singular vectors define corresponding orthonormal inputs and responses, respectively.

Resolvent analysis has been used to study the input/output behavior of a wide range of flows. For example, it has been used to successfully predict the dominant frequencies and mode-shapes in turbulent boundary layers (Sharma & McKeon 2013, Luhar et al. 2014). The approach has also been applied to both supersonic and subsonic jets (Garnaud et al. 2013, Nichols & Jovanović 2014). The preferred frequencies obtained from these analyses are in reasonable agreement with experimentally determined values, and the dominant output modes take the form of wavepackets that are qualitatively similar to those obtained using parabolized stability equations.

A challenge in interpreting the results of these analyses is that it is often unclear whether or not the computed inputs and outputs are physically relevant; it is entirely possible for the optimal output to be excited by inputs that correspond to unphysical mechanisms. For example, a high-gain acoustic response can be excited by inputs that are spatially discontinuous or localized in regions of the jet where little nonlinear forcing is expected, such as the acoustic far-field itself, or by other forms of direct acoustic forcing (Semeraro et al. 2015).

Here, we develop a data-based input/output methodology in which the input and output modes are constrained to lie within the span of the data. The method, which we call empirical resolvent-mode decomposition (ERD), is, to the best of our knowledge, completely novel.

#### 3.3.5.1 Derivation

ERD constructs orthogonal input and output modes from the $Y$ and $F$ data ensembles that maximize gain. The expansion coefficients that define the empirical resolvent modes,

$$\Psi_{ERD} = \begin{bmatrix} \psi_{ERD}^{(1)} & \psi_{ERD}^{(2)} & \cdots & \psi_{ERD}^{(N_s)} \end{bmatrix}, \tag{3.29}$$

are the unique solution of the maximization problem

$$\psi_{ERD}^{(j)} = \arg\max_{\psi} \frac{\|Y_j\psi\|^2}{\|F_j\psi\|^2} = \arg\max_{\psi} \frac{\psi^* Y_j^* Y_j \psi}{\psi^* F_j^* F_j \psi}, \tag{3.30}$$

where

$$Y_j = Y - \sum_{s=1}^{j-1} Y \psi_{ERD}^{(s)} \kappa_{ERD}^{(s)}, \tag{3.31}$$

$$F_j = F - \sum_{s=1}^{j-1} F \psi_{ERD}^{(s)} \kappa_{ERD}^{(s)}, \tag{3.32}$$

and

$$\kappa_{ERD}^{(s)} = \left(\psi_{ERD}^{(s)}\right)^* F^* F. \tag{3.33}$$

The modified data and force matrices have the same meaning as before, and the $\kappa_{ERD}^{(s)}$ vectors are again coefficients for reconstructing the data from the modes. The resulting output and force modes are each orthogonal and maximize the gain between them since the quantity being maximized in equation (3.30) is gain squared.

To solve the maximization problem, we seek the extremum of the function

$$J = \psi^* Y_j^* Y_j \psi - \lambda \left(\psi^* F_j^* F_j \psi - 1\right), \tag{3.34}$$

which is obtained when

$$\frac{\partial J}{\partial \psi} = 2 \left(Y_j^* Y_j \psi - \lambda \psi^* F_j^* F_j \psi\right) = 0. \tag{3.35}$$

We therefore have the generalized eigenvalue problem

$$Y_j^* Y_j \psi_{ERD}^{(j)} = \lambda_{ERD}^{(j)} F_j^* F_j \psi_{ERD}^{(j)} \tag{3.36}$$

for each $j$. The global extremum is given by the eigenvector corresponding to the largest eigenvalue. Since the matrices $Y_j^* Y_j$ and $F_j^* F_j$ are Hermitian, their eigenvectors are orthogonal and we can

combine the eigenvalue problem for every $j$ into the single generalized eigenvalue problem

$$Y^*Y\Psi_{ERD} = F^*F\Psi_{ERD}\Lambda_{ERD}. \tag{3.37}$$

Solving this generalized eigenvalue problem is equivalent to simultaneous diagonalizing $Y^*Y$ and $F^*F$:

$$\Psi_{ERD}^*Y^*Y\Psi_{ERD} = \Lambda_{ERD}, \tag{3.38a}$$

$$\Psi_{ERD}^*F^*F\Psi_{ERD} = I. \tag{3.38b}$$

Therefore, the resulting output and force modes are each orthogonal and maximize the gain between them, which is given by $\sqrt{\lambda_j}$.

#### 3.3.5.2 Computation

$\Psi_{ERD}$ can be computed either by solving the generalized eigenvalue problem in equation (3.37) or by computing two successive standard eigenvalue problems. This second method is computationally preferable and is motivated by equation (3.38). The first step is to compute the eigenvalue decomposition of $F^*F$, which is identical to computing the POD modes of $F$:

$$F^*F\Psi_1 = \Psi_1\Lambda_1. \tag{3.39}$$

Second, the following eigenvalue decomposition is computed:

$$\left(\Lambda_1^{-1/2}\right)^* \Psi_1^*Y^*Y\Psi_1\Lambda_1^{-1/2}\Psi_2 = \Lambda_2\Psi_2. \tag{3.40}$$

Then, $\Lambda_{ERD} = \Lambda_2$ and $\Psi_{ERD} = \Psi_1\Lambda_1^{-1/2}\Psi_2$. The first and second eigenvalue problems ensure the orthogonality of the inputs and outputs, respectively.

#### 3.3.5.3 Relation to other types of modes

In the limit in which $F$ is full-rank, the ERD modes exactly recover those obtained by direct computation of the singular value decomposition of $G(\omega)$, i.e., standard resolvent modes. A full-rank $F$ implies that every degree of freedom of the force input can be independently applied, such that any forcing field can be constructed from linear combinations of the force realizations. When $F$ is not full rank, which will always be the case in application, both the forcing and responses are constrained to lie within the sub-spaces spanned by the data, and ERD finds the modes with optimal gain under this constraint. This ensures that the modes are physical in the sense that they are composed of flow and force events contained within the data sets.

If the different realizations of the forces are uncorrelated, then $F$ is orthogonal and ERD modes are equivalent to POD modes. This can be clearly seen by comparing equation (3.38) to equation (3.28). Therefore, any difference between POD and ERD modes are due to some bias in the forcing, leading to preferential excitation of certain modes.

ERD bears certain similarities with the observer inferred decomposition (OID) (Schlegel et al. 2012), which decomposes a flow into either high-energy or high-gain modes that map linearly to some observable of interest. In the OID framework the notions of high-gain or high-energy modes are associated with the dependent variables only (rather than the nonlinear term of the Navier-Stokes equations), and the notion of linear mapping is based on correlations between the flow modes and the observable. These issues make physical interpretation of OID modes problematic. In contrast, because ERD is formulated in the framework of the system described by equation (3.14), the notions of high-gain or high-energy modes have a firmer physical basis and permit clearer physical interpretation.

ERD is also related to dynamic mode decomposition (DMD) (Schmid 2010) by analogy: DMD constructs an empirical approximation of the *global modes* of equation (3.2) that is constrained by the span of the data, while ERD constructs an empirical approximation of the *resolvent modes* of the same equation, also constrained by the data. Finally, just as DMD is related to Krylov methods for computing unconstrained global modes, the ERD methodology could be used as a Krylov method

for computing unconstrained resolvent modes.

### 3.3.6 Mode notation

In what follows, we use a mnemonic in order to compactly refer to the different modal decompositions using different output mappings. In particular we refer to modes

XXX-Z-#-v,

where XXX refers to the decomposition (POD or ERD), and Z refers to the output quantity determined by $C$, i.e., Z=$I$, $P$, or $L$. When needed, the # refers to the mode number, and v refers to the flow quantity being displayed, i.e., v takes one of the values $u_x, u_r, u_\theta, \nu$ or $p$, when we are plotting states, or one of the values $f_{u_x}, f_{u_r}, f_{u_\theta}, f_\nu$ or $f_p$ when we are plotting the corresponding forcing fields in the streamwise, radial, or azimuthal momentum equations, continuity, and energy equations, respectively.

## 3.4 Results

In this section, we use the POD and ERD data decomposition techniques to educe and interpret the nonlinear and stochastic forcing experienced by wavepackets in the Mach 0.9 jet. We describe the structure of the various modes and attempt to relate them to the underlying dynamics of the near-field turbulence and far-field acoustics.

At this stage of the analysis, we limit our attention to axisymmetric ($m = 0$) solutions of equation (3.13). The axisymmetric mode is important in the aft acoustic field, comprising roughly half of the emitted sound at the peak angles and frequencies of emission. In future work, we will return to the data to examine the results for $m = 1$ and $m = 2$. Furthermore, for the purpose of presentation, we focus on three frequencies that cover much of the range of primary interest: $St = 0.26, 0.52, 0.78$.

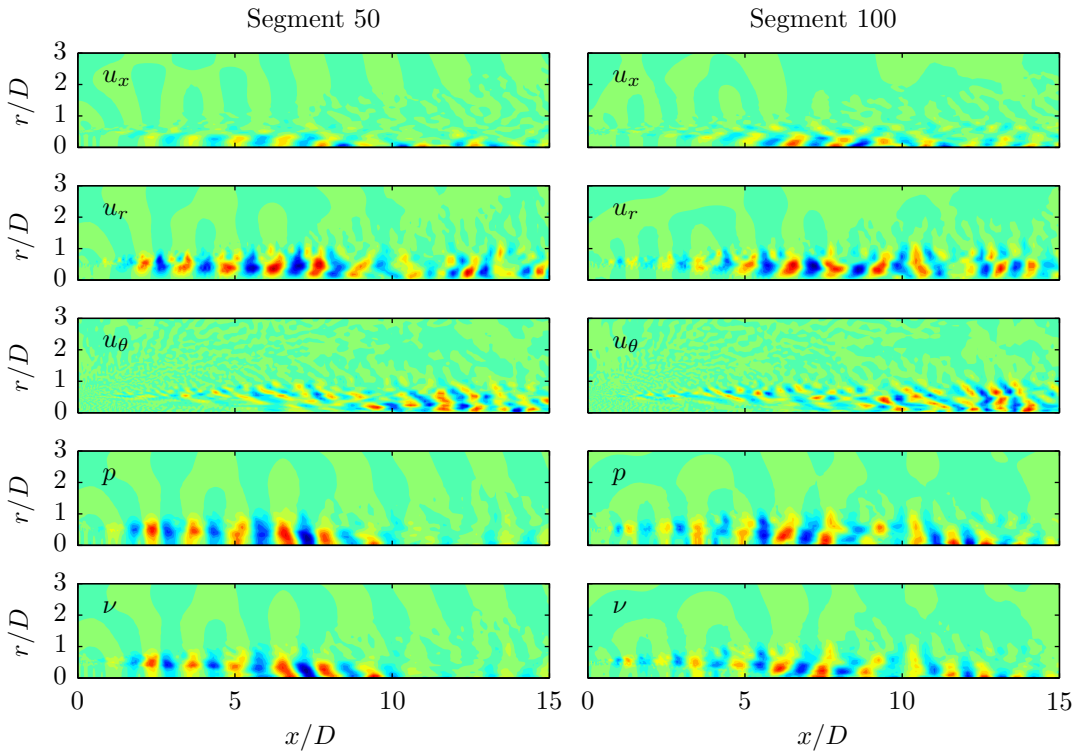


Figure 3.4: Two realizations ($k = 50$ and 100) of the flow field $\hat{q}^{(k)}_{\omega,m}$ at $St = 0.52$ and $m = 0$. The real part of each flow variable is plotted on a linear scale.

### 3.4.1 Flow and force data segments

Before examining the modes from the two decomposition techniques, we show flow and force fields from the Fourier-transformed LES data segments $\hat{q}^{(k)}_{\omega,m}$ and $\hat{f}^{(k)}_{\omega,m}$ in order to introduce some basic properties of these fields.

The flow variables are shown in Figure 3.4 for two realizations of the jet ($k = 50$ and 100) at $St = 0.52$ and $m = 0$. The real part of each variable is plotted on a linear scale, with the maximum value set independently for each subplot. With the exception of the azimuthal velocity, each flow variable clearly contains large-scale coherent wavepackets. Note, however, that the wavepackets are somewhat different in the two different realizations of the jet. This is the essence of jitter, as discussed in section 3.1.

The forces for the same two realizations are shown in Figure 3.5. The magnitude of each force component is plotted on a log scale that spans two orders-of-magnitude. The structure of the

forces is strikingly different from that of the flow field wavepackets themselves. Up until the end of the potential core, the forces are very concentrated in a thin layer starting at the nozzle lip and approximately following a contour of constant mean axial velocity. Since the wavepackets that these modes represent convect with nearly constant phase-speed, lines of constant velocity approximate the location of the critical layer, a location at which the jet has been shown to be sensitive to forcing (Tissolt et al. 2015).

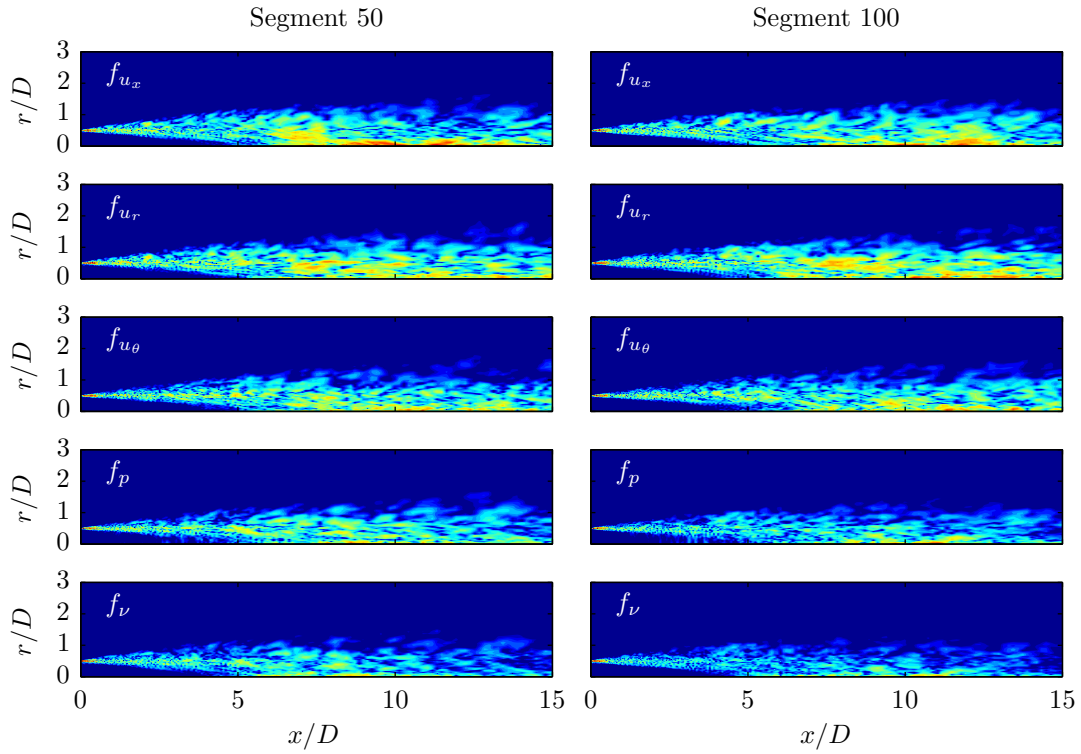


Figure 3.5: Two realizations ($k = 50$ and 100) of the forcing field $\hat{f}^{(k)}_{\omega,m}$ at $St = 0.52$ and $m = 0$. The magnitude of each force component is plotted on a log scale spanning two orders-of-magnitude.

The forces are especially large in the near-nozzle shear-layer. This is shown in Figure 3.6 by repeating Figure 3.5 on a reduced set of axes that magnify the near-nozzle region. This near-nozzle forcing could be related to nonlinear saturation of the Kelvin-Helmholtz instability of the initial shear-layer, which undergoes rapid growth in this region at high frequencies.

Finally, the real part of the forces are plotted on a linear scale on Figure 3.7. Up to the end of the potential core, the forces show minimal coherent phase structure, indicating that they do not propagate with the flow field wavepacket. Unlike the near-nozzle and shear layer forces, those

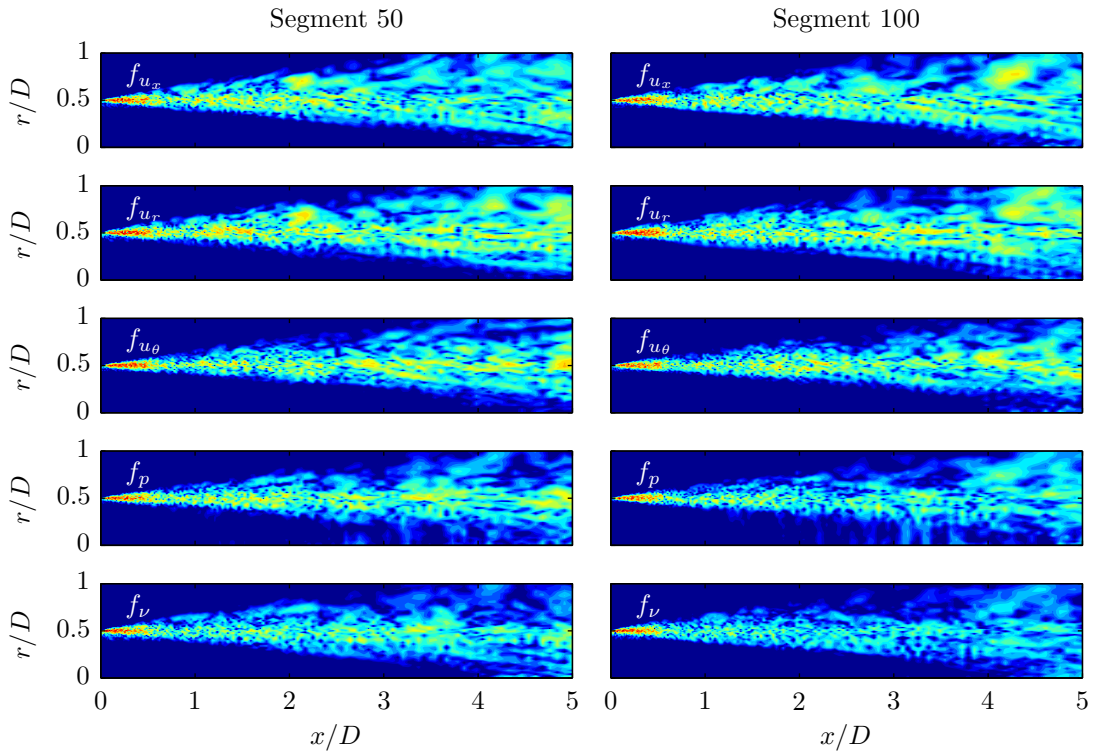


Figure 3.6: Two realizations ($k = 50$ and 100) of the forcing field $\hat{f}^{(k)}_{\omega,m}$ at $St = 0.52$ and $m = 0$. The magnitude of each force component is plotted on a log scale spanning two orders-of-magnitude. Note the reduced span of the axes compared to Figure 3.5, which magnify the near-nozzle region.

beyond the end of the potential core show some phase structure indicative of coherent convection. The form is suggestive of nonlinear interaction between two low frequency structures, possibly due to nonlinear saturation and breakdown of coherent structures that is known to occur in this region of the jet (Hileman et al. 2005). The modal decomposition techniques will be used in the following sections to determine whether or not these coherent nonlinear interactions are dynamically or acoustically significant.

To keep the number of figures within a reasonable limit, we will from here-on-out plot only the pressure and streamwise velocity and the forces in the energy and streamwise momentum equations. From Figure 3.4, it is evident that the specific volume is is nearly identical to the pressure, indicating that the structures are nearly isentropic, and $f_\nu$ is largely representative to $f_p$. Similarly, the radial velocity component is qualitatively similar to the streamwise velocity, while the azimuthal velocity shows limited signs of coherent structures. Likewise, the three momentum forces are all qualitatively

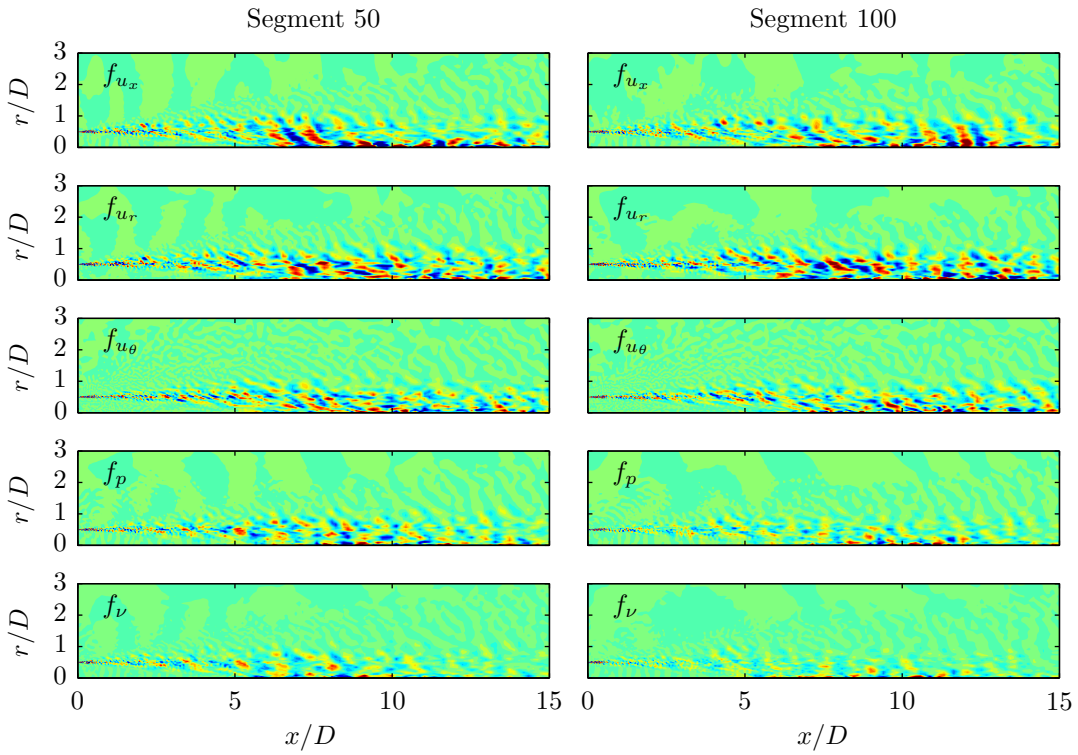


Figure 3.7: Two realizations ($k = 50$ and 100) of the forcing field $\hat{f}^{(k)}_{\omega,m}$ at $St = 0.52$ and $m = 0$. The real part of each force component is plotted on a linear scale.

similar. Except when noted, contour levels are chosen to highlight the spatial structure of the fields; energy amplitudes can be inferred from Figure 3.8, to which we now turn our attention.

### 3.4.2 Modal energies

Figure 3.8 shows cumulative reconstructions of the output for each of the decomposition types and for the three different frequencies at $m = 0$. If the turbulence were completely random, we would expect the energy in each field to accumulate linearly with the number of modes in the reconstruction. Such a linear trend line has been drawn as a guide in each sub-figure.

Recall that POD modes, by definition, represent the maximal portion of the output energy that can be achieved by any reconstruction of that order. This can be observed in Figure 3.8 by noting that the POD-I curve is always highest in the flow field reconstruction (first row), the POD-L curve is always highest in the forcing field reconstruction (second row), and POD-P curve is always highest in the acoustic field reconstruction (third row).

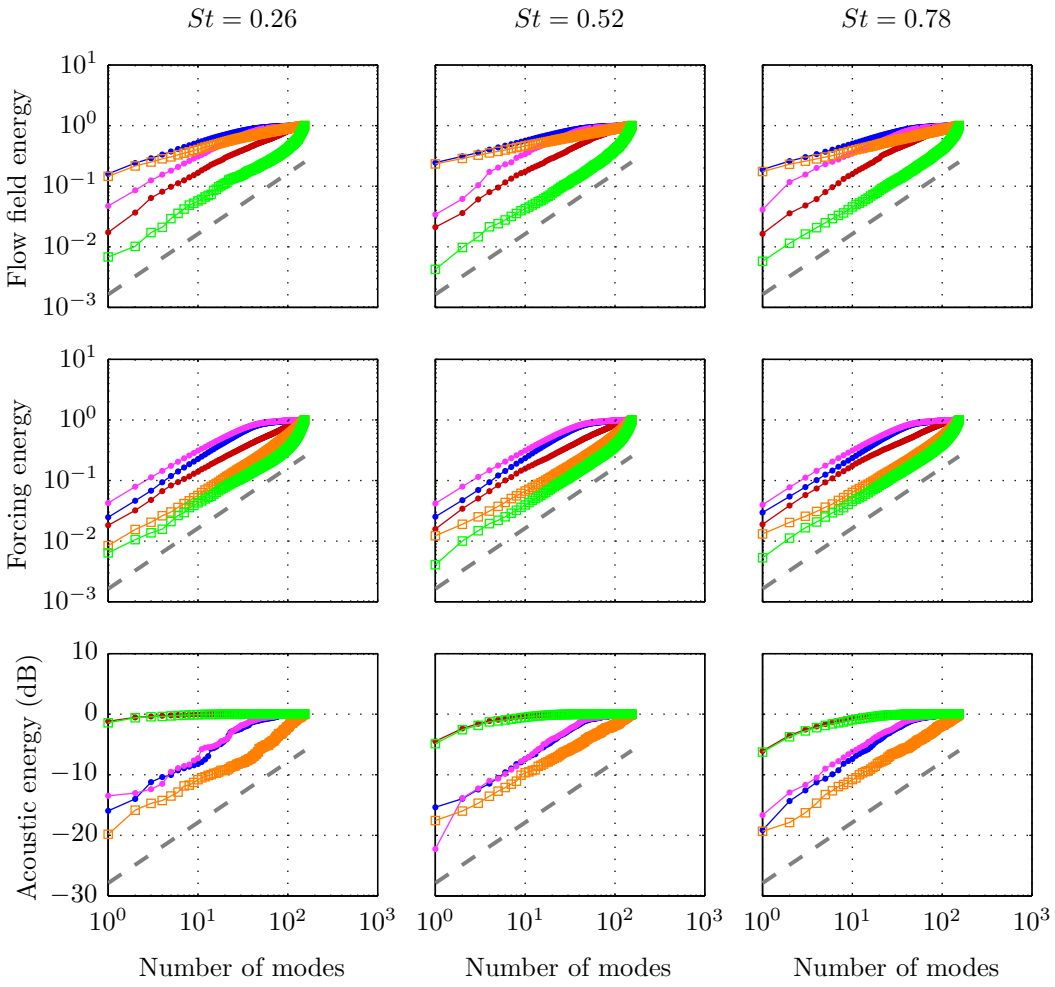


Figure 3.8: Cumulative near-field, forcing, and far-field energy captured by a reduced-order construction of the LES data using a varying number of the following types of modes: ● POD-I; ● POD-P; ● POD-L; □ ERD-I; □ ERD-P. The slope of the gray dashed line represents linear accumulation of energy, indicating an equal division of energy between all modes of a decomposition.

The first few POD-I modes (blue lines with circles) comprise a significant fraction of the total flow energy for each of the three frequencies considered, indicating that coherent structures are energetically significant in the near field of the jet at these frequencies. These modes take the form of wavepackets; their form will be examined in section 3.4.3. Despite the high energy of these structures in the flow field, they comprise (are correlated with) a minuscule amount of the acoustic energy. The near linear slopes of the POD-I acoustic field reconstructions show that these modes are no more effective at capturing the acoustic energy than a random representation of the flow field.

For each frequency, the first three POD-I modes, which cumulatively represent over 30% of the flow field energy, produce an acoustic field that is too quiet by about 15dB.

The first three POD-P modes (red lines with circles) reproduce the acoustic field to within 0.5, 2, and 3 dB for the three frequencies, but represent a vanishing fraction of the flow field energy. These observations are similar to those made in a previous POD analysis of a low Reynolds number jet (Freund & Colonius 2009). The interpretation is that both the near-field and far-field contain very energetic coherent structures, but they are not mutually correlated.

The most energetic POD-L modes make up only a small fraction of the total forcing energy, signifying a lack of energetic coherent structures in the forcing field. The POD-L modes are extremely inefficient at describing the energetic structures in the acoustic field. This indicates that the coherent structures that do exist in the forcing field are not responsible for exciting the coherent structures in the acoustic field. In particular, they are no more effective at exciting acoustic radiation than random forces, since the POD-L reconstruction linearly accumulates energy in the acoustic field. Conversely, the POD-P modes are inefficient at describing the forcing field.

Similarly, the POD-L modes are inefficient at describing the flow field and the POD-I modes are efficient at describing the forcing field, but the inefficiencies here are much less extreme than they are for the acoustic field. We'll see later that the forces associated with the flow field modes are more structured than those associated with the acoustic field modes.

The ERD-I modes are nearly as efficient at reconstructing the flow field as the POD-I modes (compare orange and blue curves). Similarly, the ERD-P modes are nearly as efficient in reconstructing the acoustic field as the POD-P modes (compare red and green curves). However, the ERD-I and ERD-P forces are significantly less energetic than the POD-I and POD-P forces. In other words, ERD is able to isolate forces that are efficient at exciting a strong response in the flow or acoustic field. While POD seeks contributions from any flow event that produces a coherent response, ERD rejects inefficient contributions that that only slightly increase the energy of the response but significantly add to the energy of the force. The fact that ERD is able to accomplish this indicates that some parts of forcing field are more important than others for exciting the flow and acoustic fields.

In the following sections we will examine the spatial structure of each of the mode types with the goal of relating the preceding observations to the underlying dynamics of the near-field turbulence and far-field acoustics.

### 3.4.3 Energetic flow field modes

The pressure and streamwise velocity of the first, second, and fortieth modes for $St = 0.24$ and $St = 0.52$ are depicted in Figures 3.9 and 3.10. The first two modes exhibit clear wavepacket structure within both fields and for both frequencies. By contrast, the fortieth mode exhibits little spatial structure and presumably captures low energy turbulent behavior.

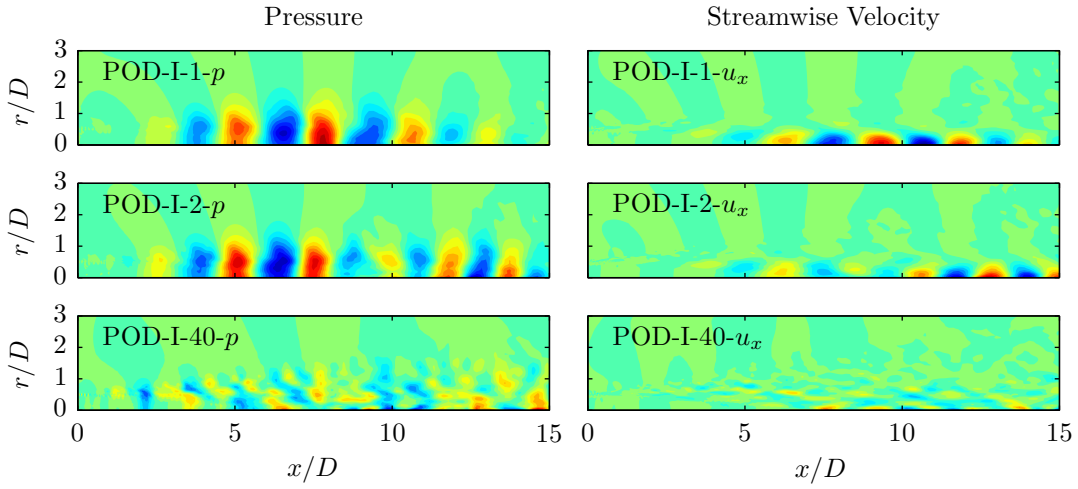


Figure 3.9: Pressure and streamwise velocity contours for POD-I modes 1, 2, and 40 at $St = 0.26$. The first two modes comprise 24% of the total flow energy and take the form of large-scale coherent wavepackets.

As discussed earlier, linear models that are forced exclusively at the jet inlet provide a reasonable representation of the most energetic near field wavepackets, namely the POD-I-1 modes. To illustrate this, Figure 3.11 compares the pressure and axial velocity of the POD-I-1 modes at $St = 0.26$ and $St = 0.78$ with predictions obtained by forcing the one-way Euler equations with a local Kelvin-Helmholtz eigenfunction at $x/D = 0.5$. The scaling of the linear one-way Euler solutions is arbitrary and has been set so that the pressure at $(x/D, r/D) = (7, 0)$ matches the corresponding POD-I-1-p value. The overall match is good at both frequencies, although non-trivial differences can be observed

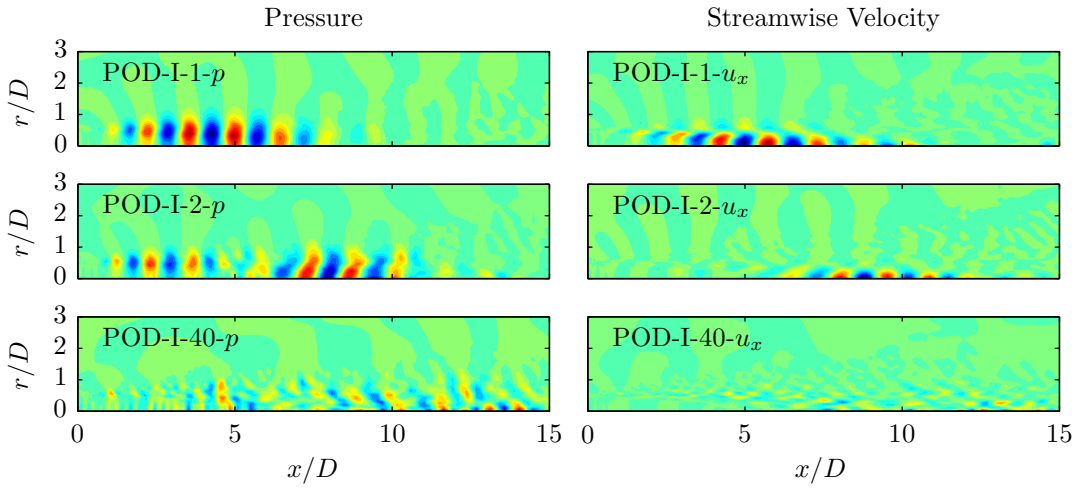


Figure 3.10: Pressure and streamwise velocity contours for POD-I modes 1, 2, and 40 at $St = 0.52$. The first two modes comprise 31% of the total flow energy and take the form of large-scale coherent wavepackets.

at $St = 0.26$, particularly for the streamwise velocity. Degradation of linear model predictions at low frequencies have been reported by Gudmundsson & Colonius (2011), among others. Since linear models essentially capture the POD-I-1 modes, their low acoustic efficiency is associated with and explained by the low acoustic efficiency of these modes.

The $f_p$ and $f_{u_x}$ components of the forces associated with the POD-I modes at $St = 0.26$ and $St = 0.52$ are shown in Figures 3.12 and 3.13. They are plotted on both a logarithmic scale and a linear scale to highlight different aspects of their character.

The forces related to these modes are quite similar to those observed for the individual flow and force realizations of the jet shown in section 3.4.1, especially up to the end of the potential core. In particular, they show minimal coherent phase structure in this region, indicating that they do not propagate with the flow field wavepacket. Moreover, the forces associated with coherent flow structures (modes 1 and 2) are similar to those associated with the unstructured turbulence (mode 40) in this region, indicating that the same forcing mechanisms are associated with both.

As was the case for the individual realizations, the forces beyond the end of the potential core show some phase structure indicative of coherent convection. The form is suggestive of nonlinear interaction between two low frequency structures, possibly due to nonlinear saturation and break-

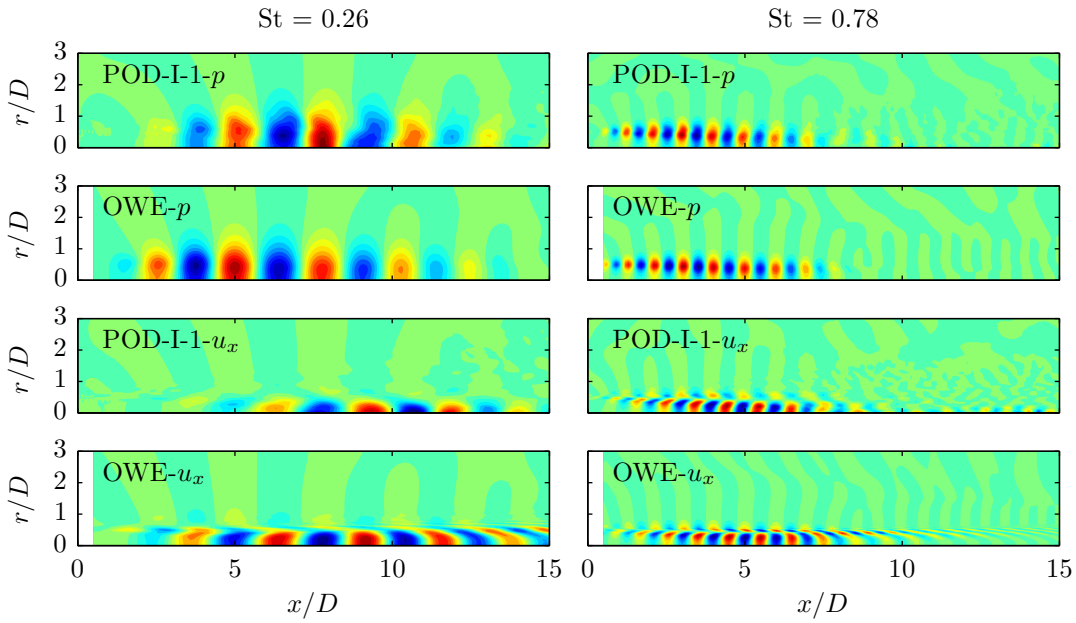


Figure 3.11: Comparison between POD-I-1 modes and a linear model with inlet forcing, computed using one-way Euler equations, at $St = 0.24$ and $St = 0.78$.

down of coherent structures. Their presence here does not indicate a connection to sound generation, however, since the POD-I modes have very little acoustic energy.

It's unlikely that these semi-structured forces play a significant role in physically generating the coherent flow field wavepackets. These wavepackets convect downstream, making their development insensitive to downstream conditions. Instead, a more physically reasonable interpretation is that wavepackets develop almost linearly beginning in the near-nozzle region up to the close of the potential core, at which point they break down nonlinearly. This interpretation is bolstered by the fact that models forced exclusively at the inlet produce good approximations of these structures.

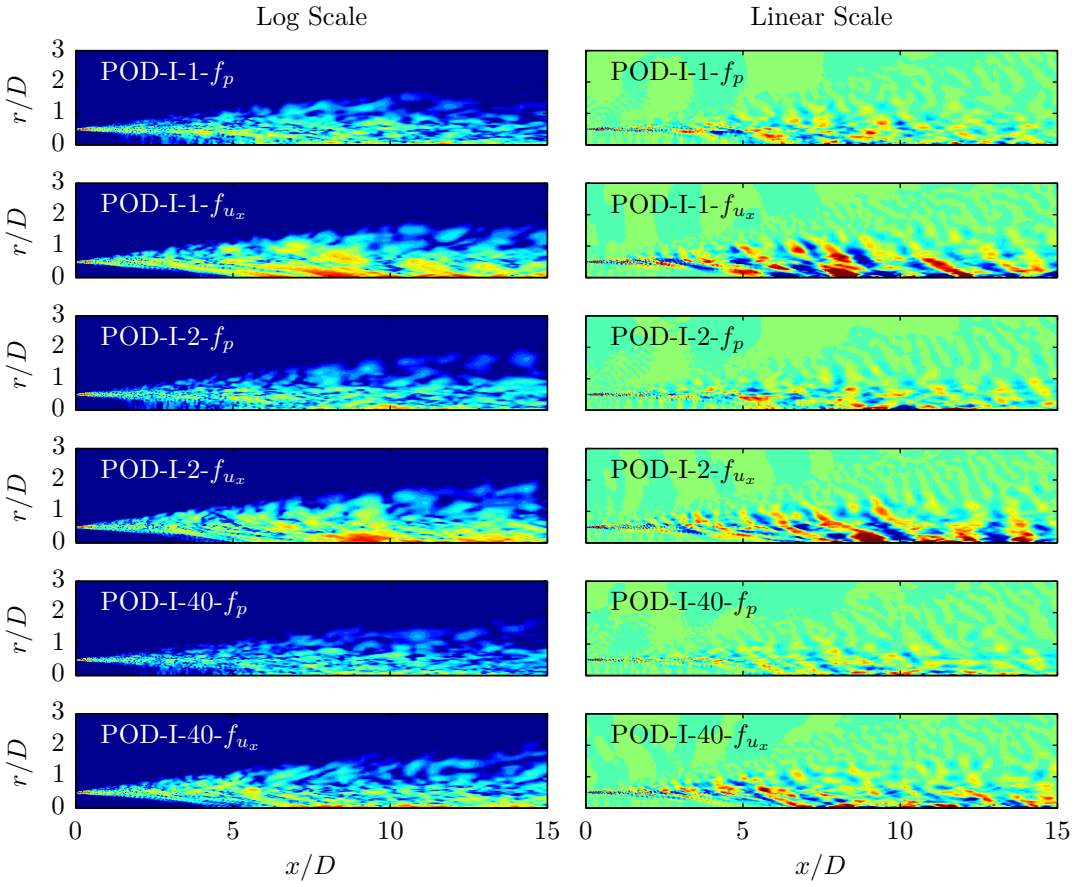


Figure 3.12: Energy and streamwise momentum equation force contours for POD-I modes 1, 2, and 40 at $St = 0.26$. The first and second columns use logarithmic and linear scales, respectively.

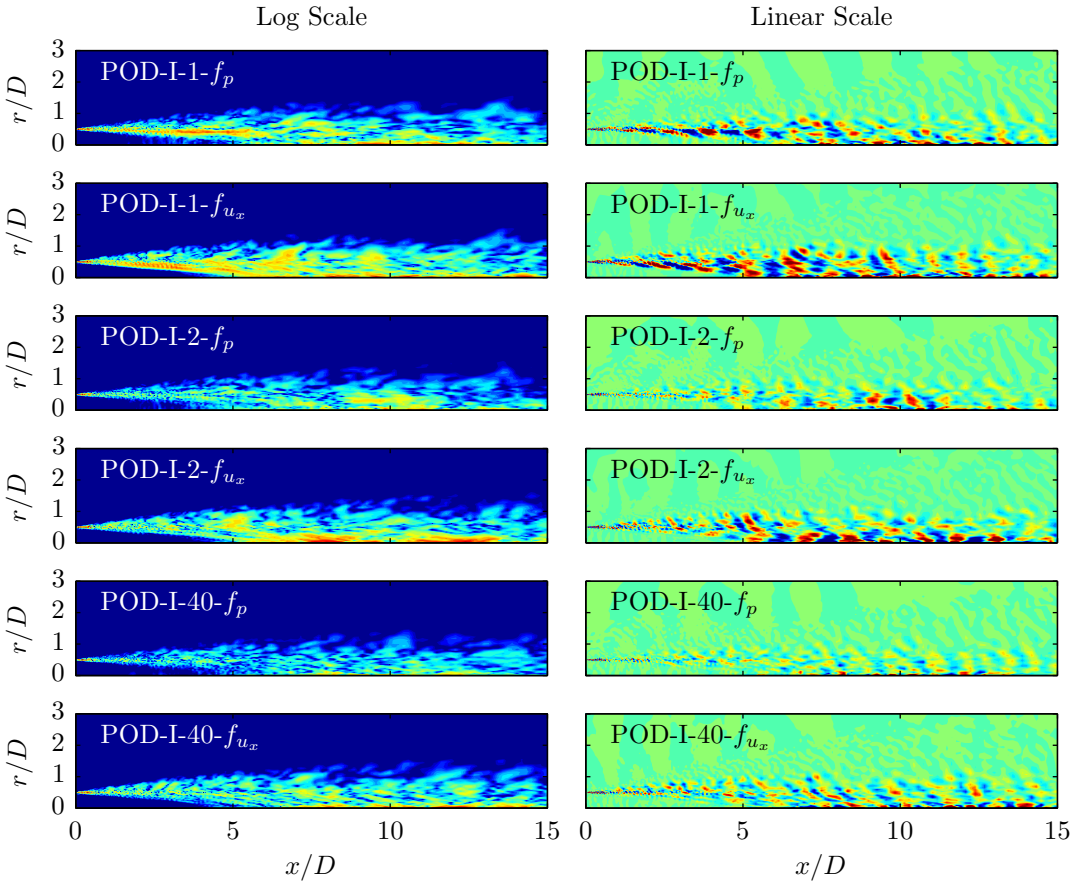


Figure 3.13: Energy and streamwise momentum equation force contours for POD-I modes 1, 2, and 40 at $St = 0.52$. The first and second columns use logarithmic and linear scales, respectively.

### 3.4.4 Energetic acoustic field modes

Figures 3.14 and 3.15 show the pressure component of the first, second, and fortieth POD-P modes at $St = 0.26$ and $St = 0.52$. The first and second columns use contour levels that highlight the flow field and acoustic field wavepackets, respectively. These modes optimally represent the energy of the acoustic field. Both frequencies show similar characteristics. In the first mode, a single, highly directive beam of acoustic radiation emanates from near the close of the potential core, accounting for over half of the radiated acoustic energy of the jet. The near flow field takes the form of a distorted (jittered) wavepacket. Especially at the lower frequency, the wavepacket is significantly shorter than the corresponding POD-I wavepacket.

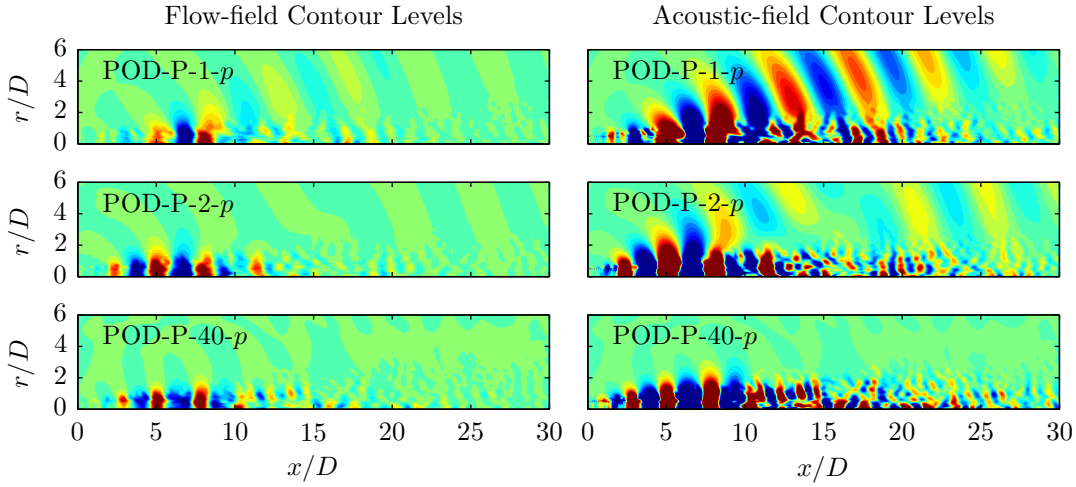


Figure 3.14: Pressure for POD-P modes 1, 2, and 40 at $St = 0.26$. The left and right columns use contour levels selected to highlight the flow field and acoustic field wavepackets, respectively. The first two modes represent the acoustic field to within 0.5 dB.

The corresponding energy and streamwise momentum equation forces are shown in Figures 3.16 and 3.17. They follow the same general trends as the POD-I forces, again reflecting a lack of coherence up to the end of the potential core. There is again some evidence of nonlinear wavepacket interaction further downstream, but these structures are less energetic than they were for the POD-I modes. This is visually apparent, but also confirmed by the energy reconstructions in Figure 3.8. More importantly, no new features that could be regarded as sound source mechanism appear in the POD-P forcing fields that do not exist in the POD-I forcing fields. Furthermore, the mode 1 and

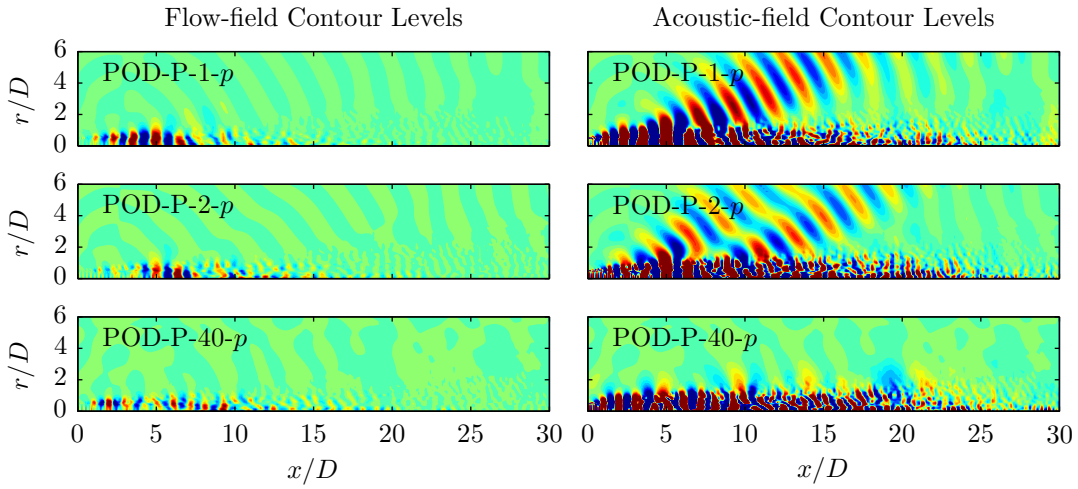


Figure 3.15: Pressure for POD-P modes 1, 2, and 40 at $St = 0.52$. The left and right columns use contour levels selected to highlight the flow field and acoustic field wavepackets, respectively. The first two modes represent the acoustic field to within 2.3 dB.

2 forcing fields are nearly identical to the mode 40 forcing fields, indicating that there is little that distinguishes forces that generate loud wavepackets from those that generate quiet ones.

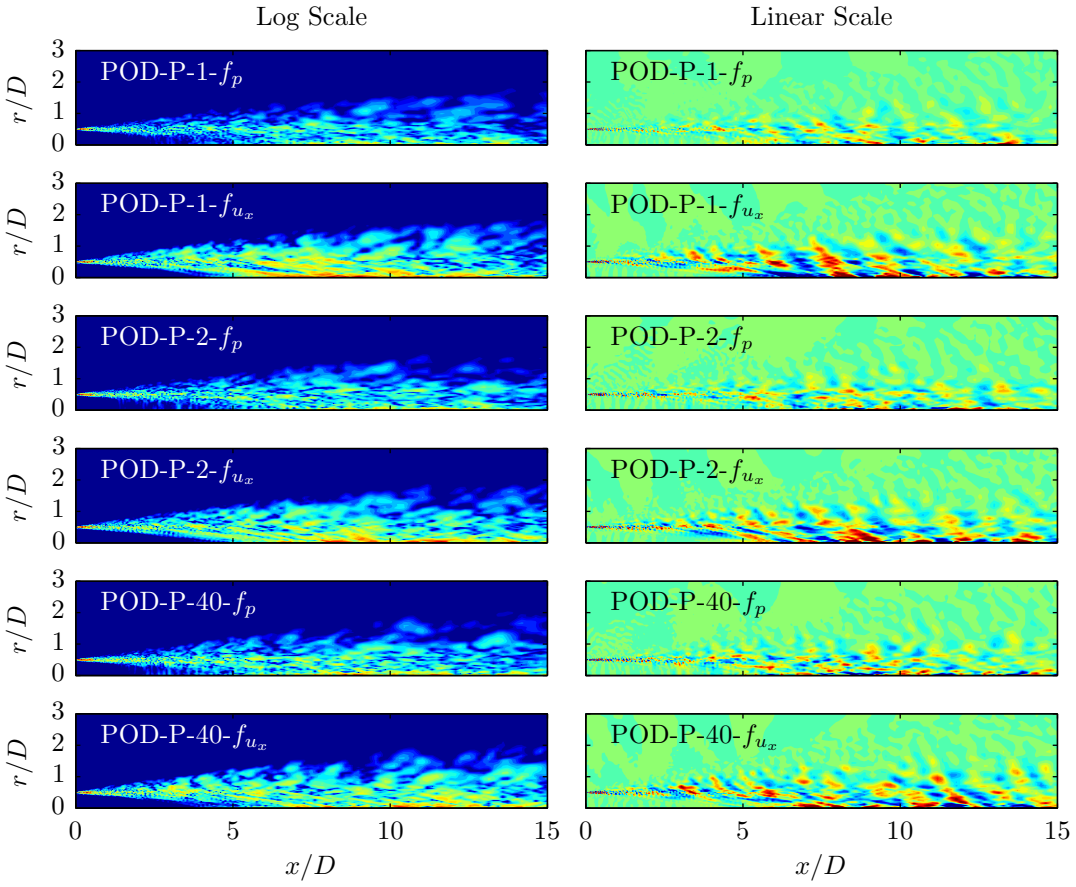


Figure 3.16: Energy and streamwise momentum equation force contours for POD-P modes 1, 2, and 40 at $St = 0.26$. The first and second columns use logarithmic and linear scales, respectively.

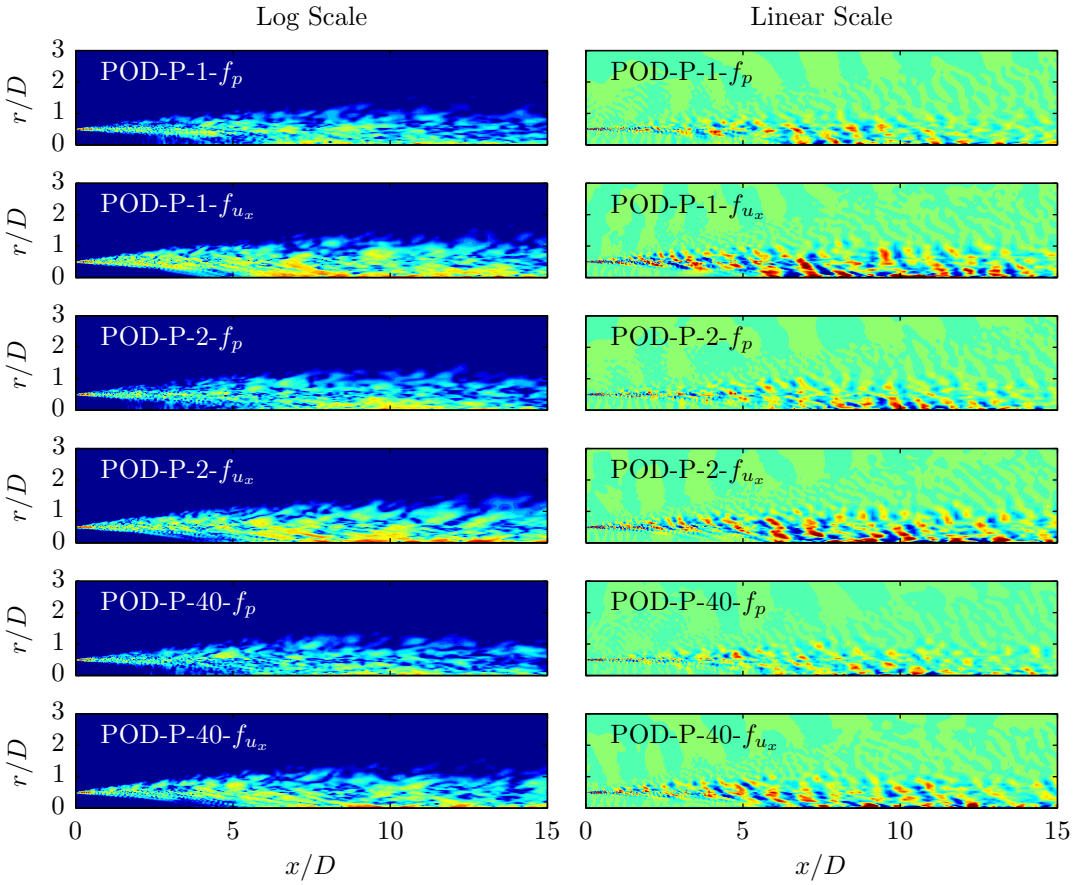


Figure 3.17: Energy and streamwise momentum equation force contours for POD-P modes 1, 2, and 40 at $St = 0.52$. The first and second columns use logarithmic and linear scales, respectively.

### 3.4.5 Energetic forcing modes

We next survey the POD-L modes, which represent the most energetic structures in the forcing field and the flow and acoustic field responses they excite. Figures 3.18 and 3.19 depict the energy and streamwise momentum equation forces for the first, second, and fortieth POD-L modes at $St = 0.26$ and $St = 0.52$, respectively.

The first and second modes show obvious wavepacket structure. Recall, however, that these structures make up a small fraction of the total forcing field energy. In fact, for both frequencies, they are only slightly more energetic than the fortieth mode, which exhibits little-to-no structure.

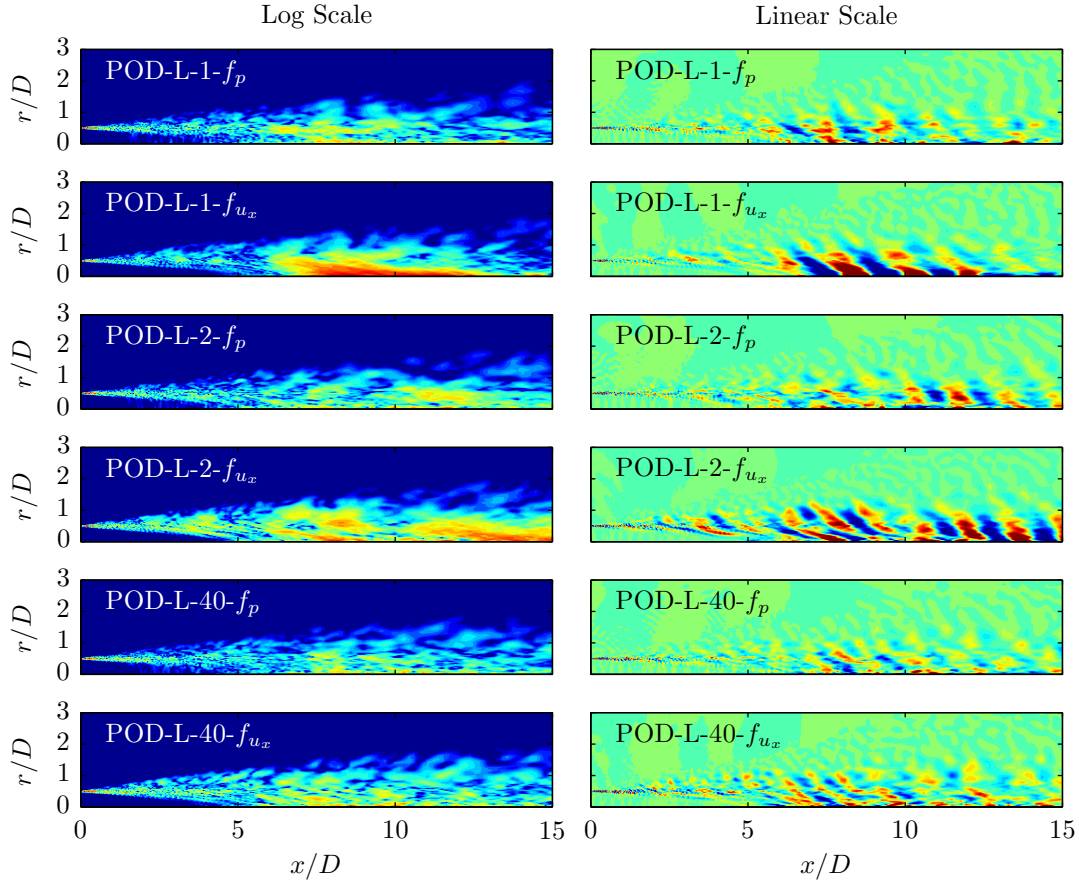


Figure 3.18: Energy and streamwise momentum equation force contours for POD-L modes 1, 2, and 40 at $St = 0.26$. The first and second columns use logarithmic and linear scales, respectively.

The response excited by these forces are displayed in Figures 3.20 and 3.21. Specifically, the pressure is plotted using the same two sets of contour levels from Figures 3.14 and 3.15 so that the

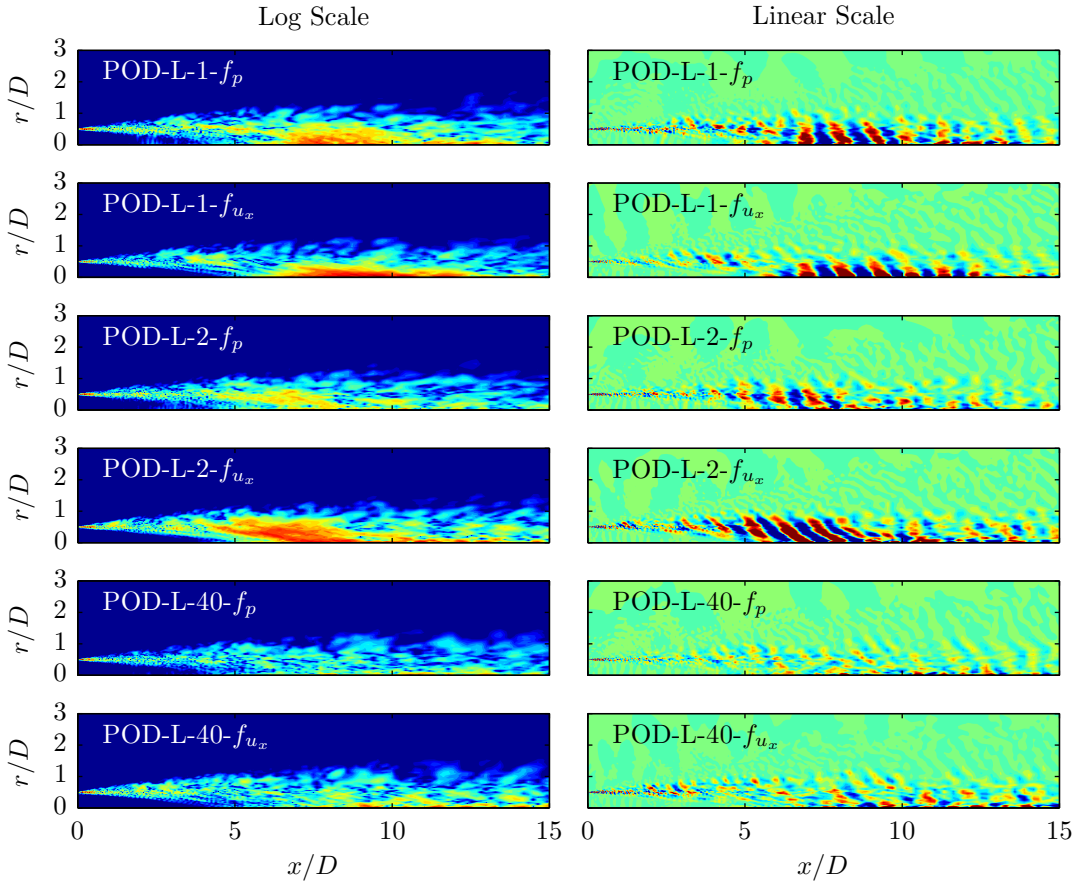


Figure 3.19: Energy and streamwise momentum equation force contours for POD-L modes 1, 2, and 40 at $St = 0.52$. The first and second columns use logarithmic and linear scales, respectively.

fields can be directly compared. It is clear that the high-energy, structured forces produce very little sound, a conclusion we also ascertained from the energy reconstructions in Figure 3.8. Especially for the higher frequency, the unstructured forces in the fortieth mode are *more* effective at exciting acoustic radiation. To reiterate, the limited structure that does exist within the forcing field is unrelated to acoustic emissions. On the other hand, the POD-L modes are reasonably energetic in the flow field, as discussed in section 3.4.2.

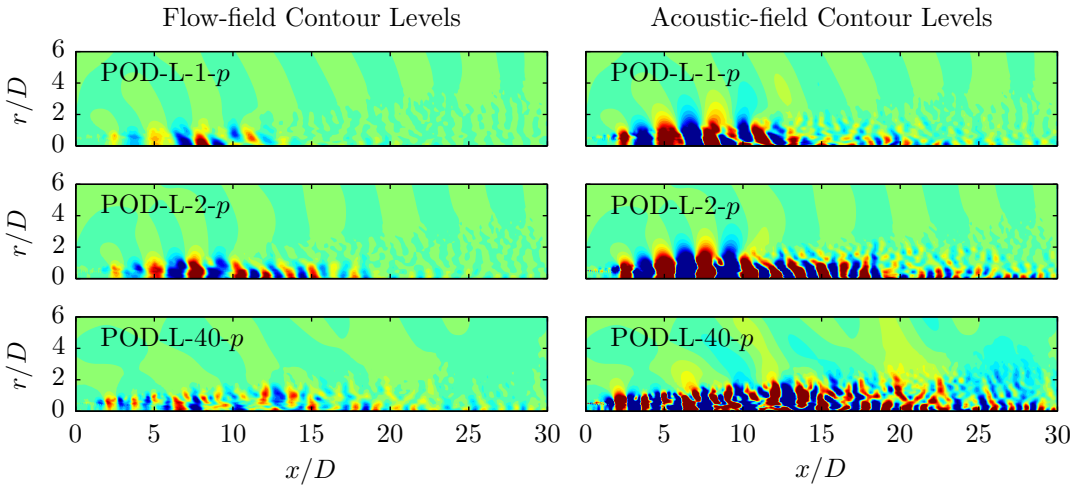


Figure 3.20: Pressure for POD-L modes 1, 2, and 40 at $St = 0.26$. The left and right columns use contour levels selected to match Figure 3.14.

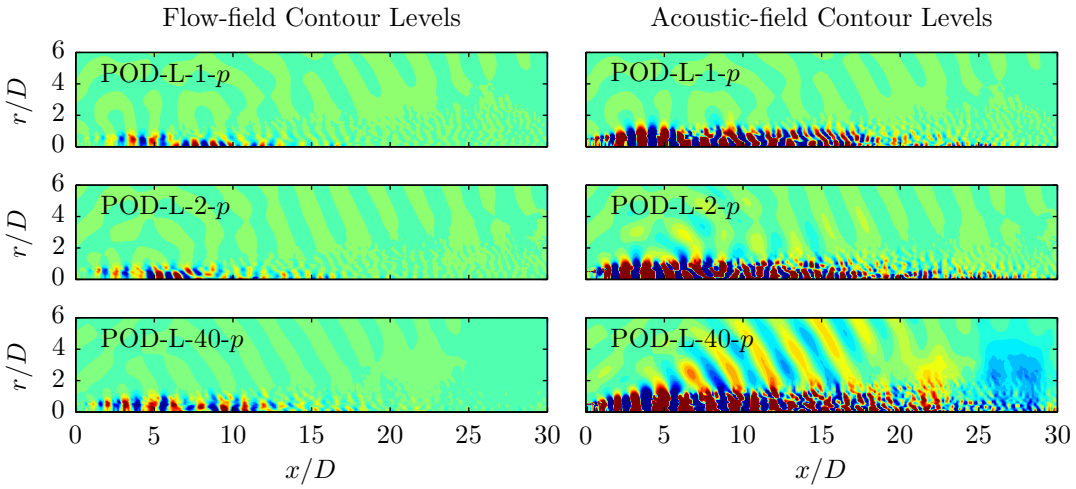


Figure 3.21: Pressure for POD-L modes 1, 2, and 40 at $St = 0.52$. The left and right columns use contour levels selected to match Figure 3.15.

### 3.4.6 High flow-field-gain modes

We next consider the ERD-I modes, which maximize the gain between the forcing and flow fields. The gain for each mode at $St = 0.26$, 0.52, and 0.78 in shown in Figure 3.22(a), while the maximum gain as a function of frequency is shown in Figure 3.22(b).

We saw previously that the ERD-I modes are nearly as efficient as the POD-I modes at representing the flow field energy. This implies that the first few ERD-I modes ought to be similar to the first few POD-I modes. Figures 3.23 and 3.24 compare the pressure fields of the first, second, and

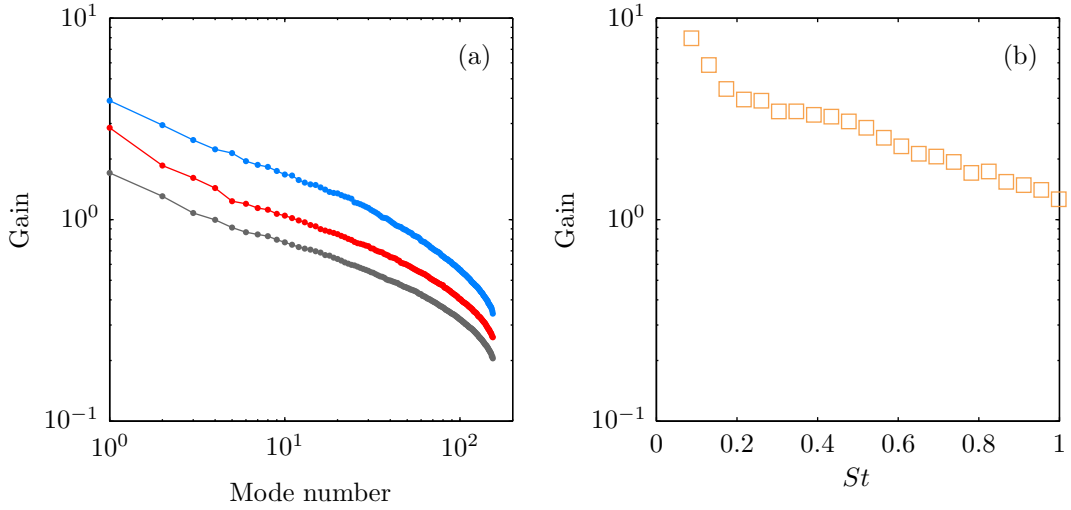


Figure 3.22: Flow field gains: (a) gain as a function of mode number for $St = 0.26$ ( ● ) , $St = 0.52$ ( ● ), and $St = 0.78$ ( ● ); and (b) maximum gain as a function of frequency.

fortieth ERD-I modes to the corresponding POD-I modes for $St = 0.26$ and $St = 0.52$. The close correspondence of the first two modes highlights the near-equivalence of high energy and high gain modes in the flow field response. The match is even better at higher frequencies.

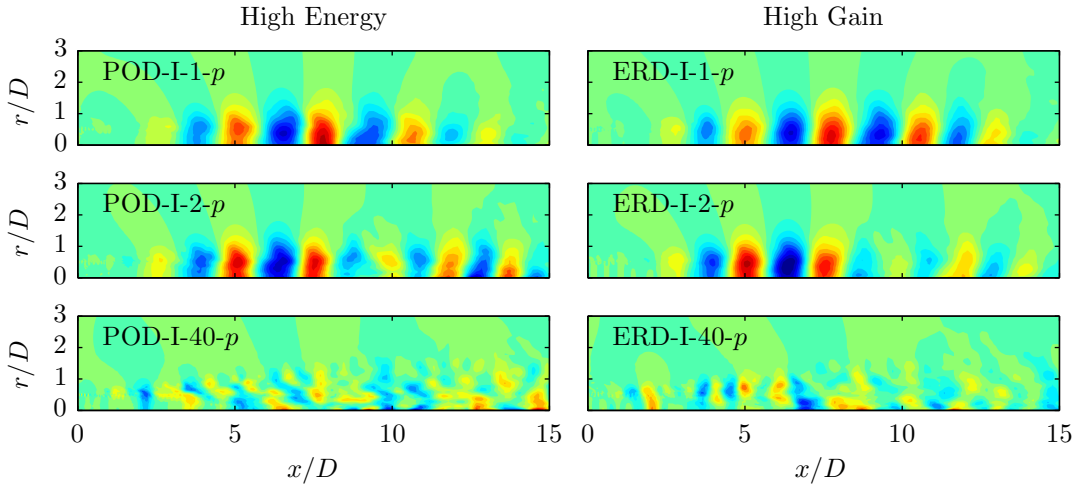


Figure 3.23: Pressure for POD-I and ERD-I modes 1, 2, and 40 at $St = 0.26$. The flow fields of the first two high gain modes are nearly the same as those of the first two high energy modes both in terms of energy form.

However, the forcing fields associated with these modes, which are represented by their streamwise momentum equation components in Figures 3.25 and 3.26, are significantly different in terms of their energy; from Figure 3.8, the ERD-I forces are, on average, about half as energetic as the POD-I

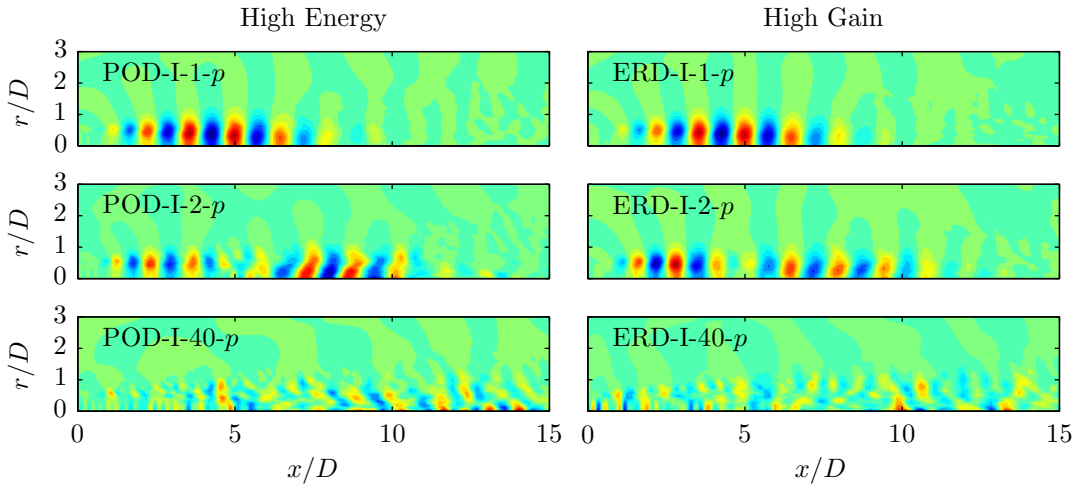


Figure 3.24: Pressure for POD-I and ERD-I modes 1, 2, and 40 at $St = 0.52$. The flow fields of the first two high gain modes are nearly the same as those of the first two high energy modes both in terms of energy form.

forces. Specifically, ERD identifies the forces that maximize gain rather than energy, thus effectively filtering out impotent forces. Although it is not abundantly clear precisely which part of the force is removed, the ERD-I forces seem to display fewer signs of nonlinear wavepacket interactions. Also, the differences between the first two modes and fortieth mode are less noticeable for the ERD-I forces than for the POD-I forces, suggesting that high-gain forces are not all that different from low gain ones. In other words, as we already argued in section 3.4.3, the structured part of the POD-I forces are unimportant and mostly unrelated to the dynamics of the flow field wavepackets.

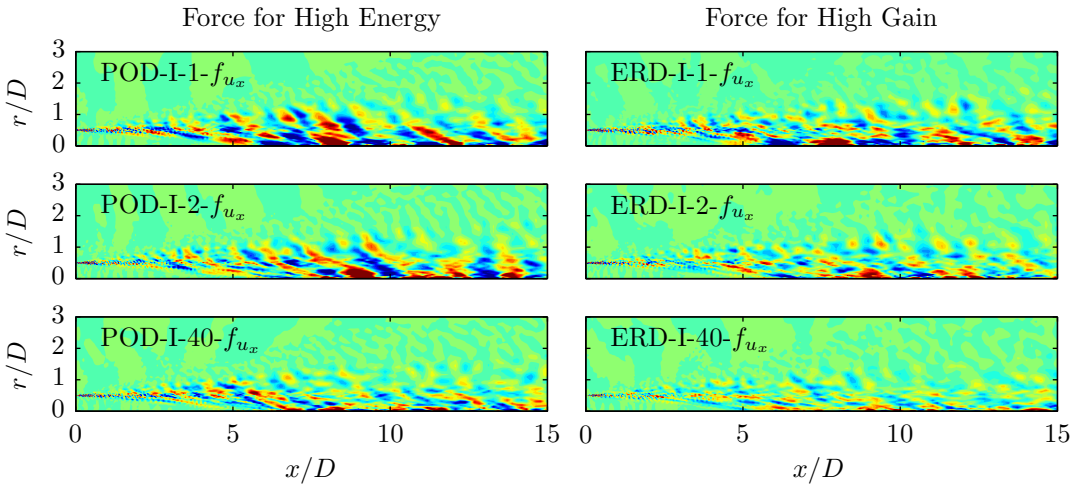


Figure 3.25: Streamwise momentum force for POD-I and ERD-I modes 1, 2, and 40 at $St = 0.26$. The high gain forces show less evidence of nonlinear wavepacket interaction.

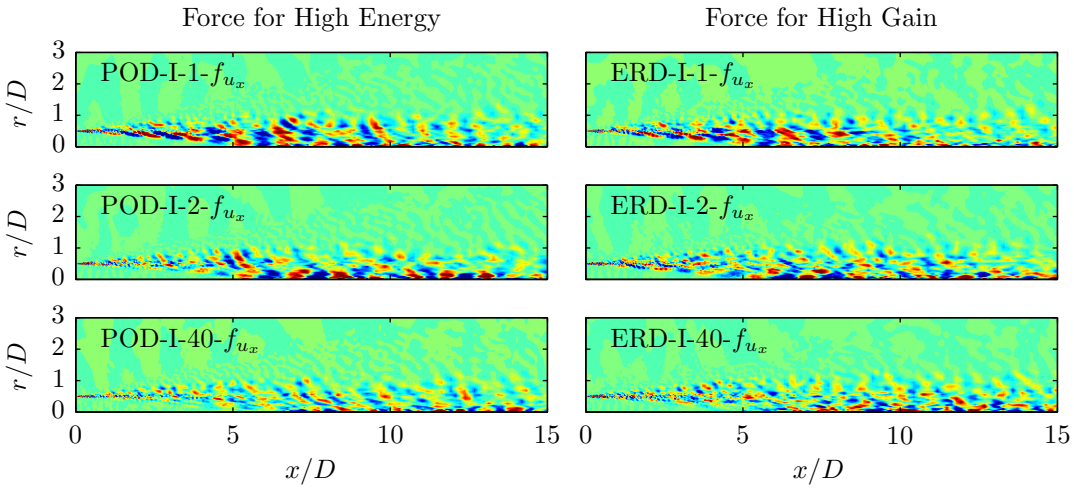


Figure 3.26: Streamwise momentum force for POD-I and ERD-I modes 1, 2, and 40 at $St = 0.52$. The high gain forces show less evidence of nonlinear wavepacket interaction.

### 3.4.7 High acoustic-gain modes

Finally, we examine the ERD-P modes, which maximize the gain between the forcing field and the acoustic field. The gain for each mode at $St = 0.26$, 0.52, and 0.78 in shown in Figure 3.22(a). The gains fall off quickly, so the ERD-I modes provide a low-rank representation of the flow field. The maximum gain as a function of frequency is shown in Figure 3.22(b). A peak in the maximum gain is observed at $St = 0.2$, which has been identified as the peak radiation frequency at aft-angles Jordan & Colonius (2013).

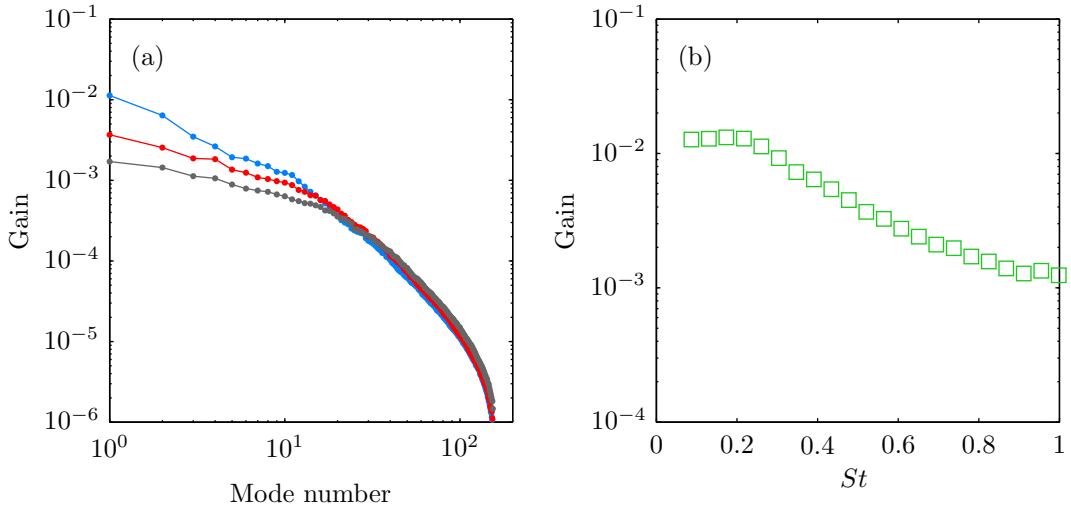


Figure 3.27: Acoustic field gains: (a) gain as a function of mode number for $St = 0.26$ ( ● ) , $St = 0.52$ ( ● ), and $St = 0.78$ ( ● ); and (b) maximum gain as a function of frequency.

The first few EDR-P modes make an almost identical contribution to the acoustic field energy as the POD-P modes. Accordingly, the acoustic fields of these modes should be very similar. Figures 3.28 - 3.30 compare the pressure components of the first, second, and fortieth POD-P and ERD-P modes at $St = 0.26$, $St = 0.52$, and $St = 0.78$, respectively. These figures confirm the similarity of the POD-P and ERD-P acoustic fields for the leading modes.

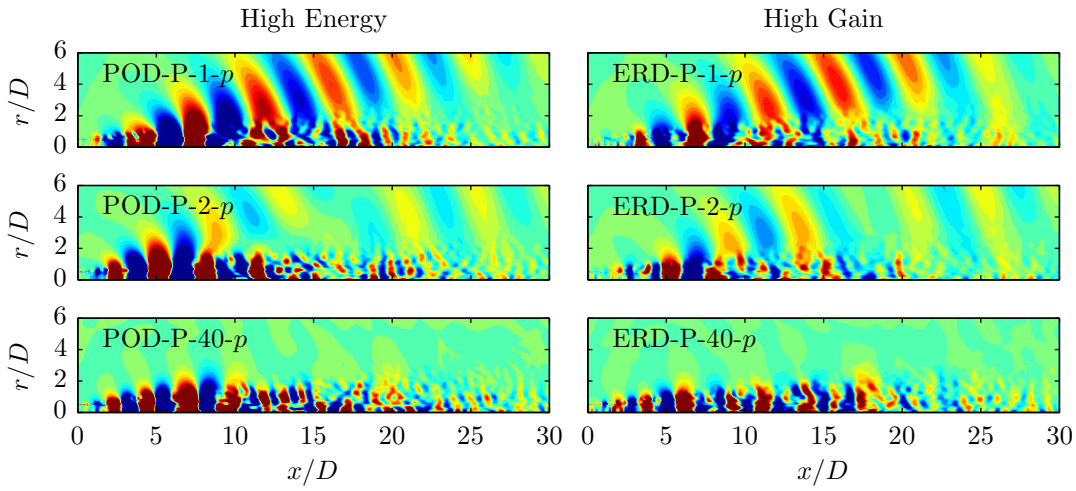


Figure 3.28: Pressure for POD-P and ERD-P modes 1, 2, and 40 at $St = 0.26$. The acoustic fields of the first two high gain modes are nearly the same as those of the first two high energy modes both in terms of energy form, but the flow field wavepackets in the ERD-P modes have high acoustic efficiency.

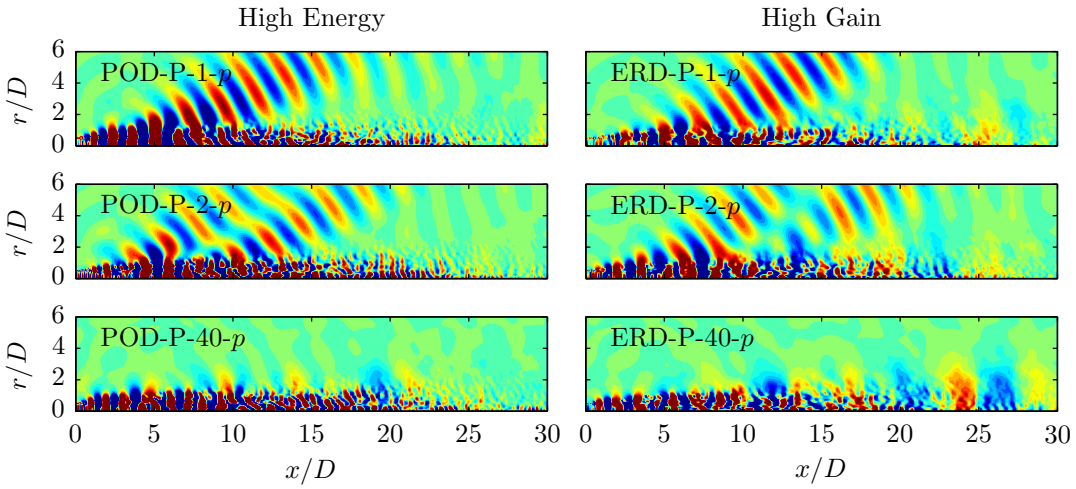


Figure 3.29: Pressure for POD-P and ERD-P modes 1, 2, and 40 at $St = 0.52$. The acoustic fields of the first two high gain modes are nearly the same as those of the first two high energy modes both in terms of energy form, but the flow field wavepackets in the ERD-P modes have high acoustic efficiency.

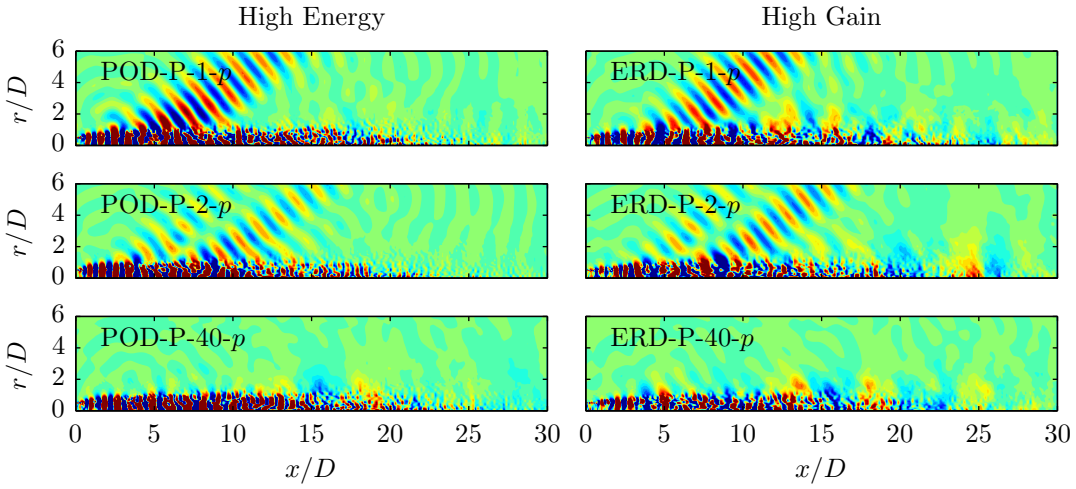


Figure 3.30: Pressure for POD-P and ERD-P modes 1, 2, and 40 at $St = 078$. The acoustic fields of the first two high gain modes are nearly the same as those of the first two high energy modes both in terms of energy form, but the flow field wavepackets in the ERD-P modes have high acoustic efficiency.

Despite exciting nearly the same response, the forcing fields associated with the ERD-P and POD-P modes are markedly different. To begin with, the forcing fields of the first few ERD-P modes are about one-third as energetic as the corresponding POD-P forces. Therefore, ERD effectively distills the forces that most efficiently excite acoustic radiation. The form of these optimal forces are represented using the axial momentum component and compared to the POD-P forces for the three

frequencies in Figures 3.31 - 3.33.

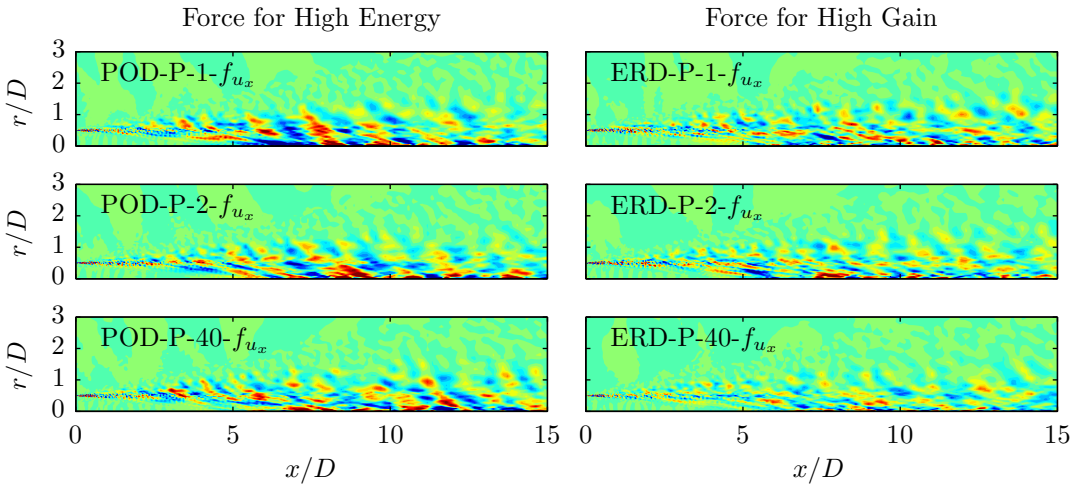


Figure 3.31: Streamwise momentum force for POD-P and ERD-P modes 1, 2, and 40 at $St = 0.26$. The form of the optimal high gain forces in suggestive of random turbulence.

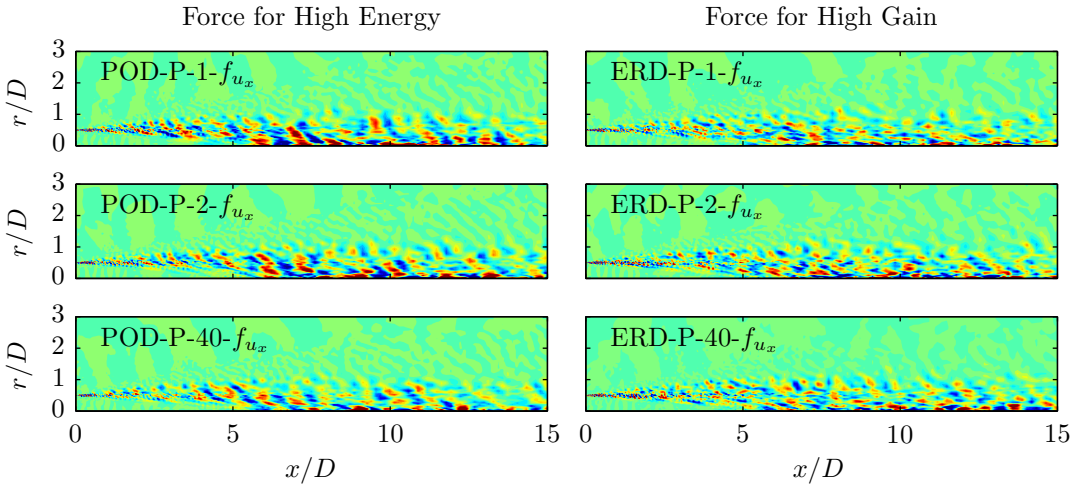


Figure 3.32: Streamwise momentum force for POD-P and ERD-P modes 1, 2, and 40 at $St = 0.52$. The form of the optimal high gain forces in suggestive of random turbulence.

The difference between the ERD-P and POD-P forces is clear – the ERD forces exhibit significantly less evidence of nonlinear wavepacket interaction, and are instead dominated by unstructured fluctuations. That ERD eliminates structured pieces of the force is consistent with the fact that POD-L modes have very little acoustic energy. The form of the remaining forces are suggestive of random turbulence. Furthermore, the mode 1 and 2 forcing fields are nearly identical to the mode 40 forcing fields, signifying a lack of any innate sound-source mechanism. Instead, both loud and

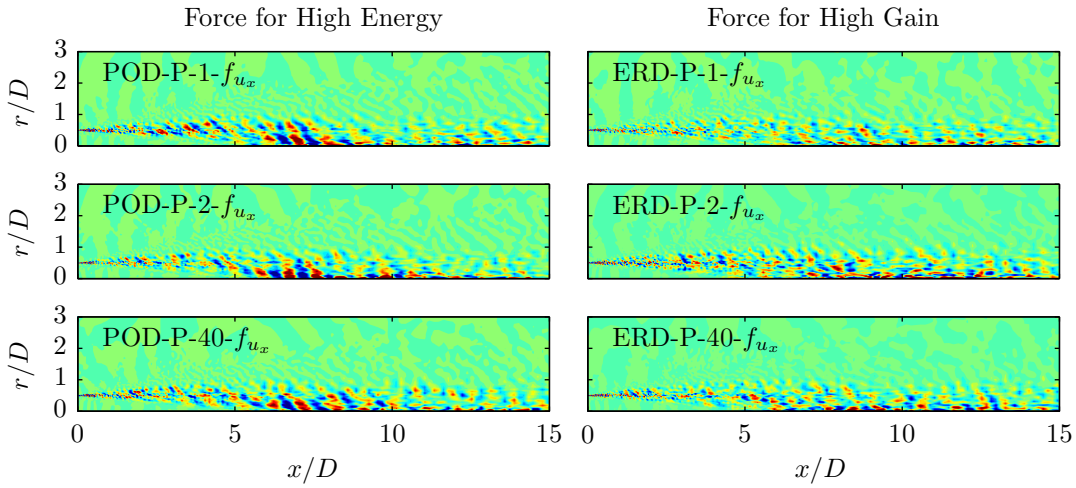


Figure 3.33: Streamwise momentum force for POD-P and ERD-P modes 1, 2, and 40 at $St = 0.78$. The form of the optimal high gain forces in suggestive of random turbulence.

quiet wavepackets are excited by incoherent turbulent fluctuations.

This is, emphatically, *n*ot equivalent to saying that random forces excite random acoustic waves. From Figures 3.28 - 3.30, it is clear that the acoustic field at these frequencies is very coherent and that the corresponding flow field is composed of distorted wavepackets that reach their maximal energy near the end of the potential core. It appears that random turbulent fluctuations excite and jitter wavepackets that radiate acoustic energy. The ERD-P flow fields contain the wavepackets that radiate energy most efficiently. These wavepackets have a shorter streamwise extent and are altogether less structured than their POD-P counterparts, characteristics that are consistent with increased radiative efficiency.

## 3.5 Chapter summary and implications for linear modeling

We have used data and force ensembles of large-eddy-simulation data along with two data decomposition techniques to educe the forcing experienced by wavepackets in a Mach 0.9 turbulent jet.

Modes with high energy in the flow field, acoustic field, or forcing field are extracted using proper orthogonal decomposition. Consistent with previous investigations, the modes with high energy in the flow field have low energy in the acoustic field and vice versa, indicating that energetic coherent

structures exist in fields but are mutually uncorrelated. In contrast, the forcing field noticeably lacks energetic coherent structures, and those that do exist are uncorrelated with acoustic radiation.

The spatial structure of the forces is strikingly different from that of the flow field and acoustic field wavepackets themselves. The forces are concentrated in the shear layer, particularly near the critical layer, and, up to the end of the potential core, show limited signs of nonlinear interactions between coherent structures.

Modes with high gain either between the forces and the flow field or between the forces and the acoustic field are extracted using a novel empirical resolvent-mode decomposition. The high gain modes are nearly as energetic as the high energy modes, but they successfully isolate only the most efficient parts of the forcing field. Specifically, the high gain modes further reduce the signatures of nonlinear wavepacket interactions, leaving unstructured forces that are suggestive of random turbulence rather than nonlinear interactions amongst coherent structures that have sometimes been emphasized in the past (Sandham et al. 2006, Sandham & Salgado 2008, Suponitsky et al. 2010). It appears that turbulent fluctuations excite and jitter wavepackets that radiate acoustic energy.

While further analysis is required, these results bode well for the construction of accurate linear models that capture the energetic, coherent fluctuations in both the flow and acoustic fields. Specifically, they suggest that it is unnecessary to explicitly compute or model nonlinear interactions between coherent structures to capture the dynamics of sound generation. Instead, the essential ingredients are contained within the linear operator itself, not in the forces, and can be coaxed out by forcing the system with some appropriate parameterization of the incoherent turbulent fluctuations. A sufficiently rich ensemble of such forces will excite the high gain modes to produce the observed coherent structures in both the flow and acoustic fields, since both sets of modes are primarily excited by similar incoherent forces.

# Chapter 4

# Concluding Remarks

We conclude this thesis by summarizing its primary contributions and suggesting avenues for the further advancement of wavepacket-based jet turbulence and noise models.

## 4.1 Summary of contributions

This thesis has contributed to two aspects of wavepacket-based jet turbulence and noise models. The first part of the thesis addressed spatial integration methods that can be used to obtain approximate solutions of the linearized flow equations that form the basis of wavepacket models.

First, we showed that the inability of the parabolized stability equations to capture acoustic radiation in subsonic jets is a consequence of the regularization that is required to overcome the ill-posedness of the method. The results of our analysis can be used to qualitatively and quantitatively understand how any quasi-local instability mode of the linear equations is effected by the PSE parabolization.

Second, we developed two alternative spatial integration methods that can be used to efficiently model wavepackets in jets. Unlike PSE, the new methods are well-posed and are capable of capturing both near-field wavepackets and their acoustic radiation. Compared to direct time domain or frequency domain solutions, the one-way spatial integration methods offer an order-of-magnitude reduction in computational cost.

The methods are formulated for general hyperbolic equations and thus have potential applications outside of the context of jet noise modeling. The most obvious application is to inhomogeneous wave

propagation problems that arise in many fields. Examples include underwater acoustics, medical imaging, seismology, and non-isotropic elastic wave problems. One-way equations based on our methodology for these problems could prove to be faster than traditional time domain methods and more accurate than existing one-way equations that are based on factorization and subsequent approximation of quasi-uniform analytical dispersion relations. Additional applications include noise, stability, and transition analysis of free-shear flows such as mixing-layers, as well as wall-bounded flows (for which transverse viscous terms can be incorporated without hindering parabolization) ranging from classical flat-plate boundary layers to complicated swept wings. Unlike the parabolized stability equations, the one-way equations could capture multi-modal behavior within these problems, such as the generation of acoustic waves (as we have seen) or interaction between multiple instability modes.

The second part of the thesis investigated the nonlinear and stochastic forcing of wavepackets that is neglected in most jet noise models. In contrast to the flow and acoustic fields, the forcing field is characterized by a lack of energetic coherent structures. Furthermore, the structures that do exist are largely uncorrelated with the acoustic field. Instead, the forces that most efficiently excite an acoustic response appear to take the form of random turbulent fluctuations, suggesting that direct forcing from nonlinear interactions amongst wavepackets is not an essential noise source mechanism. This has obvious implications for jet noise modeling and in particular suggests that the linear flow operator, not the forcing field, contains the vital ingredient for sound generation. This perspective stands in stark contrast to equivalent-source methodologies.

An additional outcome of this investigation was the derivation of a novel data decomposition technique, called empirical resolvent-mode decomposition, that identifies modes that maximize the gain between input and output data-sets. The method played an important role in the preceding analysis, and could be a valuable tool for studying a wide range of fluid dynamical systems.

## 4.2 Future work

The results from this thesis suggest a number of new avenues for the continued advancement of spatial integration methods in general and jet noise and turbulence modeling in particular.

### 4.2.1 One-way spatial integration

#### Iterative solution strategies

The computational cost of two one-way spatial integration methods developed in Chapter 2 is an order of magnitude lower than direct time domain and frequency domain methods, but could likely be further reduced by employing a tailored iterative approach for solving the necessary recursion equations. An iterative strategy is promising because the equations that must be satisfied change slowly with axial position, and an excellent initial guess is provided at each axial station by the solution at the previous station. A successful implementation of such a strategy could bring the cost of the one-way method down to the level of the parabolized stability equations.

#### Upstream correction

Although we have focused on integrating in the downstream direction, it is equally valid to use the methodology to derive a one-way equation that can be integrated in the upstream direction. In the case of a parallel flow, the complete solution can be obtained by integrating once in each direction, as was demonstrated by the dipole example in section 2.3.7.1. For nonparallel flows, it may be possible to reconstruct the full solution by iteratively integrating downstream and upstream. The clear splitting of the equations into upstream and downstream parts achieved by the projection-based one-way approach make it particularly well-suited for implementing such a scheme.

**Adaptive recursion parameters**

Although the simple strategies for choosing recursion parameters described in section 2.2.6 have proven sufficient for a variety of problems, they are neither universal nor optimal and require a priori analysis of the flow. An automated method for choosing stable, quasi-optimal parameters would be of great value. The terminal ($j = \pm N_\beta$) auxiliary variables contain information that could be used to formulate an adaptive approach to parameter selection. Specifically, these terminal auxiliary variables go to zero as the order of the approximation goes to infinity, and their non-zero values at any finite order is dominated by the modes which are least accurately parabolized by the given set of recursion parameters, therefore providing guidance for modifying the recursion parameters.

**One-way parabolic and mixed hyperbolic-parabolic equations**

The concepts of well-posedness that form the basis for our one-way approximations of hyperbolic equations can likewise by applied to parabolic and mixed hyperbolic-parabolic equations to obtain one-way approximations of these equations. As a proof of concept, we have already derived and validated a one-way approximation of the heat equation, which is parabolic. Of particular interest would be a one-way framework for mixed hyperbolic-parabolic systems, which could be used to fully incorporate viscous effects into a one-way Navier-Stokes approximation.

### 4.2.2 Further analysis of forces

Further analysis is needed to corroborate and extend the findings of Chapter 3. For one, we have so far exclusively considered axisymmetric disturbances at relatively low frequencies. We suspect that the nature and role of wavepacket forcing is substantially different for sufficiently high frequencies and azimuthal wavenumbers, and the limits of the current conclusions must be established. Furthermore, the low frequency, axisymmetric forces that we have investigated are, by definition, a convolution of all frequencies and azimuthal modes that sum to the chosen frequencies and $m = 0$. At present, we cannot say much about which scales may or may not be important in generating these forces.

An effort should be made to break these forces into their individual frequency and wavenumber components. Finally, as mentioned previously, predictive models could be constructed if approximate representations of the forces can be obtained. This will require additional statistical analysis of the LES forces.

# Appendix A

# Segment length and overlap of LES data ensembles

This appendix contains some tests that examine the impact of the segment length and overlap percentage of the LES data ensembles on the modal results from Chapter 3. Although in performing this analysis we considered multiple decomposition types and all of the flow and force variables, to keep this appendix to a reasonable length we present results only for POD-P modes and exclusively show pressure. This is sufficient to convey the main results of the analysis. All data has been normalized to have a full-field Euclidean norm of one, and equal contour levels are then used for all subplots within each figure.

## A.1 Overlap

First, we study the effect of the overlap percentage between adjacent segments. Specifically, we take segments with a uniform length of 128 snapshots and compute the ffts and POD modes for overlaps of 25%, 50%, 75%, 83%, and 87.5%. Compared to the 50% overlap case, the total number of segments change by a factor of $\frac{2}{3}$, 1, 2, 3, and 4.

Figures A.1 and A.2 show the pressure for the first and fortieth modes at $St = 0.35$ and $St = 0.69$, respectively. For all values of the overlap, the first mode is nearly identical. The main observed effect was that higher modes converged with high overlap. This can't be seen very clearly for mode 40 but is noticeable up to at least mode 20.

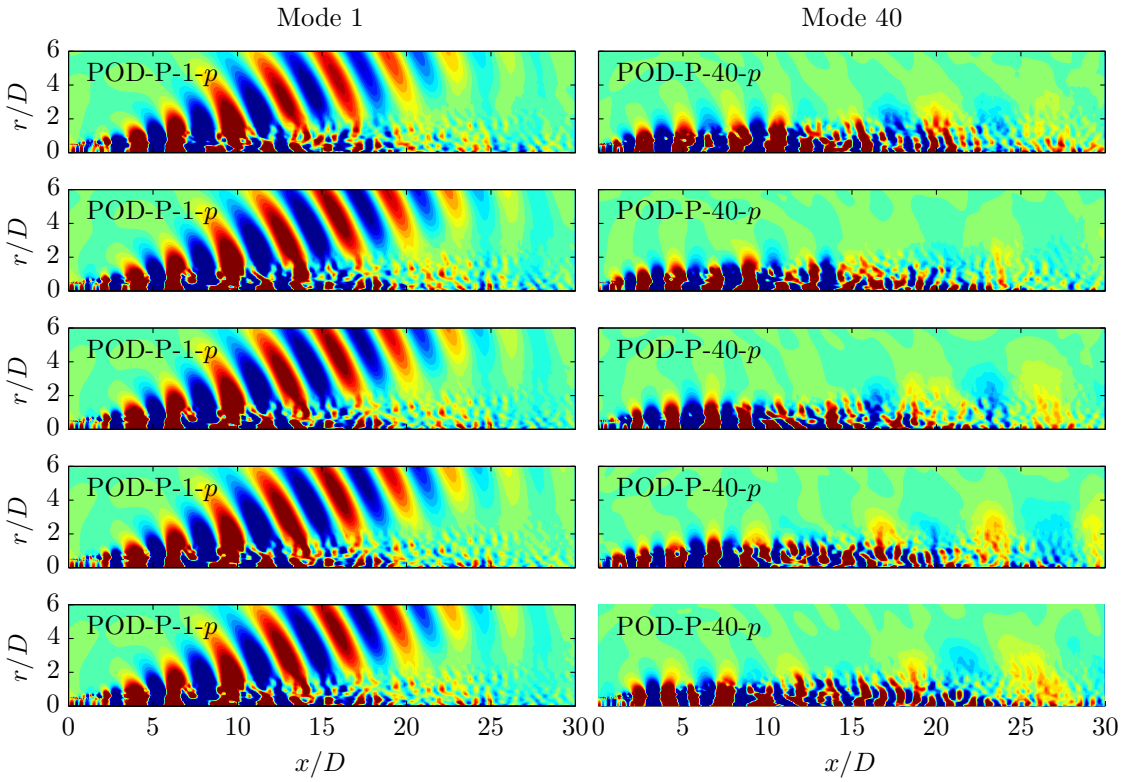


Figure A.1: Pressure field for modes 1 and 40 at $St = 0.35$. The ffts were computed using a segment length of 128 and overlaps of 25%, 50%, 75%, 83%, and 88%, which are shown top to bottom.

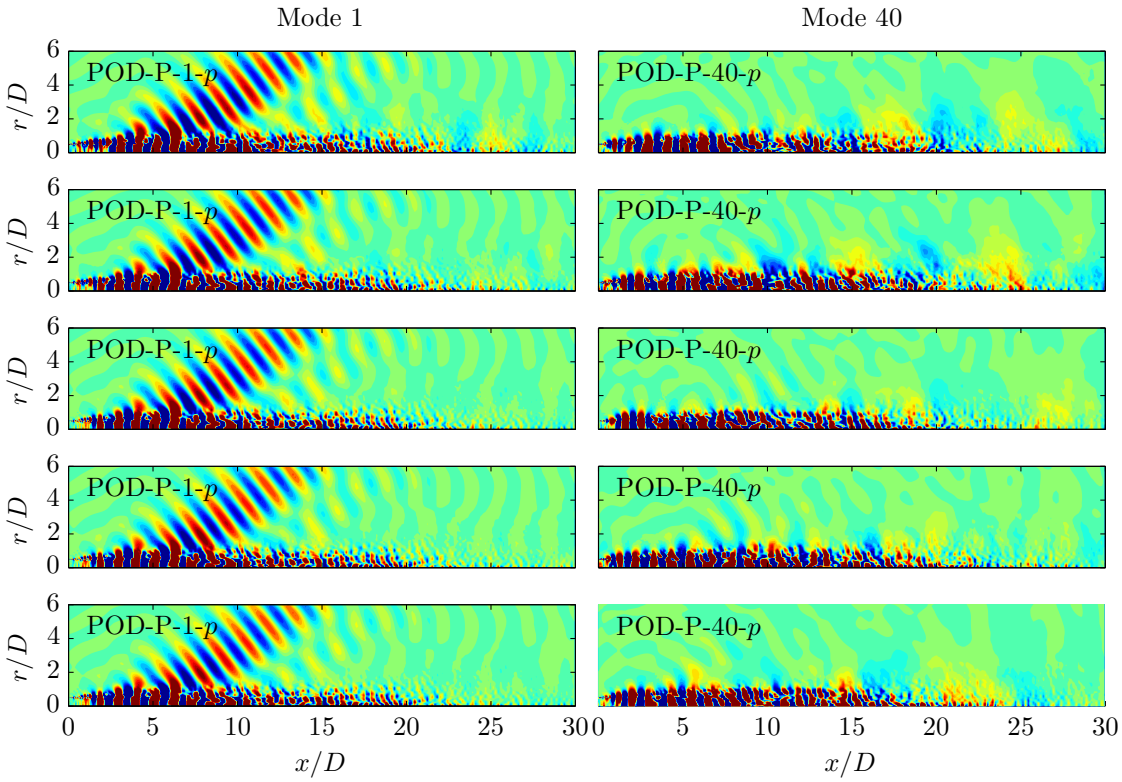


Figure A.2: Pressure field for modes 1 and 40 at $St = 0.69$. The ffts were computed using a segment length of 128 and overlaps of 25%, 50%, 75%, 83%, and 88%, which are shown top to bottom.

## A.2 Segment length

Next, we study the effect of the fft segment length. Specifically, we perform the Fourier and POD analysis using segment lengths of 64, 128, and 256, all with 50% overlap. Figure A.3 shows the pressure for the first and fortieth modes at $St = 0.35$. The most obvious difference is that the acoustic radiation in mode 1 is stronger for lower segment lengths, but the directivity is the same. Figure A.4 shows the pressure for the first and fortieth modes at $St = 0.69$. Compared to $St = 0.35$, the effect of the segment length on mode 1 is much less significant, and the results for segment lengths of 128 and 256 are nearly identical.

These results can be explained as follows. The acoustic events at each frequency within a given segment are averaged by the fft. Since the acoustics are intermittent, there are some very loud events and some quiet ones. When using short segments, a small number of events are averaged over, resulting in some loud jet realizations and some quiet ones. This variety gives POD the opportunity

to isolate very loud acoustics. When longer segments are used, more events are averaged over in each segment, resulting is less variety in the different realizations. This makes it more difficult for POD to isolate loud acoustics. This effect is more noticeable at low frequency since fewer low frequency events fit in each segment. A more relevant test of segment length is conducted in the next section.

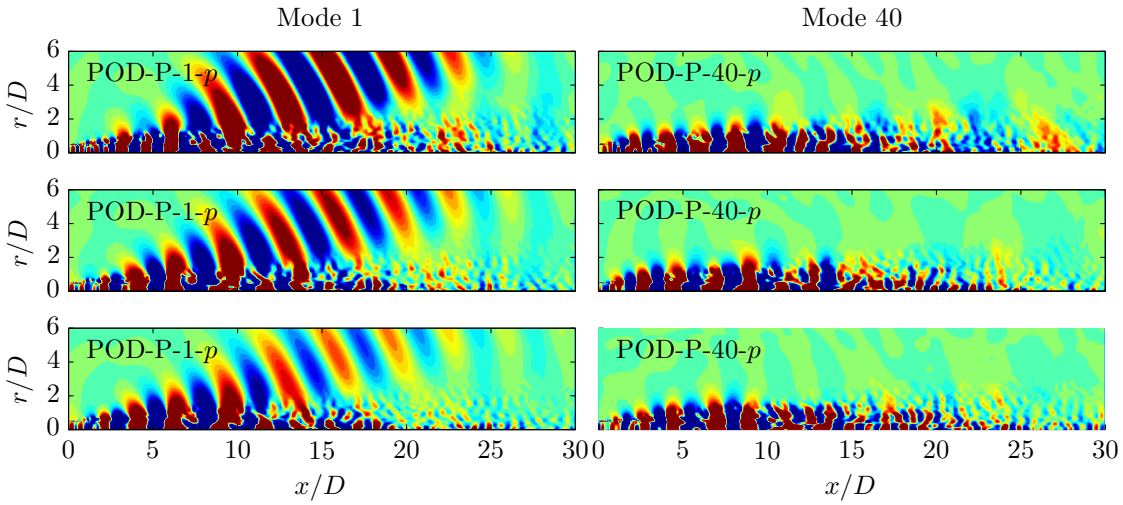


Figure A.3: Pressure field for modes 1 and 40 at $St = 0.35$. The ffts were computed using 50% overlap and segment lengths of 64, 128, and 256, which are shown top to bottom.

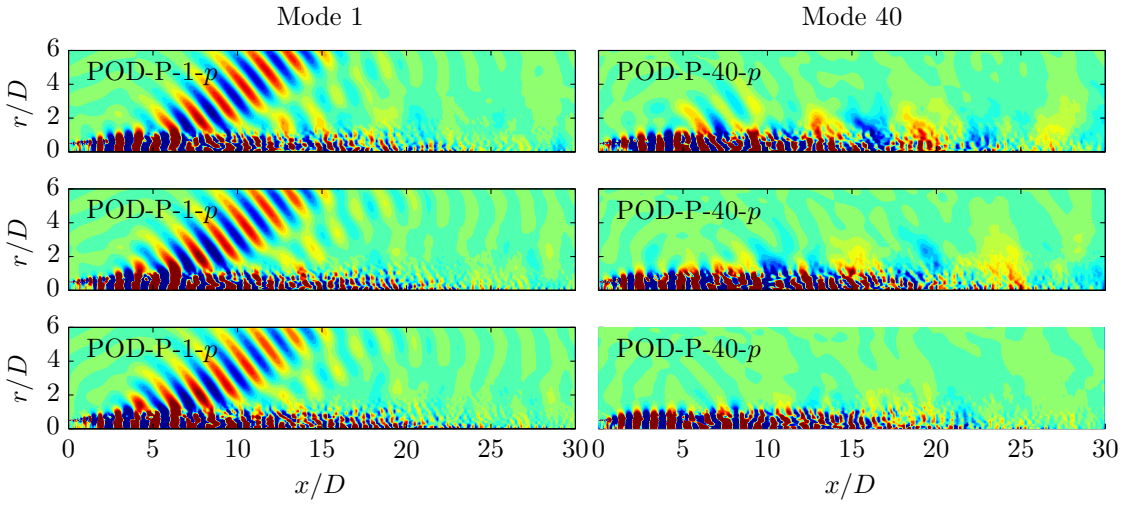


Figure A.4: Pressure field for modes 1 and 40 at $St = 0.69$. The ffts were computed using 50% overlap and segment lengths of 64, 128, and 256, which are shown top to bottom.

## A.3 Time delay

Finally, we examine whether introducing a time delay between the near-field source region and the acoustic region has a significant effect on the results. This can be viewed as a test of whether a given segment length is long enough to contain the complete process of sound generation and propagation. For convenience, we use time delays equal to the time difference between adjacent fft segments, which then avoids the need to compute any additional ffts.

Each un-delayed POD mode is constructed as

$$\tilde{q}_j = \sum_{k=1}^{N} q_k \psi_{kj}, \tag{A.1}$$

where the $\psi_{kj}$ expansion coefficients are the solution of the usual economy POD eigenvalue problem. To incorporate the effect of a time delay, we compute the POD of the far-field, and then use these expansion coefficients to construct time delayed modes of the form

$$\tilde{q}_j^d = \sum_{k=1}^{N} q_{k-d} \psi_{kj}, \tag{A.2}$$

where $d$ is an integer that controls the length of the delay.

We show results for two segments lengths. First, we use segments of length 128 with 75% overlap, which results in delays times that are multiples of 6.4 acoustic time units. The pressure is shown for modes 1 and 40 at $St = 0.35$ and $St = 0.69$ in Figures A.5 and A.6. Note that the time delay that one might suggest given the approximate source location and the direction of the acoustic beam is approximately 12 acoustic time units, so the delay of -12.8 is most physically relevant (third row in plots). Some small differences are apparent between these results the un-delayed results.

The differences can be mostly eliminated by using longer segments. To show this, we use segments of length 256 with 75% overlap, resulting in delays that are multiples of 12.8 acoustic time units. The pressure is shown for modes 1 and 40 at $St = 0.35$ and $St = 0.69$ in Figures A.7 and A.8. Again, the delay of -12.8 is most relevant (now second row). Now, the differences compared to the

un-delayed results are minor. The conclusion is then that using segment lengths of 256 is sufficient to eliminate the need for explicitly incorporating a time delay. Or, to say it another way, segments of length 256 are long enough to ensure that the entire process of sound generation and propagation to the outer extent of the domain fit within a single segment.

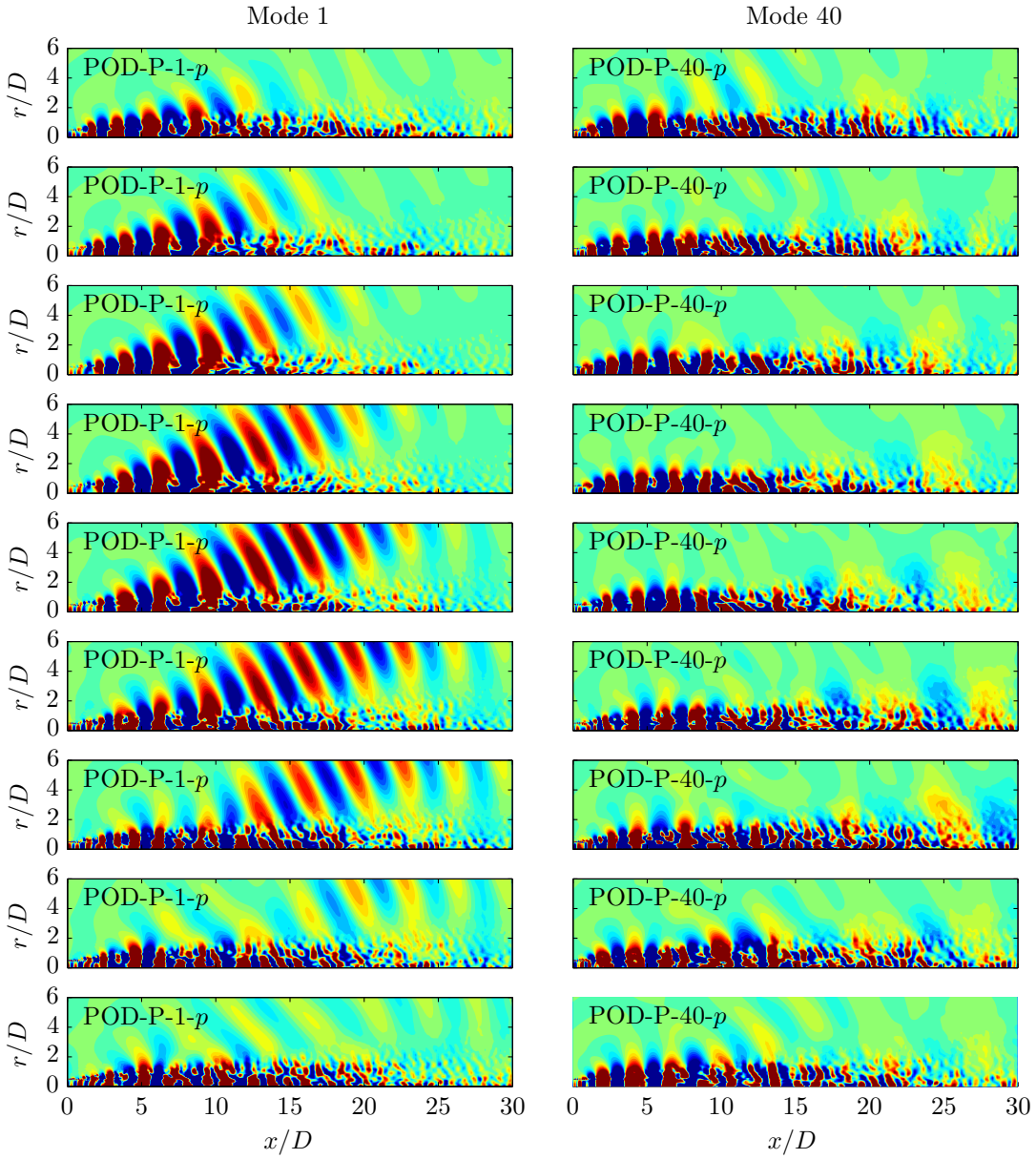


Figure A.5: Pressure field for modes 1 and 40 at $St = 0.35$ with segment lengths of 128 and different time shifts between the near- and far- fields. From top to bottom: -25.6, -19.2, -12.8, -6.4 0, 6.4, 12.8, 19.2, 25.6 acoustic time units.

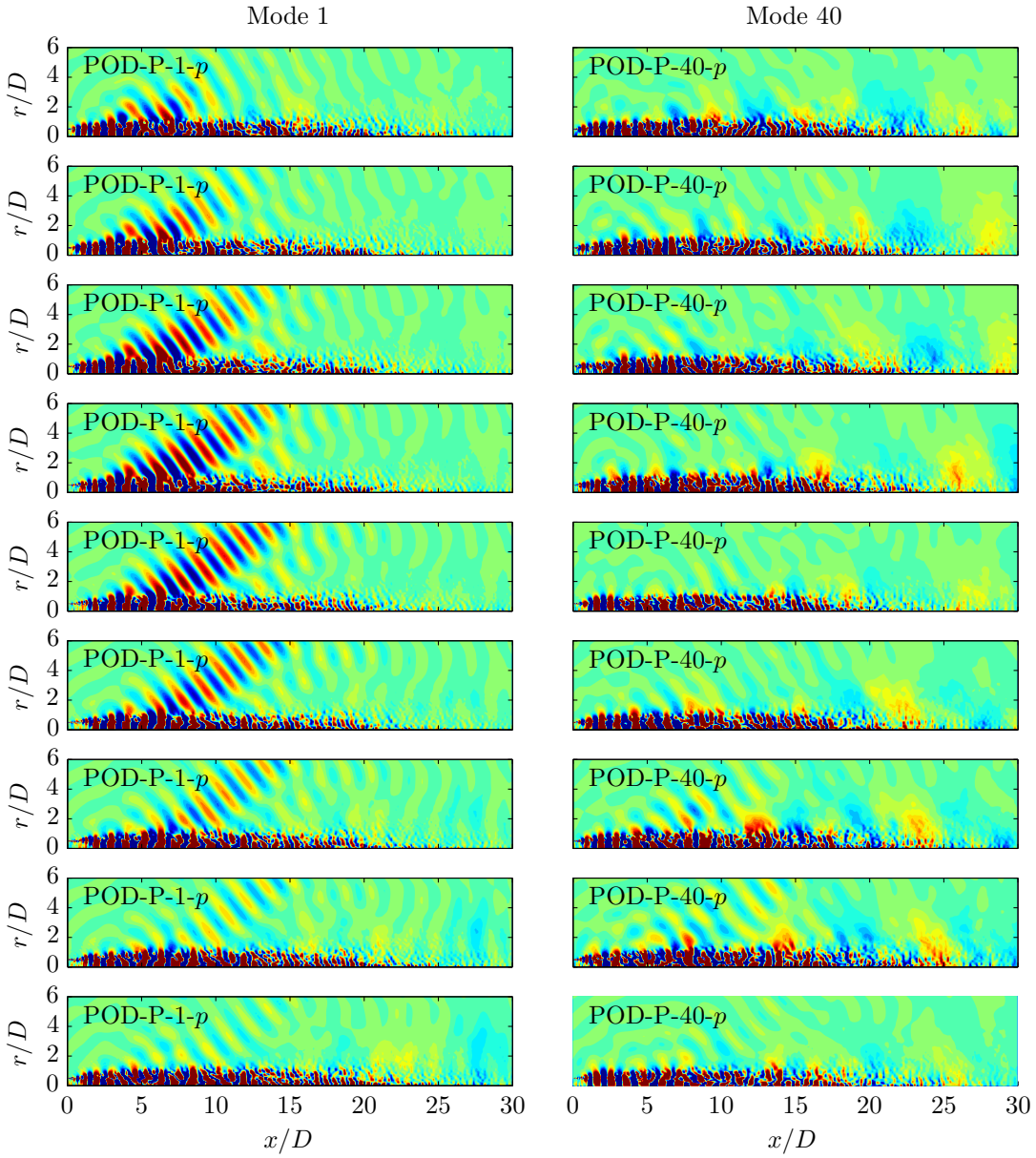


Figure A.6: Pressure field for modes 1 and 40 at $St = 0.35$ with segment lengths of 128 and different time shifts between the near- and far- fields. From top to bottom: -25.6, -19.2, -12.8, -6.4 0, 6.4, 12.8, 19.2, 25.6 acoustic time units.

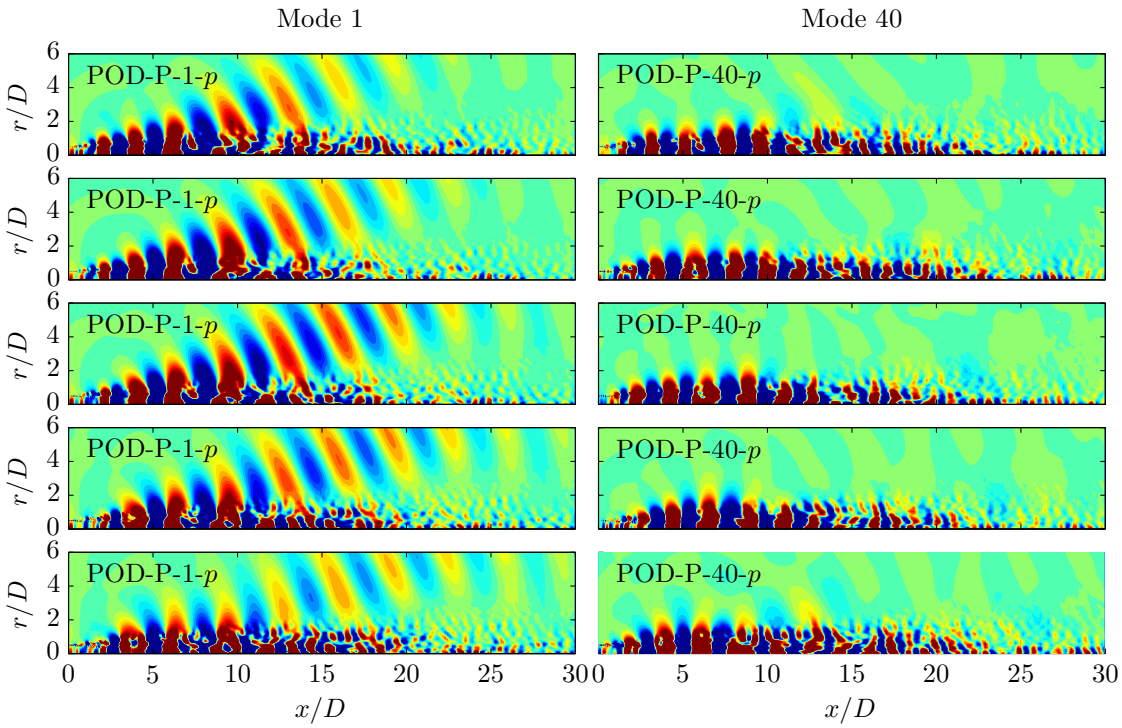


Figure A.7: Pressure field for modes 1 and 40 at $St = 0.35$ with segment lengths of 256 and different time shifts between the near- and far- fields. From top to bottom: -25.6, -12.8, 0, 12.8, 25.6 acoustic time units.

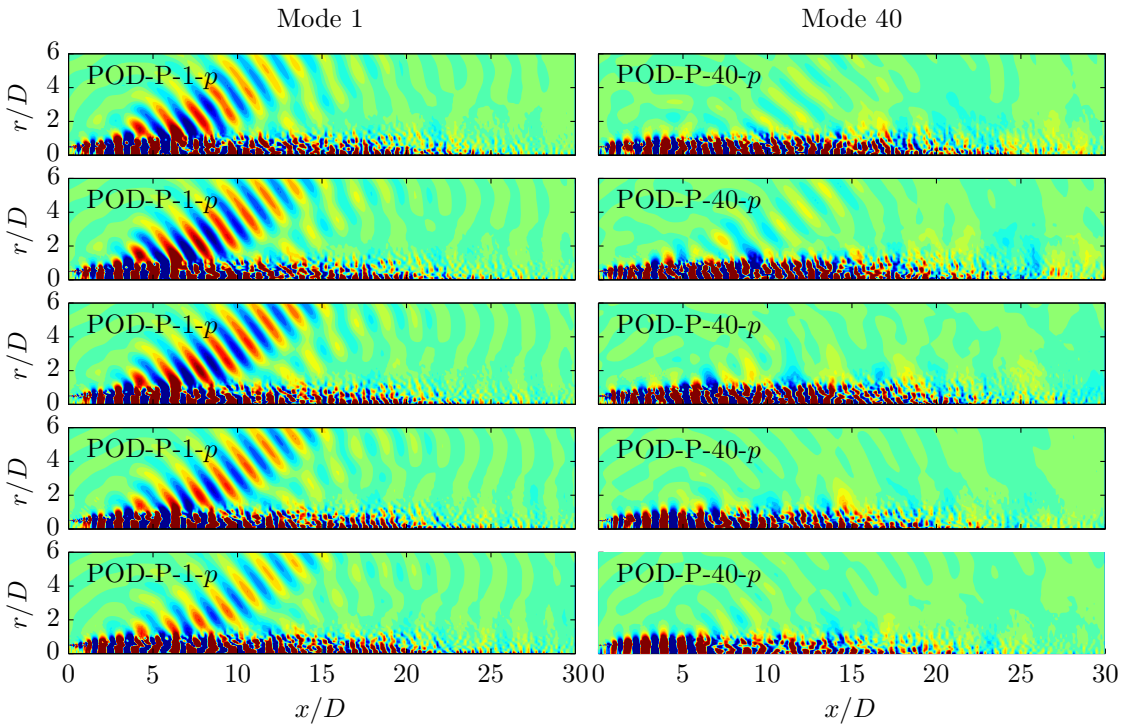


Figure A.8: Pressure field for modes 1 and 40 at $St = 0.35$ with segment lengths of 256 and different time shifts between the near- and far- fields. From top to bottom: -25.6, -12.8, 0, 12.8, 25.6 acoustic time units.

# Bibliography

Andersson, P., Henningson, D. & Hanifi, A. (1998), 'On a stabilization procedure for the parabolic stability equations', *J. Engr. Mech.* **33**, 311–332.

Appelo, D. & Colonius, T. (2009), 'A high-order super-grid-scale absorbing layer and its application to linear hyperbolic systems', *J. Comput. Phys.* **228**(11), 4200–4217.

Arndt, R. E., Long, D. & Glauser, M. (1997), 'The proper orthogonal decomposition of pressure fluctuations surrounding a turbulent jet', *J. Fluid Mech.* **340**, 1–33.

Baqui, Y. B., Agarwal, A., Cavalieri, A. & Sinayoko, S. (2013), Nonlinear and linear noise source mechanisms in subsonic jets, *in* '19th AIAA/CEAS Aeroacoustics Conference, AIAA Paper 2013-2279', Berlin, Germany.

Bodony, D. J. & Lele, S. K. (2008), 'Current status of jet noise predictions using large-eddy simulation', *AIAA J.* **46**(2), 364–380.

Borée, J. (2003), 'Extended proper orthogonal decomposition: a tool to analyse correlated events in turbulent flows', *Exp. Fluids* **35**(2), 188–192.

Brès, G. A., Jaunet, J., Le Rallic, M., Jordan, P., Colonius, T. & Lele, S. K. (2015), Large eddy simulation for jet noise: the importance of getting the boundary layer right, *in* '21st AIAA/CEAS Aeroacoustics Conference'.

Brès, G. A., Jordan, P., Colonius, T., Rallic, M. L., Jaunet, V. & Lele, S. K. (2014), Large eddy simulation of a turbulent Mach 0.9 jet, Technical report, Proceedings of the Center for Turbulence Research summer program.

Briggs, R. J. (1964), *Electron-Stream Interactions with Plasmas*, MIT Press, Cambridge, Massachusetts.

Candel, S. (1979), 'Numerical solution of wave scattering problems in the parabolic approximation', *J. Fluid Mech.* **90**, 465–507.

Cavalieri, A. V. G., Jordan, P., Agarwal, A. & Gervais, Y. (2011), 'Jittering wave-packet models for subsonic jet noise', *J. Sound Vib.* **330**(18), 4474–4492.

Cavalieri, A. V., Rodríguez, D., Jordan, P., Colonius, T. & Gervais, Y. (2013), 'Wavepackets in the velocity field of turbulent jets', *J. Fluid Mech.* **730**, 559–592.

Chang, C., Malik, M., Erlebacher, G. & Hussaini, M. Y. (1991), Compressible stability of growing boundary layers using parabolized stability equations, *in* '22nd Fluid Dynamics, Plasma Dynamics and Lasers Conference', Honolulu,HI,U.S.A.

Cheung, L. & Lele, S. (2007), Aeroacoustic noise prediction and the dynamics of shear layers and jets using the nonlinear parabolized stability equations, Technical Report TF-103.

Cheung, L. & Lele, S. (2009), 'Linear and nonlinear processes in two-dimensional mixing layer dynamics and sound radiation', *J. Fluid Mech.* **625**, 321–351.

Citriniti, J. & George, W. (2000), 'Reconstruction of the global velocity field in the axisymmetric mixing layer utilizing the proper orthogonal decomposition', *J. Fluid Mech.* **418**, 137–166.

Claerbout, J. (1976), *Fundamentals of Geophysical Data Processing*, McGraw-Hill, New York.

Claerbout, J. (1985), *Imaging the Earth's Interior*, Blackwell Scientific Publications, Inc., Cambridge, MA, USA.

Collins, M. (1989), 'Applications and timedomain solution of higherorder parabolic equations in underwater acoustics', *J. Acoust. Soc. Am.* **86**(3), 1097–1102.

Colonius, T., Lele, S. & Moin, P. (1994), 'The scattering of sound waves by a vortex: numerical simulations and analytical solutions', *J. Fluid Mech.* **260**, 271–298.

Colonius, T., Samanta, A. & Gudmundsson, K. (2010), 'Parabolized stability equation models of large-scale jet mixing noise', *IUTAM Symposium on Computational Aero-Acoustics for Aircraft Noise Prediction* .

Crighton, D. G. & Gaster, M. (1976), 'Stability of slowly diverging jet flow', *J. Fluid Mech.* **77**, 397–413.

Crighton, D. & Huerre, P. (1990), 'Shear-layer pressure fluctuations and superdirective acoustic sources', *J. Fluid Mech.* **220**, 355–368.

Crow, S. & Champagne, F. (1971), 'Orderly structures in jet turbulence', *J. Fluid Mech.* **48**, 547–591.

Day, M., Mansour, N. & Reynolds, W. (2001), 'Nonlinear stability and structure of compressible reacting mixing layers', *J. Fluid Mech.* **446**, 375–408.

Engquist, B. & Majda, A. (1977), 'Absorbing boundary conditions for the numerical simulation of waves', *Math. Comput.* **31**(139), pp. 629–651.

Ffowcs-Williams, J. & Hawkings, D. L. (1969), 'Sound generation by turbulence and surfaces in arbitrary motion', *Philosophical Transactions of the Royal Society of London A: Mathematical, Physical and Engineering Sciences* **264**, 321–342.

Freund, J. B. (2001), 'Noise sources in a low-Reynolds-number turbulent jet at Mach 0.9', *J. Fluid Mech.* **438**, 277–305.

Freund, J. & Colonius, T. (2009), 'Turbulence and sound-field POD analysis of a turbulent jet', *International Journal of Aeroacoustics* **8**(4), 337–354.

Fuchs, H. V. (1972), 'Space correlations of the fluctuating pressure in subsonic turbulent jets', *Journal of sound and vibration* **23**(1), 77–99.

Garnaud, X., Lesshafft, L., Schmid, P. & Huerre, P. (2013), 'The preferred mode of incompressible jets: linear frequency response analysis', *J. Fluid Mech.* **716**, 189–202.

Givoli, D. (2004), 'High-order local non-reflecting boundary conditions: a review', *Wave Motion* **39**(4), 319 – 326.

Givoli, D. & Neta, B. (2003), 'High-order nonreflecting boundary scheme for time- dependent waves', *J. Comput. Phys.* **186**, 24–46.

Goldstein, M. (2003), 'A generalized acoustic analogy', *J. Fluid Mech.* **488**, 315–333.

Gordeyev, S. & Thomas, F. (2000), 'Coherent structure in the turbulent planar jet. Part 1. extraction of proper orthogonal decomposition eigenmodes and their self-similarity', *J. Fluid Mech.* **414**, 145–194.

Gudmundsson, K. & Colonius, T. (2011), 'Instability wave models for the near-field fluctuations of turbulent jets', *J. Fluid Mech.* **689**, 97–128.

Hagstrom, T., Becache, E., Givoli, D. & Stein, K. (2012), 'Complete radiation boundary conditions for convective waves', *Commun. Comput. Phys.* **11**(2), 610–628.

Hagstrom, T. & Warburton, T. (2004), 'A new auxiliary variable formulation of high-order local radiation boundary conditions: corner compatibility conditions and extensions to first-order systems', *Wave Motion* **39**, 890–901.

Hagstrom, T. & Warburton, T. (2009), 'Complete radiation boundary conditions: minimizing the long time error growth of local methods', *SIAM J. Numer. Anal.* **47**, 3678–3704.

Hagstrom, T., Watburton, T. & Givoli, D. (2007), 'Radiation boundary conditions for time-dependent waves based on complete plane wave expansions', *J. Comput. App. Math.* **45**(4), 1988–1995.

Hairer, E. & Wanner, G. (1971), *Solving Ordinary Differential Equatoins II: Stiff and Differential-Algebraic Problems*, Springer-Verlag, New York.

Haj-Hariri, H. (1994), 'Characteristics analysis of the parabolized stability equations', *Stud. Appl. Math.* **92**(1), 41–53.

Herbert, T. (1997), 'Parabolized stability equations', *Annu. Rev. Fluid Mech.* **29**, 245–283.

Hileman, J., Thurow, B., Caraballo, E. & Samimy, M. (2005), 'Large-scale structures evolution and sound emission in high-speed jets: real-time visualization with simultaneous acoustic measurements', *J. Fluid Mech.* **544**, 277–307.

Huerre, P. & Monkewitz, P. A. (1990), 'Local and global instabilities in spatially developing flows', *Annu. Rev. of Fluid Mech.* **22**, 473–537.

Hussain, F. (1983), 'Coherent structuresreality and myth', *Phys. Fluids* **26**, 2816–2850.

Hussain, F. (1986), 'Coherent structures and turbulence', *J. Fluid Mech.* **173**, 303–356.

Jensen, F., Kuperman, W., Porter, M. & Schmidt, H. (2001), *Computational Ocean Acoustics*, Modern Acoustics and Signal Processing, 2nd edn, Springer.

Jordan, P. & Colonius, T. (2013), 'Wave packets and turbulent jet noise', *Annu. Rev. of Fluid Mech.* **45**, 173–195.

Jordan, P., Colonius, T., Bres, G. A., Zhang, M., Towne, A. & Lele, S. (2014), Modeling intermittent wavepackets and their radiated sound in a turbulent jet, Technical report, Proceedings of the Center for Turbulence Research summer program.

Jovanović, M. R. & Bamieh, B. (2005), 'Componentwise energy amplification in channel flows', *J. Fluid Mech.* **534**, 145–183.

Kerhervé, F., Jordan, P., Cavalieri, A. V. G., Delville, J., Bogey, C. & Juvé, D. (2012), 'Educing the source mechanism associated with downstream radiation in subsonic jets', *J. Fluid Mech.* **710**, 606.

Kibens, V. (1980), 'Discrete noise spectrum generated by acoustically excited jet', *AIAA J.* **18**, 434–441.

Korte, J. (1991), 'An explicit upwind algorithm for solving the parabolized Navier-Stokes equations', *NASA Technical Paper* **3050**, 890–901.

Kreiss, H. (1970), 'Initial boundary value problems for hyperbolic systems', *Commun. Pure Appl. Math* **23**, 277–298.

Laufer, J. (1974), On the mechanism of noise generation by turbulence, *in* 'Omaggio a Carlo Ferrari', Vol. 1.

Lee, H. K. & Ribner, H. (1972), 'Direct correlation of noise and flow of a jet', *J. Acoust. Soc. Am.* **52**(5A), 1280–1290.

Li, F. & Malik, M. (1996), 'On the nature of PSE approximation', *Theoret. Comput. Fluid Dynamics* **8**, 253–273.

Li, F. & Malik, R. (1997), 'Spectral analysis of the parabolized stability equations', *Computers & Fluids* **26**(3), 279–297.

Lighthill, M. J. (1952), 'On sound generated aerodynamically. I. general theory', *Proc. R. Soc. London Ser. A* **211**(1107), 564–587.

Lighthill, M. J. (1954), 'On sound generated aerodynamically. II. turbulence as a source of sound', *Proc. R. Soc. London Ser. A* **222**(1148), 1–32.

Lilley, G. (1974), 'On the noise from jets', *Agard cp-131* **13**, 12.

Luhar, M., Sharma, A. & McKeon, B. (2014), 'On the structure and origin of pressure fluctuations in wall turbulence: predictions based on the resolvent analysis', *J. Fluid Mech.* **751**, 38–70.

Lumley, J. L. (1967), The Structure of Inhomogeneous Turbulent Flows, *in* A. M. Yaglom & V. I. Tatarski, eds, 'Atmospheric turbulence and radio propagation', Nauka, Moscow, pp. 166–178.

Mattingly, G. E. & Chang, C. C. (1974), 'Unstable waves on an axisymmetric jet column', *J. Fluid Mech.* **65**, 541–560.

Mattsson, K. & Nordstrm, J. (2004), 'Summation by parts operators for finite difference approximations of second derivatives', *J. Comput. Phys.* **199**(2), 503 – 540.

Maurel, S., Borée, J. & Lumley, J. (2001), 'Extended proper orthogonal decomposition: Application to jet/vortex interaction', *Flow Turbul. Combust.* **67**(2), 125–136.

McKeon, B. & Sharma, A. (2010), 'A critical-layer framework for turbulent pipe flow', *Journal of Fluid Mechanics* **658**, 336–382.

Michalke, A. (1971), 'An expansion scheme for the noise from circular jets', *Z.. Flugwiss* **19**.

Michalke, A. (1984), 'Survey on jet instability theory', *Prog. Aerosp. Sci.* **21**, 159 – 199.

Michalke, A. & Fuchs, H. (1975), 'On turbulence and noise of an axisymmetric shear flow', *J. Fluid Mech.* **70**(01), 179–205.

Mohseni, K. & Colonius, T. (2000), 'Numerical treatment of polar coordinate singularities', *J. Comput. Phys.* **157**(2), 787–795.

Mohseni, K., Colonius, T. & Freund, J. B. (2002), 'An evaluation of linear instability waves as sources of sound in a supersonic turbulent jet', *Phys. Fluids* **14**(10), 3593–3600.

Morris, P. J. (1976), 'The spatial viscous instability of axisymmetric jets', *J. Fluid Mech.* **77**, 511–529.

Morrison, G. & McLaughlin, D. (1979), 'Noise generation by instabilities in low Reynolds number supersonic jets', *J. Sound Vib.* **65**(2), 177–191.

Naval Research Advisory Committee (2009), 'Report on jet engine noise reduction'.

Nichols, J. & Jovanović, M. (2014), Input-output analysis of high speed jet noise, Technical report, Proceedings of the Center for Turbulence Research summer program.

Phillips, O. M. (1960), 'On the generation of sound by supersonic turbulent shear layers', *J. Fluid Mech.* **9**(01), 1–28.

Reba, R., Narayanan, S. & Colonius, T. (2010), 'Wave-packet models for large-scale mixing noise', *Int. Journal. Aeroacoustics* **9**, 533–558.

Rodriguez, D., Sinha, A., Brs, G. A. & Colonius, T. (2013), Acoustic field associated with parabolized stability equation models in turbulent jets, *in* '19th AIAA/CEAS Aeroacoustics Conference, AIAA Paper 2013-2279', Berlin, Germany.

Rubin, S. & Tannehill, J. (1992), 'Parabolized/reduced Navier-Stokes computational techniques', *Annu. Rev. Fluid Mech.* **24**, 117–144.

Sandham, N. D., Morfey, C. & Hu, Z. (2006), 'Nonlinear mechanisms of sound generation in a perturbed parallel jet flow', *J. Fluid Mech.* **565**, 1–23.

Sandham, N. D. & Salgado, A. M. (2008), 'Nonlinear interaction model of subsonic jet noise', *Philos. Trans. R. Soc. London, Ser. A* **366**, 2745–2760.

Schlegel, M., Noack, B. R., Jordan, P., Dillmann, A., Grschel, E., Schrder, W., Wei, M., Freund, J. B., Lehmann, O., & Tadmor, G. (2012), 'On least-order flow representations for aerodynamics and aeroacoustics', *J. Fluid Mech.* **697**, 367–398.

Schmid, P. J. (2010), 'Dynamic mode decomposition of numerical and experimental data', *J. Fluid Mech.* **656**, 5–28.

Schmid, P. J. & Henningson, D. S. (2001), *Stability and Transition in Shear Flows*, Vol. 142, Springer Science & Business Media.

Semeraro, O., Lesshafft, L. & Sandberg, R. (2015), Can jet noise be predicted using linear instability wavepackets?, *in* '5th International Conference on Jets Wakes and Separated Flows', Stockholm, Sweden.

Sharma, A. & McKeon, B. (2013), 'On coherent structure in wall turbulence', *Journal of Fluid Mechanics* **728**, 196–238.

Sinha, A., Rodriguez, D., Bres, G. & Colonius, T. (2014), 'Wavepacket models for supersonic jet noise', *J. Fluid Mech.* **742**, 71–95.

Sipp, D., Marquet, O., Meliga, P. & Barbagallo, A. (2010), 'Dynamics and control of global instabilities in open-flows: a linearized approach', *Applied Mechanics Reviews* **63**(3).

Sirovich, L. (1987), 'Turbulence and the dynamics of coherent structures, Part III: Dynamics and scaling', *Quarterly of Appl. Math.* **XLV**, 583–590.

Suponitsky, V., Sandham, N. D. & Morfey, C. L. (2010), 'Linear and nonlinear mechanisms of sound radiation by instability waves in subsonic jets', *J. of Fluid. Mech.* **658**, 509–538.

Suzuki, T. & Colonius, T. (2006), 'Instability waves in a subsonic round jet detected using a near-field phased microphone array', *J. Fluid Mech.* **565**, 197–226.

Tam, C. K. W. & Burton, D. E. (1984), 'Sound generated by instability waves of supersonic flows. Part 2. axisymmetric jets', *J. Fluid Mech.* **138**, 273–295.

Tam, C. K. W. & Hu, F. Q. (1989), 'On the three families of instability waves of high-speed jets', *J. Fluid Mech.* **201**, 447–483.

Tam, C. K. W. & Morris, P. J. (1980), 'The radiation of sound by the instability waves of a compressible plane turbulent shear layer', *J. Fluid Mech.* **98**, 349–381.

Tam, C. K. W., Viswanathan, K., Ahuja, K. K. & Panda, J. (2008), 'The sources of jet noise: experimental evidence', *J. Fluid Mech.* **615**, 253–292.

Thompson, K. W. (1987), 'Time dependent boundary conditions for hyperbolic systems', *J. Comput. Phys.* **68**, 1–24.

Tissolt, G., Zhang, M., Lajús, F. C., Cavalieri, A., Jordan, P. & Colonius, T. (2015), Sensitivity of wavepackets in jets to non-linear effects: the role of the critical layer, *in* '21st AIAA/CEAS Aeroacoustics Conference, AIAA Paper 2013-2171', Dallas, Texas.

Towne, A., Cavalieri, A., Jordan, P., Colonius, T., Jaunet, V., Schmidt, O. & Brès, G. A. (2016), 'Acoustic waves in the potential core of jets', *Submitted to the 22nd AIAA/CEAS Aeroacoustics Conference, Lyon, France* .

Towne, A., Cavalieri, A., Jordan, P., Colonius, T., Jaunet, V., Schmidt, O. & Brès, G. A. (in prep.), 'Trapped acoustic waves in the core of subsonic jets'.

Towne, A. & Colonius, T. (2013), Improved parabolization of the Euler equations, *in* '19th AIAA/CEAS Aeroacoustics Conference, AIAA Paper 2013-2171', Berlin, Germany.

Towne, A. & Colonius, T. (2014), Continued development of the one-way Euler equations: application to jets, *in* '20th AIAA/CEAS Aeroacoustics Conference, AIAA Paper 2014-2903', Atlanta, Georgia.

Towne, A. & Colonius, T. (2015), 'One-way spatial integration of hyperbolic equations', *J. Comput. Phys.* **300**, 844–861.

Towne, A., Colonius, T., Jordan, P., Cavalieri, A. & Brès, G. A. (2015), Stochastic and nonlinear forcing of wavepackets in a Mach 0.9 jet, *in* '21st AIAA/CEAS Aeroacoustics Conference, AIAA Paper 2015-2217', Dallas, Texas.

Trefethen, L. & Halpern, L. (1986), 'Well-posedness of one-way wave equations and absorbing boundary conditions', *Math Compute.* **47**(176), 421–435.

Williams, J. & Kempton, A. (1978), 'The noise from the large-scale structure of a jet', *J. Fluid Mech.* **84**(04), 673–694.

Yule, A. (1972), Two-Dimensional Self-Preserving Turbulent Mixing Layers at Different Free Stream Velocity Ratios, Technical report, University of Manchester.

Zhang, M., Jordan, P., Lehnasch, G., Cavalieri, A. & Agarwal, A. (2014), Just enough jitter for jet noise, *in* '20th AIAA/CEAS Aeroacoustics Conference', Atlanta, Georgia.